

1  
2  
3  
4  
5  
6  
7  
8  
9  
10  
11  
12  
13  
14  
15  
16  
17  
18  
19  
20  
21  
22  
23  
24  
25  
26  
27  
28  
29  
30  
31  
32  
33  
34  
35  
36  
37  
38  
39  
40  
41  
42  
43  
44  
45  
46  
47  
48  
49  
50  
51  
52  
53  
54  
55  
56  
57  
58  
59  
60  
61  
62  
63  
64  
65

1  
2  
3  
4  
5  
6  
7  
8  
9  
10  
11  
12  
13  
14  
15  
16  
17  
18  
19  
20  
21  
22  
23  
24  
25  
26  
27  
28  
29  
30  
31  
32  
33  
34  
35  
36  
37  
38  
39  
40  
41  
42  
43  
44  
45  
46  
47  
48  
49  
50  
51  
52  
53  
54  
55  
56  
57  
58  
59  
60  
61  
62  
63  
64  
65

**The Genesis of the Giant Shuangjianzishan Epithermal Ag-Pb-Zn Deposit, Inner  
Mongolia, Northeastern China**

Degao Zhai<sup>1, 2\*</sup>, Anthony E. Williams-Jones<sup>2</sup>, Jiajun Liu<sup>1</sup>, David Selby<sup>3, 4</sup>, Panagiotis C. Voudouris<sup>5</sup>,  
Stylianos Tombros<sup>6</sup>, Kuan Li<sup>1</sup>, Peilin Li<sup>1</sup>, Hongjun Sun<sup>7</sup>

<sup>1</sup>*State Key Laboratory of Geological Processes and Mineral Resources, School of Earth Sciences and  
Resources, China University of Geosciences, Beijing, 100083, China*

<sup>2</sup>*Department of Earth and Planetary Sciences, McGill University, Quebec, 3450, Canada*

<sup>3</sup>*Department of Earth Sciences, Durham University, Durham, DH1 3LE, UK*

<sup>4</sup>*State Key Laboratory of Geological Processes and Mineral Resources, School of Earth Resources, China  
University of Geosciences, Wuhan, 430074, China*

<sup>5</sup>*Department of Mineralogy-Petrology, National and Kapodistrian University of Athens, 15784, Athens,  
Greece*

<sup>6</sup>*Department of Geology, University of Patras, Rion, 26500, Greece*

<sup>7</sup>*Tiantong Mining Company, Chifeng, 024000, China*

\*E-mail: [dgzhai@cugb.edu.cn](mailto:dgzhai@cugb.edu.cn)

Revised submission to: *Economic Geology*

With 15 Figures and 5 Tables

21-July-2019

## Abstract

The newly-discovered Shuangjianzishan Ag-Pb-Zn deposit with 145 Mt of ore grading 128.5 g/t Ag (locally up to 32,000 g/t) and 2.2 wt.% Pb+Zn is located in the Great Hinggan Range (GHR) Metallogenic Belt, northeastern China, and is currently the largest Ag deposit in Asia. The Ag-Pb-Zn orebodies occur as veins and are hosted primarily by a Permian slate. Recent drilling and core logging have identified a partially Mo-mineralized granite porphyry intrusion adjacent to the Ag-Pb-Zn mineralized veins. This well-preserved magmatic-hydrothermal system therefore offers an excellent opportunity to evaluate the possible temporal and genetic relationship between Mo-mineralized porphyry intrusions and Ag-Pb-Zn veins. Three primary paragenetic stages of veining have been recognized: (I) early pyrite+quartz±K-feldspar, (II) main ore sulfide+sulfosalt+quartz+calcite+sericite+chlorite±epidote, and (III) post-ore quartz. The silver mineralization occurs mainly in the late paragenetic part of Stage II, in which canfieldite ( $\text{Ag}_8\text{SnS}_6$ ), argentite ( $\text{Ag}_2\text{S}$ ) and freibergite [ $(\text{Ag}, \text{Cu})_{12}\text{Sb}_4\text{S}_{13}$ ] are the dominant Ag-bearing ore minerals. A combination of ore mineral chemical and sulfur isotope geothermometers and physicochemical calculations suggest that the Ag-Pb-Zn mineralization took place at a temperature of 250° to 200°C, a pH of 6.7 to 5.6, and a  $\Delta\log f\text{O}_2$  (HM) of -2.4 to -8.7.

A conspicuous enrichment of Sn and Se in the ore, which is represented by minerals containing the metal suite Ag-Pb-Zn-(Cu-Sn-Se-Sb), likely reflects a close genetic association between the base metal mineralization and a magma. In situ analyses show that the  $\delta^{34}\text{S}$  values of the sulfides and Ag-bearing sulfosalts from the Ag-Pb-Zn mineralized veins vary from -4.67 to +2.44‰; the mean value is  $-2.11 \pm 1.49\%$  (n=77). The calculated mean  $\delta^{34}\text{S}_{\text{H}_2\text{S}}$  value of the ore-forming fluid is  $-1.65 \pm 0.83\%$ , which is indicative of a magmatic sulfur source. In situ Pb isotope analyses of the ore minerals yielded a narrow range of values ( $^{206}\text{Pb}/^{204}\text{Pb}$  of 18.243 to 18.310,  $^{207}\text{Pb}/^{204}\text{Pb}$  of 15.503 to 15.563 and  $^{208}\text{Pb}/^{204}\text{Pb}$  of 38.053 to 38.203, n=59). Comparisons to corresponding isotopic data for the various rock units in the area and sulfides from nearby ore deposits indicate that there were substantial contributions of Pb, and other metals (e.g., Ag and Zn), to the Shuangjianzishan deposit from a Mesozoic granitic source.

Diorite-granodiorite dikes and dacite are crosscut by the Ag-Pb-Zn veins, and therefore, pre-date ore formation. These rock units have zircon U-Pb ages of  $250.2 \pm 2.0$  and  $133.9 \pm 1.4$  Ma, respectively. A concealed, weakly Mo-mineralized granite porphyry intrusion proximal to the Ag-Pb-Zn mineralized vein system yielded zircon U-Pb ages of  $134.4 \pm 1.0$  (MSWD = 0.1) and  $134.4 \pm 1.0$  Ma (MSWD = 0.2), for coarse- and fine-grained facies, respectively. These ages are indistinguishable within the uncertainty

1 61 from the zircon ages for the dacite and a granite intrusion ~2 km north of the mineralized veins,  
2 62 which has a weighted mean zircon U-Pb age of  $135.2 \pm 1.4$  Ma (MSWD = 0.78). Molybdenite from  
3 63 three quartz vein/veinlet samples hosted by slate immediately above the porphyry intrusion yielded  
4 64 Re-Os model ages from  $136.3 \pm 0.9$  to  $133.7 \pm 1.2$  Ma and a weighted mean Re-Os age of  
5 65  $134.9 \pm 3.4$  Ma. Finally, three pyrite samples separated from the Ag-Pb-Zn mineralized veins have a  
6 66 weighted mean Re-Os model age of  $135.0 \pm 0.6$  Ma. The very similar zircon U-Pb ages for the Mo  
7 67 mineralized granite porphyry and dacite, and Re-Os ages for molybdenite and pyrite in the  
8 68 Shuangjianzishan ore district indicate that the Mesozoic magmatic-hydrothermal activity was  
9 69 restricted to a relatively short time interval (~136 to 133 Ma). They also suggest that the weakly Mo-  
10 70 mineralized granite porphyry was likely the source of the fluids and metals that produced the Ag-Pb-  
11 71 Zn mineralization.

12 72 Based on our geological observations and an extensive analytical database, a model is proposed for  
13 73 the genesis of the giant Shuangjianzishan Ag-Pb-Zn deposit in which the ore-forming fluid and its metals  
14 74 (i.e., Ag, Pb, and Zn) were exsolved during crystallization of the final phase of a composite granite  
15 75 porphyry intrusion. This fluid transported metals to the distal parts of the system, where they were  
16 76 deposited in pre-existing faults or fractures created by the withdrawal of magma during the waning  
17 77 stages of the magmatic-hydrothermal event. The present study of the Shuangjianzishan Ag-Pb-Zn  
18 78 deposit and those of other magmatic-hydrothermal ore deposits in the region provide compelling  
19 79 evidence that the widespread Mesozoic felsic magmatism and Ag-Pb-Zn mineralization in the southern  
20 80 GHR took place in an intracontinental extensional tectonic setting, which was synchronous with, and  
21 81 spatially associated to, Paleo-Pacific slab rollback and lithospheric delamination and thinning.

22 82

### 23 83 **Introduction**

24 84 Silver-lead-zinc vein-type mineralization has made a major contribution to the global supply of Ag  
25 85 and base metals. In addition, its close temporal, spatial and genetic association with porphyry-type  
26 86 mineralization has been long recognized and is well documented (e.g., Guilbert and Park, 1986; Einaudi  
27 87 et al., 2003; Sillitoe, 2010; Catchpole et al., 2015). Many studies of magmatic-hydrothermal systems  
28 88 have developed genetic models for porphyry ore systems (Einaudi et al., 2003; Heinrich, 2005; Williams-  
29 89 Jones and Heinrich, 2005; Seedorff et al., 2005; Rusk et al., 2008; Sillitoe, 2010; Richards, 2011;  
30 90 Wilkinson, 2013; Chiaradia, 2014). In contrast, much less attention has been paid to the Ag-Pb-Zn vein

1 91 mineralization, which typically occurs peripheral to, adjacent to, or is superimposed on the mineralized  
2 92 porphyry systems (Seedorff et al., 2005; Sillitoe, 2010; Zhai et al., 2017; Rottier et al., 2018a). The close  
3 93 spatial-temporal relationship between porphyry Cu-Mo and Ag-Pb-Zn vein mineralization has provided  
4 94 a very useful guide for exploration that has led to the discovery of new Ag-Pb-Zn veins adjacent to  
5 95 porphyry Cu-Mo deposits and vice versa, e.g., the Butte ore district (Rusk et al., 2008). Some Ag-Pb-Zn  
6 96 vein deposits, however, do not appear to be genetically linked to porphyry intrusions and their genesis  
7 97 still remains controversial (Beaudoin and Sangster, 1992; Kissin and Mango, 2014).

8 98 Characteristic features of Ag-Pb-Zn vein-type deposits can be summarized as follows: (1) a common  
9 99 metal suite of Ag-Pb-Zn-( $\pm$ Cu $\pm$ Au $\pm$ Bi $\pm$ Sb $\pm$ As), (2) a sulfide-rich ore (commonly massive) composed of  
10 galena, sphalerite and a variety of Ag-bearing sulfosalts and a gangue of quartz and calcite, (3) the  
11 occurrence of the orebodies as epigenetic open-space filled veins spatially associated with sericitization  
12 and silicification, (4) in some cases, a well-developed metal and alteration zonation at the deposit scale,  
13 (5) deposition mostly under epithermal conditions from magmatic-hydrothermal fluids of low to  
14 moderate salinity (commonly <10 wt.% NaCl equivalent), and (6) structural control of the mineralization  
15 by late regional faults (e.g., Einaudi, 1981; Baumgartner et al., 2009; Bendezú and Fontboté, 2009;  
16 Fontboté and Bendezú, 2009; Kissin and Mango, 2014; Catchpole et al., 2015; Rottier et al., 2018a, b;  
17 Zhai et al., 2019a, and references therein). These polymetallic vein deposits, which historically have  
18 been an important source of Zn, Pb, and Ag in the North American Cordillera and in Peru, are also  
19 referred to as Cordilleran base metal deposits, Butte-type vein deposits, polymetallic veins, or zoned  
20 base metal veins (e.g., Einaudi, 1981; Guilbert and Park, 1986; Einaudi et al., 2003; Bendezú and  
21 Fontboté, 2002, 2009; Baumgartner et al., 2009; Fontboté and Bendezú, 2009; Catchpole et al., 2015;  
22 Rottier et al., 2016, and references therein).

23 113 The Great Hinggan Range (GHR) Metallogenic Belt, NE China, hosts a number of porphyry Mo-(Cu),  
24 114 skarn Fe-(Sn), epithermal Au-Ag, and Ag-Pb-Zn vein deposits (e.g., Zeng et al., 2011; Ouyang et al., 2014;  
25 115 Mao et al., 2014; Zhai et al., 2014a, b, 2018a, 2019b; Shu et al., 2016; Chen, Y., et al., 2017). In particular,  
26 116 it contains more than 30 Ag-Pb-Zn ore deposits with total resources of >57,000 t of silver (Zhai et al.,  
27 117 2017), making it the largest silver province in China. The Ag-Pb-Zn vein-type deposits are particularly  
28 118 common in the southern segment of the GHR, where recent discoveries include the Shuangjianzishan,  
29 119 Bianjiadayuan, Bairendaba, and Weilasituo deposits (e.g., Ouyang et al., 2014; Liu, C., et al., 2016; Liu,  
30 120 Y., et al., 2016; Zhai et al., 2017). Among them, the largest is the Shuangjianzishan deposit with reserves

1 121 exceeding 145 Mt of ore at an average grade of 128.5 g/t Ag ( $\approx$  18,630 tons Ag) and 2.2 wt.% Pb+Zn  
2 122 (Kuang et al., 2014), making this deposit the largest Ag deposit in Asia. It also has an extremely high Ag  
3  
4 123 grade, which locally exceeds 32,000 g/t.  
5

6 124 Recently, a concealed, weakly Mo-mineralized granite porphyry intrusion was intersected in drill  
7  
8 125 holes adjacent to the Shuangjianzishan Ag-Pb-Zn veins. Whether-or-not the Ag-Pb-Zn vein  
9  
10 126 mineralization is related to this newly-discovered porphyry intrusion has been unclear, and resolving  
11  
12 127 this issue is important for exploration in the area. Several studies of the Shuangjianzishan deposit,  
13  
14 128 mostly published in Chinese or reported in student dissertations, have addressed the ore deposit  
15  
16 129 geology (Kuang et al., 2014), mineralogy (Wu et al., 2014; Zhai et al., 2019c), whole rock geochemistry  
17  
18 130 (Liu, C., et al., 2016; Gu et al., 2017), magmatic rock and ore geochronology (Wu et al., 2013; Wang et  
19  
20 131 al., 2016; Ouyang et al., 2016; Liu, C., et al., 2016; Wang, F., 2017; Zhang, 2018), and S-Pb isotope  
21  
22 132 geochemistry (Wang, 2015; Jiang, B., et al., 2017; Wang, X., 2017). However, questions related to the  
23  
24 133 sulfur and metal source, the timing of mineralization, and the genesis of the deposit remain unresolved  
25  
26 134 and greatly debated. For example, there is no consensus on the age of ore formation. Wu et al. (2013)  
27  
28 135 proposed a mineralization age of  $132.7 \pm 3.9$  Ma using the sphalerite Rb-Sr method, whereas Wang et  
29  
30 136 al. (2016) obtained ages for alteration and mineralization of  $146.9 \pm 1.9$  and  $162.6 \pm 2.6$  Ma using sericite  
31  
32 137 Ar-Ar and molybdenite Re-Os methods, respectively. Wang, F. (2017) subsequently obtained an age of  
33  
34 138  $159 \pm 6$  Ma by applying the Re-Os method to arsenopyrite and pyrite, and  $148 \pm 1$  Ma using the U-Pb  
35  
36 139 method (hydrothermal zircon). Finally, Gu et al. (2017) obtained a zircon U-Pb age for the Mo-  
37  
38 140 mineralized granite porphyry of  $133.4 \pm 1.2$  Ma, which they proposed was associated with the Ag-Pb-  
39  
40 141 Zn mineralization.  
41

42 142 In this contribution, we present the results of a comprehensive investigation of the Shuangjianzishan  
43  
44 143 Ag-Pb-Zn deposit, utilizing ore mineralogical, textural, petrochemical, sulfide Re-Os and zircon U-Pb  
45  
46 144 geochronological, and in situ S and Pb isotopic data. Our new data are used to constrain the source and  
47  
48 145 nature of the hydrothermal fluid, the metal source, and the timing of ore mineral deposition, and to  
49  
50 146 determine its genetic relationship to the porphyry intrusion. The results of this study show that the Ag-  
51  
52 147 Pb-Zn veins are part of a magmatic-hydrothermal system related to a nearby Mo-mineralized granite  
53  
54 148 porphyry and reflect the relatively high solubility of the metals (e.g., Ag, Pb, and Zn), which facilitated  
55  
56 149 their transport to the distal parts of the system, where they were deposited in pre-existing faults or  
57  
58 150 fractures created by magma withdrawal during the waning stages of magmatic-hydrothermal activity.  
59  
60

151 **Regional Geology**

152 The Shuangjianshan Ag-Pb-Zn deposit is located in the Great Hinggan Range (GHR) Metallogenic  
153 Belt, which lies in the easternmost segment of the Central Asian Orogenic Belt (CAOB) (Fig. 1A). The  
154 CAOB evolved through complex closure of the Paleo-Asian Ocean from the Neoproterozoic to the late  
155 Permian (Wilde, 2015), which separated the Siberian craton in the north from the Tarim and North China  
156 cratons in the south (Fig. 1A). It formed via successive accretion of arc complexes, accompanied by the  
157 emplacement of immense volumes of granitic magma (Jahn et al., 2000), and is believed to have been  
158 the world's largest site of juvenile crust formation in the Phanerozoic era (Jahn, 2004). This region  
159 records complex processes involving tectonic events that marked the transition in the late Permian-  
160 Early Triassic from the dominantly NE-SW directed motion of the Paleo-Asian plate to the E-W directed  
161 motion of the Paleo-Pacific plate (e.g., Li, 2006; Wilde, 2015; Zhou et al., 2018, and references therein).

162 The tectonic evolution of the CAOB since the late Permian can be summarized briefly as follows: (i)  
163 closure of the Paleo-Asian Ocean was completed in the late Permian (~260 Ma); (ii) a switch in  
164 geodynamic setting took place in the late Permian-Early Triassic (~260-250 Ma) that is reflected by the  
165 Paleo-Asian Ocean closure and the onset of tectonism associated with subduction of the Paleo-Pacific  
166 plate; (iii) events associated with the westward advance of the Paleo-Pacific plate in the Early Jurassic-  
167 early Cretaceous (~250-140 Ma); and (iv) the slab rollback of the Paleo-Pacific plate after the early  
168 Cretaceous (~140 Ma), which created an extensional setting associated with thinning and delamination  
169 of the lithosphere (e.g., Li, 2006; Wang et al., 2006; Zhang et al., 2010; Wu et al., 2011; Wilde, 2015; Liu,  
170 K., et al., 2017; Zhou et al., 2018, and references therein). The region underwent widespread Mesozoic  
171 volcanic and intrusive activity (Fig. 1B), including emplacement of I- and A-type granitoids at different  
172 stages (i.e., Early to Late Triassic and late Jurassic to early Cretaceous) of the geotectonic evolution (Xiao  
173 et al., 2004; Wu et al., 2005, 2011), which today underlie >50% of the surface area in the mountainous  
174 regions (HBGMR, 1993). Compared with other areas in the CAOB, NE China was strongly affected by  
175 Paleo-Pacific subduction and, as a result, is one of the most metallogenically important areas of the  
176 eastern Asian Mesozoic continental margin (Wu et al., 2011).

177 The southern segment of the GHR Metallogenic Belt hosts numerous porphyry Mo-(Cu), skarn Fe-  
178 (Sn), and Ag-Pb-Zn vein deposits (Fig. 1C; Ouyang et al., 2014; Shu et al., 2016; Chen, Y., et al., 2017;  
179 Gao et al., 2018; Zhai et al., 2018b). These deposits are hosted mainly by Permian strata and Mesozoic  
180 granites (Fig. 1C), the latter of which were produced during regional Mesozoic magmatism (Mao et al.,

1 181 2014; Ouyang et al., 2015; Shu et al., 2016; Zhai et al., 2017; Chen, Y., et al., 2017; Gao et al., 2018, and  
2 182 references therein). Recent exploration has revealed that Ag-Pb-Zn vein deposits are very common in  
3  
4 183 the region (Fig. 1C), as shown by discovery of the Shuangjianzishan, Bianjiadayuan, Bairendaba and  
5  
6 184 Weilasituo deposits (e.g., Ouyang et al., 2014; Liu, Y., et al., 2016; Wang et al., 2017; Zhai et al., 2018c),  
7  
8 185 which define the southern segment of the GHR that is the most important Ag-Pb-Zn metallogenic belt  
9  
10 186 in northern China.

11  
12 187 Available geochronological data indicate that magmatic-hydrothermal deposits in this area formed  
13  
14 188 during two distinct metallogenic events, namely, an early event in the Permian and Triassic (~290 to 230  
15  
16 189 Ma; Wan et al., 2009; Zhou et al., 2014; Duan et al., 2015; Jiang, S., et al., 2017) and a late event in the  
17  
18 190 Jurassic and Cretaceous (~160 to 130 Ma; Zeng et al., 2015; Ouyang et al., 2015; Liu, Y., et al., 2016;  
19  
20 191 Wang et al., 2017; Jiang, S., et al., 2017). Numerous age determinations of porphyry Mo-(Cu) and skarn  
21  
22 192 Fe-(Sn) deposits suggest that the magmatic-hydrothermal systems developed mainly during the second  
23  
24 193 metallogenic event (Fig. 1C), synchronously with granite emplacement (Mao et al., 2014; Ouyang et al.,  
25  
26 194 2015; Shu et al., 2016; Zhai et al., 2017; Gao et al., 2018). However, reliable ages for the vein-type Ag-  
27  
28 195 Pb-Zn mineralization are generally lacking, mostly because these deposits have received much less study,  
29  
30 196 and more importantly, because of the paucity of minerals that can be easily and accurately dated.  
31  
32 197 However, the ages of some of these deposits have been estimated reliably where it has been possible  
33  
34 198 to establish a close genetic association between the porphyry and polymetallic vein-type mineralization  
35  
36 199 (e.g., the Bianjiadayuan and Weilasituo deposits; Zhai et al., 2017; Wang et al., 2017).

### 200 **Ore Deposit Geology**

201 The main rock-types exposed in the Shuangjianzishan ore district are late Permian slates, Mesozoic  
202 volcanic rocks and Quaternary gravel (Fig. 2A). The Permian slates are part of the Dashizhai Formation,  
203 and form >30% of the surface outcrop in the mine area (Fig. 2A). The slates are >950m thick, and  
204 generally strike NE and dip NW at 55-65°. They are the main host to the ores (Fig. 2A, B). The volcanic  
205 rocks are located mainly to the southeast of the Ag-Pb-Zn mineralized zones, unconformably overlie the  
206 slates (Fig. 2A) and are interpreted to have been emplaced in the Jurassic (Wu et al., 2014). They belong  
207 mainly to the Xinmin Formation, and consist largely of dacite lava and rhyolitic tuff with a thickness  
208 of >200 m; some of the Ag-Pb-Zn mineralized veins crosscut these rock units (Fig. 2A). Quaternary  
209 gravels, which consist of unsorted rock fragments and are 15 to 50 m thick, cover much of the district  
210 (Fig. 2A).

1 211 The only exposed intrusive rock in the district is a granitic pluton located ~2 km to the north of the  
2 212 Shuangjianzishan ore deposit (Fig. 2A). An unexposed granite porphyry intrusion was intersected in the  
3 213 core of drill hole ZK12-37 from a depth of 516 m to the bottom of the hole at 1080 m. This intrusion is  
4 214 located approximately 800 m to the northwest of the main mineralized veins (Fig. 2A). Texturally, the  
5 215 porphyry has been subdivided into a lower coarse-grained facies and an upper fine-grained facies that  
6 216 intrudes the coarse-grained facies and is observed to a depth of 846 m (Fig. 3A). The fine-grained facies  
7 217 shows evidence of having undergone strong potassic and silicic alteration, and contains numerous  
8 218 quartz-molybdenite veins (0.1 to 2 cm width). Numerous K-feldspar-quartz veinlets/stockworks and less  
9 219 abundant magmatic-hydrothermal breccias cemented by minor Mo mineralization also occur in the  
10 220 fine-grained porphyry (Fig. 3A). In contrast, the coarse-grained facies is only altered near its contact  
11 221 with the fine-grained facies and is unaltered at depth and free of quartz-molybdenite veins. The  
12 222 overlying slates have been sericitized and silicified for ~150 m above the fine-grained porphyry and  
13 223 locally contain molybdenite-quartz ± albite veins/veinlets and zones of hydrothermal brecciation (Fig.  
14 224 3A). On the basis of the above observations, we speculate that the fine-grained porphyry may be  
15 225 genetically related to the Ag-Pb-Zn mineralization considered in this paper. In addition to the granitic  
16 226 pluton and granite porphyry, there are diorite and granodiorite dikes that strike NW or NE, dip ~60° to  
17 227 the SE, vary in width from 1 to 8 m, and have been traced along strike for distances of 50 to 300 m.  
18 228 Several of these dikes are crosscut by the Ag-Pb-Zn mineralized veins (Figs. 2A and 3B), indicating that  
19 229 they were intruded prior to the mineralization.

20 230 The major faults in the district have NW-, NE- and NS-strikes. However, most Shuangjianzishan Ag-  
21 231 Pb-Zn veins were emplaced parallel to a NW-striking fault zone (Fig. 2A). This fault zone varies in width  
22 232 from 500 to 800 m, strikes 300-310°, dips NE at 55 to 65° and has been traced for a distance of > 5000  
23 233 m. These faults are characterized by extensional shear features. A few veins were emplaced in a NE-  
24 234 striking fault zone (Fig. 2A), which strikes 30-50° and dips SE at ~60°. Minor veins are also hosted by the  
25 235 NS-striking fault zones (Fig. 2A). The NW- and NE-striking faults are observed to have been truncated by  
26 236 some of the Ag-Pb-Zn-barren NS-striking faults.

27 237 The Shuangjianzishan Ag-Pb-Zn deposit was discovered in 2013 and has been mined since that time.  
28 238 More than 70 major veins and numerous stockworks and disseminations have been identified, all of  
29 239 which are hosted by the Permian slate. According to a 2018 exploration report (Zhang, 2018), the  
30 240 deposit has a total resource of 145 Mt of ore containing >18.6 Kt of Ag with an average grade of 128.5

1 241 g/t, 0.87 Mt of Pb with an average grade of 0.6 wt.% and 2.32 Mt of Zn with an average grade of 1.6  
2 242 wt.%. This makes Shuangjianzishan the largest Ag deposit in Asia (Kuang et al., 2014). Two separate ore  
3  
4 243 zones 4.7 km apart, namely Shuangjianzishan in the west and Xinglongshan in the east, have been  
5  
6 244 identified (Kuang et al., 2014). The bulk of the economic mineralization, however, is in the eastern ore  
7  
8 245 zone (Fig. 2A). Although several oxidized veins are exposed in slate outcrops (Fig. 4A), most of the  
9  
10 246 mineralized veins are not exposed (Fig. 4B-D). Mineralized veins fill fractures that strike  $\sim 310^\circ$  and dip  
11  
12 247 SW at  $50\text{-}60^\circ$ , whereas they are sparse in the NE- and NS-striking fault zones. The orebodies comprise  
13  
14 248 sets of parallel veins concentrated in zones ranging from 2 to 10 m in width, although locally these zones  
15  
16 249 range up to 30 m in width; individual veins range up to 10 m in width (Fig. 4B, C). They (the orebodies)  
17  
18 250 generally have strike lengths between 100 and 800 m, and extend vertically  $\sim 500$  m (Fig. 2B). Stockwork  
19  
20 251 veins and disseminated mineralization have been discovered adjacent to the major veins (Fig. 4B) or in  
21  
22 252 structural domains associated with faults having orientations different from those controlling the major  
23  
24 253 veins.

25  
26  
27 254 Hydrothermal alteration is intense around the major Ag-Pb-Zn mineralized veins, and is characterized  
28  
29 255 by an assemblage of sericite, chlorite, quartz, and calcite. This alteration is concentrated in halos that  
30  
31 256 are distributed symmetrically on the two sides of the mineralized veins (Fig. 4B, C). In addition, the slates  
32  
33 257 have experienced silicification and subordinate weaker potassic alteration (secondary K-feldspar), which  
34  
35 258 predated the main sulfide mineralization. This alteration is associated with euhedral pyrite, or locally  
36  
37 259 pyrite-quartz veins. The latter are consistently cut by the main mineralized veins (Fig. 4D). The alteration  
38  
39 260 associated with the Ag-Pb-Zn veins (Fig. 4D-G) includes a sub-assemblage of quartz-sericite  $\pm$  chlorite  
40  
41 261 that was closely related to Ag mineral deposition (Fig. 4E), particularly the very high grade and massive  
42  
43 262 ores (Fig. 4E, F). The final stage of alteration is represented by quartz, which occurs as narrow veins (1-  
44  
45 263 5 mm width) cutting the Ag-Pb-Zn mineralized veins (Fig. 4D).

## 264 **Sampling and analytical methods**

### 265 **Ore mineral textures and compositions**

266 More than ninety samples were collected from different mining levels and drill holes from the  
267 Shuangjianzishan deposit and more than 120 polished thin sections were examined in reflected and  
268 transmitted light. A Zeiss Supra 55 Sapphire field emission scanning electron microscope (FESEM)  
269 coupled with an Oxford energy-dispersive X-ray spectrometer (EDS), located at the China University of  
270 Geosciences Beijing (CUGB), was used to identify the minerals by determining their compositions semi-

1 271 quantitatively and imaging textural relationships among them. Element line scanning was undertaken  
2 272 for Ag L $\alpha$ , Sb L $\alpha$ , Pb M $\alpha$ , Fe K $\alpha$ , Cu K $\alpha$ , Se K $\alpha$ , and S K $\alpha$  using an accelerating voltage of 20 kV and a  
3  
4 273 working distance of 15 mm. An in-lens detector for secondary electron imaging was used to characterize  
5  
6 274 topographic features, and an AsB detector was used to visualize compositional differences among the  
7  
8 275 minerals (backscattered electron images). Samples were coated with an ~10 nm thick platinum film for  
9  
10 276 electric conduction before analysis.

11  
12 277 The compositions of the sulfides and sulfosalts were determined using a JEOL 8230 Superprobe  
13  
14 278 equipped with wavelength- and energy-dispersive X-ray detectors and a back-scatter electron detector  
15  
16 279 at the Microprobe Center, Chinese Academy of Geological Sciences (CAGS). The accelerating voltage  
17  
18 280 was 20 kV. The beam current and counting times for the major elements were 20 nA and 20 s,  
19  
20 281 respectively (10 s for background measurement), and the beam diameter was 1  $\mu$ m. Natural and  
21  
22 282 synthetic mineral standards of chalcopyrite, sphalerite, galena, pyrrhotite, InAs and native Ag, Sb, Se,  
23  
24 283 Sn were utilized for calibration. The X-ray lines measured were Ag L $\alpha$ , Sb L $\alpha$ , As L $\alpha$ , Pb L $\alpha$ , Zn L $\alpha$ , Sn L $\alpha$ ,  
25  
26 284 Fe K $\alpha$ , Cu K $\alpha$ , Se K $\alpha$ , and S K $\alpha$ . X-ray element mapping was performed using the energy-dispersive X-ray  
27  
28 285 detector. The dwell time was set to 20  $\mu$ s to provide the highest possible resolution.

### 31 286 **Whole rock geochemistry**

32  
33 287 Eleven rock samples collected from drill cores and underground tunnels in the Shuangjianzishan ore  
34  
35 288 district were analyzed for their whole rock compositions. The samples comprise fine-grained granite  
36  
37 289 porphyry (4), coarse-grained granite porphyry (3), diorite to granodiorite dikes (2), granite (1) and dacite  
38  
39 290 (1). Powders of the samples were prepared by crushing with corundum plates and grinding in an agate  
40  
41 291 disk mill at the Hebei Geological Survey, China. Major element concentrations were analyzed by ICP-  
42  
43 292 OES, and trace element concentrations by ICP-MS (Agilent-7500a) at CUGB. The precision for the major  
44  
45 293 elements, as determined by the reproducibility of laboratory standards and duplicates, was better than  
46  
47 294 1%, with the exception of TiO<sub>2</sub> (~1.5%) and P<sub>2</sub>O<sub>5</sub> (~2.0%), and for minor and trace elements was better  
48  
49 295 than 10%. The results of the analyses are reported in Table 1. Most of the samples analyzed in this study  
50  
51 296 are relatively fresh and have low loss on ignition (LOI;  $\leq$  1.5 wt.%), except for the two diorite-  
52  
53 297 granodiorite dikes and the dacite, both of which were altered.

### 54 298 **In situ S and Pb isotopes**

55  
56  
57  
58 299 Fifteen samples were collected for in situ sulfur and lead isotope analysis from several mining levels  
59  
60 300 and drill cores, and are representative of the variety of mineralization in the Ag-Pb-Zn veins. Prior to

1 301 analysis, the thin sections were carefully observed with an optical microscope and FESEM, and analyzed  
2 302 with an electron microprobe (EPM) to establish the textural relationships and determine mineral  
3 303 compositions. Sulfur and lead isotopes were analyzed using a femtosecond laser ablation coupled multi-  
4 304 collector inductively coupled plasma mass spectrometer (fsLA-MC-ICP-MS) at the State Key Laboratory  
5 305 of Continental Dynamics, Northwest University, China. Details of the analytical methods for S and Pb  
6 306 isotopes have been reported by Chen, L., et al. (2017) and Yuan et al. (2015), respectively. These  
7 307 analyses were supplemented by analyses carried out using a 266 nm NWR UP Femto, femtosecond (fs)  
8 308 laser ablation system (ESI, U.S.A.) coupled to Nu Plasma 1700 (NP-1700) and Nu Plasma II (NP-II) MC-  
9 309 ICP-MS (Nu Instruments, Wrexham, U.K.), respectively. The surfaces of the polished thin sections were  
10 310 cleaned with milli-Q water (18.2 MΩ·cm). Argon flow rates and voltage were adjusted to give the best signal  
11 311 stability and intensity. Each sample acquisition consisted of background collection for 30 s, followed by ablation  
12 312 signal collection for 70 s, and a wash time of 50 s to reduce memory effects. The analyses employed a relatively  
13 313 low laser energy (the fluence ranged from 0.5 to 3.5 J cm<sup>-2</sup>), a 10 Hz frequency and an ablation rate of 2 μm/s.  
14 314 The spot size for sulfur and lead were 20-37 and 9-40 μm, respectively. Instrument drift and mass bias  
15 315 were corrected using a sample-standard bracketing approach with repeated measurement of the standard  
16 316 before and after each sample. The international standard, NBS123 (sphalerite) and internal standards of  
17 317 PY-4 (pyrite), CBI-3 (galena), PSPT-3 (sphalerite), CPY-1 (chalcopyrite), and IAEA-S-1 (Ag<sub>2</sub>S) were used  
18 318 for calibration in the sulfur isotope analyses. The analytical precision calculated from replicate analyses  
19 319 of unknown samples is better than 0.2‰ (1σ). The measured δ<sup>34</sup>S<sub>VCDT</sub> value of 17.8 ± 0.3‰ (n=156) for  
20 320 standard NBS123 is consistent with the reported value of 17.4 ± 0.2‰ (Craddock et al., 2008). The TI  
21 321 NIST SRM 997 (20 ppb, <sup>205</sup>Tl/<sup>203</sup>Tl = 2.38890) and NIST SRM 610 glass were used as internal and external  
22 322 Pb isotope standards, respectively. Repeated analyses of the NIST SRM 610 glass standard yielded highly  
23 323 reliable and reproducible results with mean <sup>206</sup>Pb/<sup>204</sup>Pb, <sup>207</sup>Pb/<sup>204</sup>Pb, and <sup>208</sup>Pb/<sup>204</sup>Pb ratios of 17.050 ±  
24 324 0.004, 15.510 ± 0.002, and 36.985 ± 0.006 (1σ, n = 63), respectively, which are very close to the reported  
25 325 reference ratios (Stern and Amelin, 2003).

### 326 **Zircon U-Pb dating**

327 Five rock samples were selected for zircon U-Pb dating. These comprise granite porphyry (fine- and  
328 coarse-grained) (Fig. 3A), granite intrusion (~2 km north of the vein system), diorite dike and dacite (Fig.  
329 3B). Zircon crystals from the selected samples were separated by standard heavy-liquid and magnetic  
330 techniques, followed by hand-picking under a binocular microscope. Prior to LA-ICP-MS analysis, the

1 331 zircon crystals were imaged by cathodoluminescence (CL) with a FESEM at Peking University. The U-Pb  
2 332 age determinations were carried out using a LA-ICP-MS in the State Key Laboratory of Geological  
3  
4 333 Processes and Mineral Resources at CUGB. The crystals were ablated using an excimer laser ablation  
5  
6 334 system (UP193SS). An Agilent 7500a ICP-MS instrument was used to acquire ion-signal intensities. A  
7  
8 335 laser spot size of 36  $\mu\text{m}$ , laser energy density of 8.5 J/cm<sup>2</sup> and a repetition rate of 10 Hz were applied  
9  
10 336 during analysis. Helium and argon were used as the carrier and make-up gases, and were mixed via a  
11  
12 337 T-connector before entering the ICP-MS. Uranium, Th and Pb concentrations were calibrated by using  
13  
14 338 <sup>29</sup>Si as an internal standard and NIST 610 glass as the reference standard. The <sup>207</sup>Pb/<sup>206</sup>Pb, <sup>206</sup>Pb/<sup>238</sup>U,  
15  
16 339 <sup>207</sup>Pb/<sup>235</sup>U and <sup>208</sup>Pb/<sup>232</sup>Th ratios were calculated using the GLITTER 4.4.1 software and corrected for  
17  
18 340 both instrumental mass bias and depth-dependent elemental and isotopic fractionation using Harvard  
19  
20 341 zircon 91500 as the external standard (Wiedenbeck et al., 1995). The zircon standard, TEMORA, was  
21  
22 342 used as a secondary standard to monitor the deviation of the age measurement/calculation (Black et  
23  
24 343 al., 2003). The Harvard zircon 91500 and TEMORA zircon standards yielded weighted mean ages of  
25  
26 344 1062.5  $\pm$  0.5 and 418.0  $\pm$  6.9 Ma, respectively, which are very similar to the reported ages (i.e., 1065  
27  
28 345 and 417 Ma; Wiedenbeck et al., 1995; Black et al., 2003). Isoplot 3.0 was used to calculate the U-Pb  
29  
30 346 ages and to make the Concordia plots (Ludwig, 2003).

#### 33 347 **Molybdenite and pyrite Re-Os dating**

34 348 Three molybdenite-quartz veins/veinlets (0.5-2 cm) in the altered slate above the granite porphyry  
35  
36 349 were analyzed for their molybdenite Re-Os isotope ratios (Fig. 3A). To date, no molybdenite has been  
37  
38 350 found in the Ag-Pb-Zn mineralized veins. The grain size of the molybdenite typically ranges from 0.1 to  
39  
40 351 0.3 mm (Fig. 3A). The Re-Os ratios of four pyrite separates from the main Ag-Pb-Zn veins sampled at  
41  
42 352 depths of 240 to 410 m were also analyzed (Fig. 3B). The pyrite grain-size ranges from 3 to 5 mm. The  
43  
44 353 mineral separates of both the molybdenite and pyrite samples were obtained using conventional  
45  
46 354 methods (i.e., crushing, washing, sieving, magnetic separation, and heavy liquid separation) followed  
47  
48 355 by hand picking under a binocular microscope.

49  
50  
51 356 The rhenium-osmium analyses were carried out at the Laboratory for Sulfide and Source Rock  
52  
53 357 Geochronology and Geochemistry at Durham University, United Kingdom. For molybdenite, a weighed  
54  
55 358 aliquot (~21 to 61 mg) of the mineral separate plus a known amount of spike solution (<sup>185</sup>Re +  
56  
57 359 isotopically normal Os) were loaded into a Carius tube with 11N HCl (1 ml) and 15.5N HNO<sub>3</sub> (3 ml),  
58  
59 360 sealed, and digested at 220°C for ~24 h. For pyrite, ~0.4 g of sample, together with a mixed spike of

1 361  $^{185}\text{Re} + ^{190}\text{Os}$ , were loaded into a Carius tube with 11N HCl (3 ml) and 15.5N  $\text{HNO}_3$  (6 ml), sealed, and  
2 362 digested at 220°C for ~24 h. For both sample types, Os was purified from the acid medium using solvent  
3 363 extraction ( $\text{CHCl}_3$ ) at room temperature and microdistillation methods. The Re fraction was purified by  
4 364 NaOH-solvent extraction and anion chromatography. The Re and Os isotopic compositions were  
5 365 measured by negative thermal ionization mass spectrometry (N-TIMS) using a Thermo Scientific TRITON  
6 366 mass spectrometer; the Re and Os isotope compositions were measured using the static Faraday  
7 367 collection mode for molybdenite, and SEM in peak hopping mode for the pyrite Os fraction. All Re-Os  
8 368 uncertainties are reported at the  $2\sigma$  absolute level, which followed the propagation of uncertainties  
9 369 related to Re and Os mass spectrometer measurements, blank determinations, spike and standard  
10 370 isotopic compositions, and calibration uncertainties of  $^{185}\text{Re}$  and  $^{187}\text{Os}$ . During the analyses, the Re and  
11 371 Os blanks were < 2.5 and 0.1 pg, respectively, and the  $^{187}\text{Os}/^{188}\text{Os}$  ratio of the blank was  $0.22 \pm 0.02$ .  
12 372 Results of analyses of the Henderson molybdenite reference material (RM8599 -  $27.695 \pm 0.038$  Ma)  
13 373 provided by Li et al. (2017) overlapped with those of this study. A  $^{187}\text{Re}$  decay constant of  $1.666 \times 10^{-11} \text{y}^{-1}$   
14 374 with an uncertainty of 0.31% was used in the calculation of the Re-Os dates (Smoliar et al., 1996; Selby  
15 375 et al., 2007).

## 31 376 **Results**

### 33 377 **Ore mineralogy and paragenesis**

34 378 Crosscutting relationships involving the different types of veins and textural relationships among the  
35 379 ore and gangue minerals show that the Ag-Pb-Zn mineralization at Shuangjianzishan occurred in three  
36 380 discrete stages (Fig. 4C, D): an early pyrite+quartz±K-feldspar stage (I), a  
37 381 sulfide+sulfosalt+quartz+calcite+sericite+chlorite±epidote stage (the main ore stage II) and a late quartz  
38 382 stage (III) (Fig. 5). The quartz-pyrite±K-feldspar assemblage occurs mainly in thin veins/veinlets (~2 to  
39 383 10 mm in width) accompanied by potassic alteration halos (K-feldspar), and pyrite less commonly occurs  
40 384 as disseminations in the silicified slate. Pyrite in these veins/veinlets is relatively coarse-grained (~0.1  
41 385 mm in diameter) and euhedral, occurring either as cubes or pyritohedra. The early veins/veinlets were  
42 386 crosscut, replaced or included as fragments in the main ore stage veins (Fig. 4C), in which sphalerite,  
43 387 galena, pyrite, quartz and calcite are the main minerals and are accompanied by subordinate  
44 388 proportions of Ag-bearing minerals and chalcopyrite. The main ore stage has been further subdivided  
45 389 into substages II-1 and II-2 (Fig. 5). Substage II-1 is represented by the ore mineral assemblage of  
46 390 galena+sphalerite+pyrite+chalcopyrite±canfieldite±freibergite and an alteration/gangue assemblage of

1 391 quartz+calcite+chlorite±epidote±sericite. This substage corresponded to a period of abundant sulfide  
2 392 deposition but minor Ag mineralization. The EPM results reveal that the base metal sulfides commonly  
3  
4 393 do not contain any silver (Electronic Appendix Table A1), indicating that silver mineralization was very  
5  
6 394 limited in the early Substage II-1.

7  
8 395 The main Ag stage was Substage II-2, which is represented by Ag-bearing sulfosalts and  
9  
10 396 argentite±galena±sphalerite±chalcopryrite and an alteration/gangue assemblage of  
11  
12 397 quartz+sericite±calcite±chlorite (Fig. 5). Although we have subdivided the main ore stage into two  
13  
14 398 substages, it is noteworthy that both substages can be observed in the same veins, suggesting that they  
15  
16 399 belong to a single continuous stage (Fig. 5). Chemically, the paragenesis for the mineralization  
17  
18 400 corresponds to an evolution from Fe-S through Pb-Zn-Fe-Cu-S to Ag-Cu-Sn-Sb-Se-S (Fig. 5).

19  
20 401 The Ag-bearing minerals crystallized in Substage II-2. In order of relative abundance, they are  
21  
22 402 canfieldite ( $\text{Ag}_8\text{SnS}_6$ ), argentite ( $\text{Ag}_2\text{S}$ ), freibergite  $[(\text{Ag}, \text{Cu})_{10}(\text{Fe}, \text{Zn})_2\text{Sb}_4\text{S}_{13}]$ , polybasite  
23  
24 403 ( $\text{Ag}_9\text{CuS}_4\text{Ag}_4\text{Cu}_2\text{Sb}_{1.25}\text{As}_{0.75}\text{S}_7$ ), pyrargyrite ( $\text{Ag}_3\text{SbS}_3$ ), and stephanite ( $\text{Ag}_5\text{SbS}_4$ ). Minor native silver and  
25  
26 404 electrum also have been observed (Wu et al., 2014). The other minor sulfides in this substage generally  
27  
28 405 do not contain Ag, except for galena, which may contain up to 7 wt.% Ag but more typically contains  
29  
30 406 <0.5 wt.% Ag.

31  
32 407 Canfieldite, argentite and freibergite are the most abundant Ag-bearing ore minerals in the deposit,  
33  
34 408 making up >80 vol.% of the Ag budget based on petrographic observations. Canfieldite is usually  
35  
36 409 associated with argentite and freibergite, both of which commonly are associated with the earlier  
37  
38 410 sulfides (e.g., sphalerite and galena) along their crystal boundaries (Fig. 6A-D), or occur interstitially to  
39  
40 411 base metal sulfides (e.g., sphalerite and chalcopryrite; Fig. 6A, B), showing that these Ag-bearing  
41  
42 412 minerals formed late relative to the base metal sulfides. Canfieldite has Ag, Sn, and S contents that  
43  
44 413 range from 59.7 to 69.4, 9.5 to 19.3, and 10.6 to 21.3 wt.%, respectively (Electronic Appendix Table A1).  
45  
46 414 The selenium content varies from below the detection limit (0.01 wt.%) to 11.6 wt.% (Zhai et al., 2019c),  
47  
48 415 and is heterogeneously distributed within individual crystals (Fig. 7). Canfieldite is the only mineral that  
49  
50 416 contains significant Se. There are also minor to trace amounts of Cu, Fe, and Te.

51  
52 417 Argentite commonly replaced Stage II-1 sulfides, mainly sphalerite, galena (Fig. 6A), and chalcopryrite  
53  
54 418 (Fig. 6B), and is intergrown with sericite and quartz; larger grains (>100  $\mu\text{m}$ ) commonly enclose the base  
55  
56 419 metal sulfides (e.g., chalcopryrite and galena; Fig. 6E). Argentite also occurs in fine veinlets (20 to 50  $\mu\text{m}$   
57  
58 420 wide) that crosscut argentinian galena (Fig. 6F). The Ag content of the argentite ranges from 71.8 to 84.5  
59  
60

1 421 wt.%. There are also minor proportions of Sb and As, and in some cases Se. Freibergite, which as noted  
2 422 above, is commonly associated with canfieldite (Fig. 6C, D), is intergrown with or replaced base metal  
3 423 sulfides, particularly galena (Fig. 6F-H). It occurs both as large grains (e.g., >200  $\mu\text{m}$ ) and small cusped-  
4 424 shaped irregular inclusions in galena (Fig. 6F, G); these galena-hosted inclusions also include pyrrargyrite  
5 425 and minor pyrrhotite (Fig. 6G). The Ag, Cu and Sb contents of the freibergite vary from 19.4 to 42.1 wt.%,  
6 426 11.9 to 25.1 wt.% and 19.3 to 25.8 wt.%, respectively, which span the compositional range from  
7 427 argentine tetrahedrite to freibergite. There are also significant concentrations of Fe (1.0 to 5.1 wt.%)  
8 428 and Zn (0.6 to 4.3 wt.%). The tennantite component is small (0.8 to 1.4 wt.% As). Among the remaining  
9 429 Ag minerals, pyrrargyrite is the most important phase and commonly occurs as intergrowths with galena  
10 430 and in rare cases traces with pyrrhotite (Fig. 6G). Lesser proportions of stephanite and polybasite occur  
11 431 as intergrowths with freibergite and replaced galena and sphalerite (Fig. 6H, I).

### 22 432 **Lithogeochemistry**

23 433 Compositionally, the granite and granite porphyry are very similar and plot in the subalkaline granite  
24 434 field on a TAS discrimination diagram (Electronic Appendix Fig. A1). In chemical affinity, the porphyry  
25 435 varies from metaluminous to peraluminous (Electronic Appendix Fig. A2F), and belongs to the high-K  
26 436 calc-alkaline family (Electronic Appendix Fig. A2E). The fine-grained granite porphyry has the highest  
27 437  $\text{SiO}_2$  content among all the analyzed samples (mostly due to the silicic alteration), i.e., from 75.7 to  
28 438 80.0 wt.%, whereas the  $\text{SiO}_2$  content of the coarse-grained granite porphyry varies from 69.6 to  
29 439 70.0 wt.%. Both the fine- and coarse-grained granite porphyry samples have similarly high  $\text{K}_2\text{O}$  contents,  
30 440 from 4.0 to 4.9 wt.%, whereas the  $\text{Na}_2\text{O}$  content of the coarse-grained porphyry is considerably higher  
31 441 (4.1 to 4.6 wt.%) than that of the fine-grained porphyry (2.2 to 3.7 wt.%). The  $\text{K}_2\text{O}$  content for both  
32 442 facies increases and the  $\text{Al}_2\text{O}_3$ , CaO, MgO,  $\text{FeO}^{\text{T}}$ ,  $\text{TiO}_2$  and  $\text{P}_2\text{O}_5$  contents decrease with increasing  $\text{SiO}_2$   
33 443 content (Electronic Appendix Fig. A2A-E), as is the case for subalkaline granite suites globally (Whalen  
34 444 et al., 1987). The dacite sample has a relatively low silica content (65.0 wt.%  $\text{SiO}_2$ ), and the two samples  
35 445 of diorite to granodiorite dikes also have low but variable silica contents (54.2 and 67.3 wt.%  $\text{SiO}_2$ ), due  
36 446 possibly to the effects of hydrothermal alteration, as suggested by their relatively high LOI (2.6 to 4.1  
37 447 wt.%; Table 1).

38 448 The granite porphyry samples (both fine-grained and coarse-grained) have relatively low Sr/Y (<10)  
39 449 and La/Yb (<20) values, low Sr (mostly <300 ppm), Rb (mostly <300 ppm) and Nb (mostly <20 ppm)  
40 450 contents, and high Y contents (mostly >30 ppm) (Table 1). They also have chondrite-normalized profiles

1 451 that display moderate enrichment of the light REE and negative Eu anomalies ( $Eu_n/Eu^* < 0.7$ ) (Electronic  
2 Appendix Fig. A3A); the average  $[La/Yb]_N$  is  $7.0 \pm 3.4$  ( $n = 21$ ). The fine-grained porphyry, however, has  
3 452 a more negative Eu anomaly ( $Eu_n/Eu^* < 0.2$ ) than the coarse-grained facies ( $Eu_n/Eu^* > 0.3$ ). Both  
4 453 porphyry facies are relatively depleted in Ba, Nb, Sr, P, Eu, and Ti, and enriched in U, La, and Nd relative  
5 454 to primitive mantle (Electronic Appendix Fig. A3B).  
6  
7  
8  
9 455

#### 10 456 **In situ S and Pb isotope compositions**

11 457 The range of  $\delta^{34}S$  values for all the sulfides and sulfosalts is relatively restricted, from -4.67 to +2.44‰  
12 458 (Figs. 8, 9A) and largely independent of the depth in the deposit from which the samples were taken.  
13 459 Moreover, those for sphalerite (mean = -1.41‰), pyrite (mean = -1.27‰), chalcopyrite (mean = -1.58‰)  
14 460 and arsenopyrite (mean = -1.34‰) are comparable to the values for freibergite (mean = -1.17‰) and  
15 461 canfieldite (mean = -1.54‰) (Table 2). The  $\delta^{34}S$  values for galena (mean = -3.58 ‰), however, are  
16 462 somewhat lower (Fig. 9A, B) and those for pyrrargyrite are significantly higher (mean = +2.0‰). The  $\delta^{34}S$   
17 463 values decrease in the order of pyrite > sphalerite > chalcopyrite > galena based on the analyses of a  
18 464 given assemblage in the same ore stage, which is consistent with the experimentally determined  
19 465 equilibrium sulfur isotope fractionation factors for  $^{32}S$  and  $^{34}S$  between the fluid and sulfide minerals  
20 466 (Seal, 2006, and references therein) and likely indicates contemporaneous deposition of these sulfides  
21 467 from the ore fluid.  
22  
23  
24  
25  
26  
27  
28  
29  
30  
31  
32  
33  
34

35 468 Interestingly, there is a small but significant variation in the sulfur isotopic composition within single  
36 469 crystals of most of the sulfides and sulfosalts. For example, the  $\delta^{34}S$  value of the galena crystal shown  
37 470 in Figure 8A varies from -4.51 to -3.11‰ and for the crystal shown in Figure 8B varies from -3.79 to -  
38 471 3.22‰. The variation in the  $\delta^{34}S$  values within the freibergite grains is somewhat smaller; for example,  
39 472 it is -1.72 to -1.35‰ for the grain shown in Figure 8C. In contrast, the variation is larger (+1.41 to +2.44‰)  
40 473 for pyrrargyrite, as shown by the data for the grain in Figure 8D.  
41  
42  
43  
44  
45  
46  
47

48 474 All the sulfides and sulfosalts analyzed have very similar lead isotope values (Fig. 10A, B; Table 3). The  
49 475  $^{206}Pb/^{204}Pb$ ,  $^{207}Pb/^{204}Pb$  and  $^{208}Pb/^{204}Pb$  ratios range from 18.243 to 18.310, 15.503 to 15.563, and  
50 476 38.053 to 38.203, and the mean ratios are 18.279, 15.537 and 38.143, respectively (Table 3). These  
51 477 ratios do not vary significantly with the mineral or its depth in the deposit. The  $^{206}Pb/^{204}Pb$  ratio varies  
52 478 linearly with the  $^{207}Pb/^{204}Pb$  ratio (Fig. 10A) and with the  $^{208}Pb/^{204}Pb$  ratio (Fig. 10B); the  $R^2$  values are  
53 479 0.877 and 0.786, respectively.  
54  
55  
56  
57  
58  
59

#### 60 480 **Zircon U-Pb ages**

1 481 The zircon LA-ICP-MS U-Pb isotope determinations are reported in Electronic Appendix Table A2.  
2  
3 482 The diorite dike that is crosscut by Ag-Pb-Zn veins (Fig. 3B) has a weighted mean zircon  $^{206}\text{Pb}/^{238}\text{U}$   
4  
5 483 age of  $250.2 \pm 2.0$  Ma (N = 19, MSWD = 0.3; Fig. 11A), showing that it was emplaced in the Early  
6  
7 484 Triassic. This age is indistinguishable, within the uncertainty, from those reported previously for  
8  
9 485 similar diorite dikes using the same methodology, i.e.,  $254 \pm 3$  to  $249 \pm 2$  Ma (Cui, 2015; Liu, C., et al.,  
10  
11 486 2016). The dacite, which was cut by several Ag-Pb-Zn mineralized quartz veins (Figs. 2A and 3B),  
12  
13 487 yielded a mean zircon  $^{206}\text{Pb}/^{238}\text{U}$  age of  $133.9 \pm 1.4$  Ma (N = 22, MSWD = 0.43; Fig. 11B) and thus  
14  
15 488 formed in the early Cretaceous instead of the Jurassic, as previously assumed (Wu et al., 2014). The  
16  
17 489 granite in the northern part of the district (~2 km; Fig. 2A) yielded a mean zircon  $^{206}\text{Pb}/^{238}\text{U}$  age of  
18  
19 490  $135.2 \pm 1.4$  Ma (N = 20, MSWD = 0.06; Fig. 11C), which is indistinguishable within the uncertainty  
20  
21 491 from that previously reported ( $133.7 \pm 0.6$  Ma; Wu, 2014). Identical zircon ages of  $134.4 \pm 1.0$  (N =  
22  
23 492 21, MSWD = 0.1; Fig. 11D) and  $134.4 \pm 1.0$  Ma (N = 21, MSWD = 0.2; Fig. 11E) were obtained for the  
24  
25 493 coarse- and fine-grained granite porphyry, respectively. These zircon  $^{206}\text{Pb}/^{238}\text{U}$  ages are very similar  
26  
27 494 to those reported by Zhang (2018) of  $134.4 \pm 1.7$  and  $135.9 \pm 1.1$  Ma for samples from the drill hole  
28  
29 495 (ZK12-37) considered in the current study, and are very similar to the zircon  $^{206}\text{Pb}/^{238}\text{U}$  age of another  
30  
31 496 concealed granite porphyry ( $133.4 \pm 1.2$  Ma; Gu et al., 2017) intersected in drill hole ZK12-50 ~3 km  
32  
33 497 east of the vein system.

#### 35 498 **Molybdenite and pyrite Re-Os ages**

37 499 The Re concentrations of the three molybdenite samples range from 0.12 to 2.61 ppm and the  
38  
39 500 measured  $^{187}\text{Re}$  and  $^{187}\text{Os}$  values range from 0.07 to 1.66 ppm and 0.17 to 3.77 ppb, respectively  
40  
41 501 (Table 4). The model ages for these samples are comparable, varying from  $136.3 \pm 0.9$  to  $133.7 \pm 1.2$   
42  
43 502 Ma; the weighted mean age is  $134.9 \pm 3.4$  Ma (MSWD = 9; Table 4). These ages are, within the  
44  
45 503 uncertainty, identical to the zircon  $^{206}\text{Pb}/^{238}\text{U}$  ages of the porphyry and the other granitic intrusions  
46  
47 504 in the district.

50 505 The Re and Os concentrations in the four pyrite samples range from 0.26 to 1.08 ppb and from 1.45  
51  
52 506 to 13.08 ppt (Table 5), and the  $^{187}\text{Re}/^{188}\text{Os}$  and  $^{187}\text{Os}/^{188}\text{Os}$  ratios from 496.9 to 34959.9 and 2.8 to 69,  
53  
54 507 respectively (Table 5). Two of the samples yielded very high  $^{187}\text{Re}/^{188}\text{Os}$  values (15SJ-16 = ~6300; 15SJ-  
55  
56 508 114 = ~35000), indicating that the Os fraction is dominated by radiogenic  $^{187}\text{Os}$  ( $^{187}\text{Os}^r$ ) (Stein et al.,  
57  
58 509 2000). Unfortunately, the Re-Os data did not return a meaningful isochron age for any of the pyrite  
59  
60 510 samples. We interpret this to have been due to the highly variable initial  $^{187}\text{Os}/^{188}\text{Os}$  ratio of the

1 511 samples, which may reflect multiple sources of Os (e.g., the porphyry and the host slates). Model Re-  
2 512 Os dates for three of the four pyrite separates, calculated using initial  $^{187}\text{Os}/^{188}\text{Os}$  ratios varying from  
3  
4 513  $\sim 1.1$  to 6.2, yielded a weighted mean age of  $135.0 \pm 0.6$  Ma (MSWD = 9).  
5

## 6 514 Discussion

### 7 515 Temperature of ore deposition

8 516 The temperature of ore deposition at Shuangjianzishan was estimated using a combination of ore  
9 517 mineral chemistry and stable isotope geothermometry. A temperature for the silver mineralization was  
10 518 estimated using the composition of freibergite and the fahlore geothermometer of Sack (2005), which  
11 519 was developed using an internally consistent thermodynamic database for the system  $\text{Ag}_2\text{S}-\text{Cu}_2\text{S}-\text{ZnS}-$   
12 520  $\text{FeS}-\text{Sb}_2\text{S}_3-\text{As}_2\text{S}_3$ . This geothermometer makes use of isotherms based on molar ratios of  $\text{Ag}/(\text{Ag}+\text{Cu})$  and  
13 521  $\text{Zn}/(\text{Zn}+\text{Fe})$  in fahlore. Freibergite crystals, which show no evidence of having undergone post-  
14 522 mineralization solid-state reaction and exsolution (Zhai et al., 2019a), were selected for fahlore  
15 523 geothermometry. In addition, application of the fahlore geothermometer was restricted to freibergite  
16 524 crystals with  $\text{Ag}/(\text{Ag}+\text{Cu})$  molar ratios  $< 0.55$  because of the close spacing of the isotherms at higher  
17 525 ratios and the resulting high uncertainty of the corresponding temperature estimates. The temperatures  
18 526 estimated using this geothermometer ranged from  $\sim 200^\circ$  to  $280^\circ\text{C}$  and the mean temperature was  
19 527  $\sim 240^\circ\text{C}$  ( $n = 9$ , Fig. 12).  
20  
21  
22  
23  
24  
25  
26  
27  
28  
29  
30  
31  
32  
33  
34

35 528 The mineral pairs sphalerite-galena, pyrite-galena, pyrite-sphalerite, pyrite-chalcopyrite,  
36 529 chalcopyrite-galena and sphalerite-chalcopyrite were used to estimate temperature based on the  
37 530 fractionation of  $^{32}\text{S}$  and  $^{34}\text{S}$  between these sulfide minerals and the equations of Seal (2006). Only  
38 531 mineral pairs that were in apparent textural equilibrium were used. These mineral pairs ( $n = 19$ ) yielded  
39 532 temperatures from  $142^\circ$  to  $>570^\circ\text{C}$ . The highest temperatures were for pairs involving pyrite, a  
40 533 paragenetically early mineral. If these pairs are excluded, the range of temperature estimates using  
41 534 sulfur isotope geothermometry is from  $210^\circ$  and  $320^\circ\text{C}$  (Electronic Appendix Fig. A4) and the mean  
42 535 temperature is  $\sim 250^\circ\text{C}$ .  
43  
44  
45  
46  
47  
48  
49  
50

51 536 In summary, the sulfur isotope and fahlore chemical geothermometers yielded temperatures ranging  
52 537 from  $210^\circ$  to  $320^\circ\text{C}$  (mean  $\sim 250^\circ\text{C}$ ) and  $200^\circ$  to  $280^\circ\text{C}$  (mean  $\sim 240^\circ\text{C}$ ) for the base metal and silver  
53 538 mineralization, respectively, suggesting that base metal sulfides and Ag-bearing sulfosalts precipitated  
54 539 from an intermediate- to low-temperature hydrothermal fluid. These temperatures are similar to the  
55 540 homogenization temperatures of fluid inclusions hosted in quartz reported by Wang, X. (2017), which  
56  
57  
58  
59  
60  
61  
62  
63  
64  
65

1 541 are from 170° to 260°C for the base metal sulfide and silver mineralization.

2 542 **Unusual features of the mineralogy**

3  
4 543 An unusual feature of the Shuangjianzishan deposit is that canfieldite ( $\text{Ag}_8\text{SnS}_6$ ) is one of the main  
5  
6 544 silver minerals (Fig. 6A-D). Significantly, the canfieldite has an unusually high Se content (up to 11.6  
7  
8 545 wt.%; Zhai et al., 2019c), which is zonally distributed such that the highest concentration is in the cores  
9  
10 546 of crystals (Fig. 7D). Another unusual feature of the mineralogy is the occurrence of cassiterite (Fig. 7A,  
11  
12 547 E; see also Jiang et al., 2018), which was replaced by canfieldite, argentite, galena and sphalerite (Fig.  
13  
14 548 7A). The element suite of the ore minerals of the Shuangjianzishan deposit therefore differs from that  
15  
16 549 of the Ag-Pb-Zn veins associated with porphyry deposits in the North and South American Cordillera  
17  
18 550 (e.g., Peru), which does not include significant Sn or Se (Bendezú and Fontboté, 2009).

19  
20  
21 551 We interpret the enrichment of Sn and Se in the Shuangjianzishan deposit to be of magmatic origin  
22  
23 552 (as we do for the other ore elements; see below). In support of this interpretation, we note that Sn- and  
24  
25 553 Se-bearing ore minerals also have been reported from several Ag-Au-Cu-Se-Te epithermal deposits that  
26  
27 554 are spatially associated with porphyry deposits (e.g., the Prasolovskoye deposit, Kuril Islands, So et  
28  
29 555 al., 1995; the Kawazu deposit, Japan, Shimizu et al., 2008; the Svetloye deposit, Russia, Alderton and  
30  
31 556 Brameld, 2006; and the Mavrokoryfi prospect, Greece, Voudouris, 2011). It is also noteworthy that Se  
32  
33 557 has been observed in the structure of molybdenite in intrusion-related deposits in Bohemia (Pasava et  
34  
35 558 al., 2016), indicating a magmatic origin for the Se in these deposits. Finally, we note that a number of  
36  
37 559 magmatic-hydrothermal ore deposits located relatively close to the Shuangjianzishan deposit, for  
38  
39 560 example, the Bianjiadayuan Ag-Pb-Zn deposit, the Weilasituo Cu-Zn deposit, the Huanggangliang Fe-(Sn)  
40  
41 561 deposit, the Dajing Cu-Sn deposit, the Baiyinnuoer Pb-Zn deposit, the Haobugao Fe-Zn deposit, and the  
42  
43 562 Anle Cu-Sn deposit (Fig. 1C), are spatially associated with Sn-rich granitic intrusions/porphyries and may  
44  
45 563 be genetically related to them (Ouyang et al., 2015; Zhu et al., 2016; Zeng et al., 2016; Zhai et al., 2017).

46  
47  
48 564 **Sulfur and metal sources**

49  
50 565 The sulfides and sulfosalts from the Ag-Pb-Zn mineralized veins at Shuangjianzishan have a narrow  
51  
52 566 range of  $\delta^{34}\text{S}$  values (i.e., -4.67 to +2.44‰) and an average value that is close to zero (Fig. 9A). Moreover,  
53  
54 567 these values are independent of the mineral paragenesis (Fig. 9A) and the depth from which the  
55  
56 568 samples were taken (Fig. 9B; Table 2). The corresponding range and mean  $\delta^{34}\text{S}_{\text{H}_2\text{S}}$  values are -3.32 to  
57  
58 569 +0.77‰ and  $-1.65 \pm 0.83\%$ , respectively, assuming a temperature of 250 °C. These observations suggest  
59  
60 570 a magmatic source for the sulfur (Seal, 2006). The  $\delta^{34}\text{S}$  values reported here are also very similar to

1 571 those of sulfides in nearby magmatic-hydrothermal ore deposits (e.g., the Bianjiadayuan Ag-Pb-Zn,  
2 572 Weilasituo Zn-Cu-Ag, Baiyinnuoer Pb-Zn, Hashitu Mo, Haobugao Fe-Zn, and Huanggangliang Fe-Sn  
3  
4 573 deposits), which are generally in the range  $-4$  to  $+4\%$  (Yao et al., 2012; Ouyang et al., 2014; Zhai et al.,  
5  
6 574 2014b, 2018b, 2019a, and references therein). This suggests strongly that most of the ore deposits in  
7  
8 575 the southern GHR had a similar source of sulfur, namely a magma. Finally, we note that the relatively  
9  
10 576 small range in the  $\delta^{34}\text{S}$  values of the Shuangjianzishan ores, the even smaller range for individual  
11  
12 577 minerals (Fig. 9) and the very small intra-crystal variation of these values indicate that pH and  
13  
14 578 particularly  $f\text{O}_2$  did not vary significantly during ore formation (see Ohmoto, 1972; Wood, 1998; King et  
15  
16 579 al., 2014).

18  
19 580 In order to evaluate the source of the metals, we compared the lead isotope compositions of the  
20  
21 581 sulfides and Ag-bearing sulfosalts from Shuangjianzishan with corresponding data for Mesozoic granite,  
22  
23 582 andesite and basalt, Paleozoic granite, and Permian slate, as well as Pb isotope data for sulfides from  
24  
25 583 numerous nearby magmatic-hydrothermal ore deposits (Electronic Appendix Table A3; Zhang et al.,  
26  
27 584 1995, 2008; Shen and Fu, 1999; Chu et al., 2001; Cai et al., 2004; Wang, 2009; Zeng et al., 2009; Guo et  
28  
29 585 al., 2010; Jiang et al., 2010; Shao et al., 2010; Yao et al., 2012; Wu et al., 2012; Zhai et al., 2014b, 2018b,  
30  
31 586 2019a). The  $^{206}\text{Pb}/^{204}\text{Pb}$ ,  $^{207}\text{Pb}/^{204}\text{Pb}$ , and  $^{208}\text{Pb}/^{204}\text{Pb}$  ratios for the Shuangjianzishan ore minerals are  
32  
33 587 very similar to those of magmatic-hydrothermal ore deposits in the region (Fig. 13A, B), suggesting  
34  
35 588 strongly that the Shuangjianzishan ores and these deposits shared a common source for their metals. It  
36  
37 589 should be noted, however, that the ranges for our ratios, which were obtained by in situ analysis, are  
38  
39 590 significantly smaller than for the other deposits. We attribute this to the fact that the latter data were  
40  
41 591 obtained from mineral separates. The ranges for our Pb isotope ratios are also narrower than those for  
42  
43 592 the Shuangjianzishan deposit reported by Wang, F. (2017) from mineral separates; the latter ratios also  
44  
45 593 indicate more radiogenic Pb isotope compositions (Electronic Appendix Fig. A5). We consider it likely  
46  
47 594 that this difference is due to contamination of the separates by minerals with radiogenic Pb (e.g., sericite  
48  
49 595 and K-feldspar).

51  
52 596 The Pb isotopic ratios of the Shuangjianzishan ore minerals closely match those of the local Mesozoic  
53  
54 597 (late Jurassic to early Cretaceous) granites (Fig. 13A, B). This suggests that the Pb and other metals (e.g.,  
55  
56 598 Ag and Zn) originated mainly from Mesozoic magmas (e.g., the Mo-mineralized porphyry). In contrast,  
57  
58 599 the substantial differences between the Pb isotopic ratios of the Shuangjianzishan ore minerals and  
59  
60 600 those of the other rock units in the district, for example, the Mesozoic basalt, andesite, the Paleozoic

1 601 granite and the Permian slate (Fig. 13A, B), demonstrate that these rock units did not contribute to the  
2 602 ore metal budget.

### 3 603 **pH and $fO_2$ conditions**

4 604 The pH- $\log fO_2$  conditions of ore formation and alteration were evaluated from phase equilibria  
5 605 calculated using the HCh software package (Shvarov, 2011). Stability relationships among the minerals  
6 606 were determined assuming that the minerals are all ideal solid solutions. The total sulfur activity ( $\Sigma aS$ )  
7 607 was conservatively assumed to be 0.01 (e.g., Bonsall et al., 2011; Williams-Jones and Migdisov, 2014),  
8 608 the  $\delta^{34}S_{\Sigma S}$  was assumed to be +0.5‰ (i.e., the isotopic composition of magmatic sulfur species), and the  
9 609 total dissolved  $CO_2$  ( $\Sigma C$ ) was assumed to be 1 m (e.g., Ohmoto, 1972). The temperatures evaluated were  
10 610 250° and 200°C (see earlier discussion of the temperature of ore formation).

11 611 The pH of base metal sulfide and Ag-sulfosalt deposition at 250°C varied from 5.6 to 6.7 (pure water  
12 612 at this temperature has a pH value of 5.6) (Fig. 14A), based on the observation that this mineralization  
13 613 was associated with sericitization (Fig. 6A, I) and the occurrence of calcite as a gangue mineral (Fig. 4C).  
14 614 The presence of calcite also restricts  $\log fO_2$  to values above -43.1 and that of pyrite to values below -  
15 615 32.5 (Fig. 14A). The measured  $\delta^{34}S$  values calculated to have been in equilibrium with the fluid for  
16 616 different sets of pH and  $\log fO_2$  conditions ( $\delta^{34}S = -4.67$  to +2.44‰; Fig. 9A) further restricts  $\log fO_2$  to  
17 617 values below -36.8 (Fig. 14A). These values correspond to  $\Delta \log fO_2$  (HM) values (hematite/magnetite  
18 618 buffer) of -8.7 to -2.4. At 200°C, the pH of base metal sulfide and Ag-sulfosalt deposition would have  
19 619 been 5.3 to 6.8 (the pH value of pure water at this temperature is 5.6) and the  $\Delta \log fO_2$  (HM) values  
20 620 would have been -8.5 to -2.2 (Fig. 14B). Thus, the  $fO_2$  conditions of Ag-Pb-Zn ore deposition varied from  
21 621 moderately to strongly reducing; the pH was nearly neutral to weakly alkaline.

### 22 622 **Timing of Ag-Pb-Zn mineralization**

23 623 The age of vein-type Ag-Pb-Zn mineralization in the GHR is still poorly constrained, whereas that of  
24 624 spatially-associated porphyry Mo-Cu and skarn Fe-Sn deposits is well-known from numerous  
25 625 molybdenite Re-Os dates. Although there have been many determinations of the age of Ag-Pb-Zn  
26 626 mineralization in the Shuangjianzishan deposit, there is no agreement on this age. For example, Cui  
27 627 (2015) proposed an age of  $249.1 \pm 1.9$  Ma for the deposit based on a zircon U-Pb age for one of the  
28 628 diorite dikes. As discussed earlier, however, these dikes predate the mineralization (Figs. 2A and 3B).  
29 629 Ouyang et al. (2016) proposed an age of  $159.3 \pm 2.3$  Ma based on a zircon U-Pb date for a granite  
30 630 porphyry that they considered was related to the mineralization, whereas Gu et al. (2017), using the

1 631 same method applied to the porphyry, concluded that the mineralization developed at  $133.4 \pm 1.2$  Ma.  
2 632 Wu et al. (2013) was the first to date the mineralization and obtained an age of  $132.7 \pm 3.9$  Ma from a  
3 633 sphalerite Rb-Sr isochron. However, this Rb-Sr age was likely not the age of the sphalerite but rather the  
4 634 age of inclusions of a mineral such as muscovite that would have hosted the Rb and Sr. Wang et al. (2016)  
5 635 dated the mineralization indirectly by determining the age of sericite using the Ar-Ar method and  
6 636 obtained an age of  $146.9 \pm 1.9$  Ma, but they did not establish the spatial and temporal relationships  
7 637 between the sericite and the mineralization. They also reported a Re-Os age of  $162.6 \pm 2.6$  Ma for  
8 638 molybdenite from the nearby granite porphyry described earlier in this paper. More recently, Wang, F.  
9 639 (2017) obtained an age of  $159 \pm 6$  Ma for the Ag-Pb-Zn mineralization using the Re-Os method applied  
10 640 to arsenopyrite and pyrite, and a U-Pb age of  $148 \pm 1$  Ma for hydrothermal zircon.

11 641 As described earlier, we conducted a comprehensive geochronological program designed to reliably  
12 642 establish the age of the mineralization. The results of our determinations of the ages of the different  
13 643 lithological units in the Shuangjianshan district are illustrated in Figure 15A. A diorite dike that is  
14 644 crosscut by the Ag-Pb-Zn veins and is pre-ore (Fig. 15B) yielded a zircon U-Pb age of  $250.2 \pm 2.0$  Ma (Fig.  
15 645 11A). Dacite located in the southwestern part of the district (Fig. 2A), which is cut by several Ag-Pb-  
16 646 Zn mineralized veins (Figs. 2A and 3B) and thus is also pre-ore, was dated at  $133.9 \pm 1.4$  Ma (zircon  
17 647 U-Pb method,  $N = 22$ ,  $MSWD = 0.43$ ; Fig. 11B). Within the analytical uncertainty, the same age,  $134.4$   
18 648  $\pm 1.0$  Ma (Fig. 11D, E), was obtained for a Mo-mineralized granite porphyry located only 800 m from  
19 649 the deposit using the zircon U-Pb method, suggesting that the dacite and porphyry may have been  
20 650 derived from the same magma (Fig. 15C). Their similar trace element compositions also support this  
21 651 hypothesis (Electronic Appendix Fig. A3). Moreover, Re-Os dating of molybdenite related to the  
22 652 porphyry yielded a weighted mean age of  $134.9 \pm 3.4$  Ma ( $MSWD = 9$ ), which is indistinguishable  
23 653 within error from the age of the porphyry. Finally, a granite intrusion in the northern part of the  
24 654 mining district ( $\sim 2$  km from the deposit) yielded a mean  $^{206}\text{Pb}/^{238}\text{U}$  age of  $135.2 \pm 1.4$  Ma, which is  
25 655 indistinguishable within the uncertainty from the  $133.7 \pm 0.6$  Ma age reported by Wu (2014) for the  
26 656 same intrusion.

27 657 We dated the Ag-Pb-Zn mineralization directly using the Re-Os model ages for the pyrite samples  
28 658 from the Ag-Pb-Zn mineralized veins (Fig. 3B). This yielded a weighted mean age of  $135.0 \pm 0.6$  Ma  
29 659 that is in agreement with the sphalerite Rb-Sr isochron age of  $132.7 \pm 3.9$  Ma reported by Wu et al.  
30 660 (2013). These ages, within the error, are the same as the ages reported for the granite porphyry and its

1 661 molybdenite mineralization (Fig. 15D). Based on these age determinations, we conclude that the Ag-  
2 662 Pb-Zn mineralization of the Shuangjianzishan deposit was the product of hydrothermal fluids released  
3  
4 663 during an early Cretaceous felsic magmatic event at ~134 Ma (Fig. 15A). This event produced volcanic  
5  
6 664 rocks (i.e., dacite) and granitic intrusions (Fig. 15C, D), including the nearby Mo-mineralized porphyry,  
7  
8 665 which we speculate is genetically related to the Ag-Pb-Zn mineralization.  
9

10 666 The age interpreted for the Shuangjianzishan deposit is similar to that for many other magmatic-  
11  
12 667 hydrothermal ore deposits in the southern GHR (Fig. 1C). These include the Baiyinnuoer skarn Pb-Zn  
13  
14 668 deposit (135 ± 1 Ma, molybdenite Re-Os; Ouyang et al., 2015), the Huanggangliang skarn Fe-(Sn)  
15  
16 669 deposit (135 ± 2 Ma, molybdenite Re-Os; Zhai et al., 2014b), the Weilasituo greisen Sn and Cu-Zn vein  
17  
18 670 deposit (136 ± 1 Ma, zircon U-Pb; Zhai et al., 2016), the Bairendaba Ag-Pb-Zn vein deposit (135 ± 3  
19  
20 671 Ma, sericite Ar-Ar; Chang and Lai, 2010), the Anle Sn-(Cu) vein deposit (133 ± 3 Ma, sericite Ar-Ar;  
21  
22 672 Wang et al., 2001), and the Dajing Cu-(Sn) vein deposit (133 ± 1 Ma, zircon U-Pb/sericite Ar-Ar;  
23  
24 673 Ishiyama et al., 2008; Jiang et al., 2012). Shuangjianzishan is thus a representative of an important late  
25  
26 674 Mesozoic (early Cretaceous) metallogenic event in the southern GHR that involved felsic  
27  
28 675 magmatism (Mao et al., 2005, 2014; Wu et al., 2011; Ouyang et al., 2015; Zhai et al., 2015; Shu et al.,  
29  
30 676 2016; Chen, Y., et al., 2017).

### 31 677 **Tectonic controls on Ag-Pb-Zn mineralization**

32  
33  
34 678 The regional magmatism in the early Cretaceous is represented by both I-type (granodiorite,  
35  
36 679 monzogranite and syenite) and A-type granitoids (Wu et al., 2002); the latter are interpreted to have  
37  
38 680 formed from magmas derived from the lower crust (Wei et al., 2008). These granitoids display an  
39  
40 681 eastward-younging trend, which indicates their emplacement in an extensional setting (Zhang et al.,  
41  
42 682 2010; Wu et al., 2011). The granite porphyry in the Shuangjianzishan district has a geochemical  
43  
44 683 signature characteristic of an arc-related magma (i.e., Y >30 ppm and Sr/Y ratios <10; Electronic  
45  
46 684 Appendix Fig. A6A), but nonetheless one that is distinguishable from the adakites, which are commonly  
47  
48 685 associated with porphyry Cu±Mo±Au deposits (Sun et al., 2011; Richards, 2011; Chiaradia et al., 2012).  
49  
50 686 However, it also has characteristics typical of A-type granites forming in extensional tectonic settings  
51  
52 687 (Electronic Appendix Fig. A6B). This setting for the GHR in the early Cretaceous is manifested by the  
53  
54 688 development of extensional basins (e.g., the Songliao, Erlian, and Hailaer basins; Meng, 2003),  
55  
56 689 formation of metamorphic core complexes (Wang et al., 2012), widespread alkali plutonism and  
57  
58 690 volcanism (A-type granites and bimodal volcanic rocks; Wu et al., 2002; Wang et al., 2006; Zhang et al.,  
59  
60  
61  
62  
63  
64  
65

1 691 2010), and formation of Climax-type porphyry molybdenum deposits (e.g., the Hashitu, Haisugou,  
2 692 Banlashan, and Aolunhua deposits; Zhai et al., 2018b) and alkaline intrusion-related rare metal deposits  
3  
4 693 (e.g., the Baerzhe Zr, REE and Nb deposit; Ouyang et al., 2015). It has been proposed that Paleo-Pacific  
5  
6 694 subduction in the early Cretaceous caused lithospheric delamination, slab rollback and crustal extension  
7  
8 695 of the back-arc domain (Zhang et al., 2010; Wu et al., 2011, and references therein). The slab rollback  
9  
10 696 could have triggered large scale upwelling of the asthenosphere and back-arc spreading along the entire  
11  
12 697 margin of NE China, softening the lithosphere, thereby facilitating the lithospheric thinning and  
13  
14 698 extension observed across the East Asian continental margin for the early Cretaceous (~140-110 Ma;  
15  
16 699 Zhang et al., 2011). This, in turn, could have led to the emplacement of the large numbers of Cretaceous  
17  
18 700 granitoids in NE China (Zhang et al., 2008; Wu et al., 2011; Wilde, 2015). In summary, we propose that  
19  
20 701 the widespread synchronous Ag-Pb-Zn mineralization observed in the GHR, including the  
21  
22 702 Shuangjianzishan deposit, was a direct consequence of Paleo-Pacific subduction and subsequent slab  
23  
24 703 rollback, lithospheric delamination, thinning and extension that triggered the emplacement of large  
25  
26 704 volumes of granitic magma during the early Cretaceous.

#### 27 28 29 705 **A Proposed Genetic Model**

30  
31 706 The data presented in this paper provide strong evidence that the Ag-Pb-Zn veins of the  
32  
33 707 Shuangjianzishan deposit were the product of a magmatic-hydrothermal system related to a nearby  
34  
35 708 early Cretaceous Mo-mineralized granite porphyry. These data show, moreover, that the mineralization  
36  
37 709 was coeval with the intrusion of this porphyry. In Figure 15, we present a model that explains the genesis  
38  
39 710 of the Shuangjianzishan Ag-Pb-Zn deposit using the geological observations and geochemical data  
40  
41 711 presented earlier. In this model, both the ore-forming fluid and metals (i.e., Ag, Pb, and Zn) were sourced  
42  
43 712 from the adjacent porphyry intrusion, which has an arc affinity (Electronic Appendix Fig. A6) and was  
44  
45 713 emplaced in the early Cretaceous (Fig. 15A) in response to regional slab rollback and lithospheric  
46  
47 714 delamination and thinning. The porphyry was intruded in two phases (early coarse-grained and late  
48  
49 715 fine-grained phases), the second of which exsolved a magmatic-hydrothermal fluid. The metals and  
50  
51 716 sulfur were transported to well beyond the confines of the intrusion (~ 800 m away) by this fluid, where  
52  
53 717 they were deposited in pre-existing faults or fractures created by the withdrawal of magma during the  
54  
55 718 waning stages of the magmatic-hydrothermal system (Fig. 15D).

56  
57  
58 719 The Shuangjianzishan ore district is similar in many aspects to Cordilleran ore districts, in which  
59  
60 720 porphyry deposits are associated with distal Ag-Pb-Zn deposits (Fontboté and Bendejú, 2009;

1 721 Baumgartner et al., 2009), but there are also significant differences. The similarities include: ore (sulfide  
2 722 and a variety of Ag-bearing sulfosalts) and gangue (quartz and calcite) mineral assemblages; the ore  
3 723 paragenesis (base metal sulfides prior to Ag-bearing sulfosalts/sulfides); alteration zonation; high Ag/Au  
4 724 ratios; open space filling and epigenetic veins structurally controlled by faults; formation under  
5 725 epithermal conditions at shallow levels (<1 km) from low temperature (~200° to 250°C) and salinity (~1  
6 726 to 10 wt.% NaCl equivalent) fluids; a magmatic source for the fluids and metal; and a close genetic  
7 727 association with porphyry systems (Baumgartner et al., 2009; Fontboté and BendeZú, 2009; Catchpole  
8 728 et al., 2015; Rottier et al., 2016, 2018a). An important difference is that the Cordilleran veins are  
9 729 commonly characterized by a Cu-Zn-Pb-(Ag-Au-Bi) metal suite (Fontboté and BendeZú, 2009), whereas  
10 730 the Shuangjianzishan deposit, as well as other Ag-Pb-Zn veins in the GHR, have a Ag-Pb-Zn-(Sn-Se-Sb)  
11 731 metal suite (Fig. 5); the Shuangjianzishan deposit is distinguished by rare Ag-bearing sulfosalts (i.e.,  
12 732 canfieldite, Figs. 6A-D, 7), whereas the sulfosalts in the Cordilleran veins are dominantly Bi-bearing (e.g.,  
13 733 cuprobismutite; Baumgartner et al., 2008). Moreover, a well-developed spatial zonation of ore and  
14 734 alteration minerals has been identified in many of the Cordilleran veins (Catchpole et al., 2015),  
15 735 whereas this is not observed in the Shuangjianzishan deposit and other Ag-Pb-Zn deposits in the GHR  
16 736 (Zhai et al., 2019a). Another significant difference is that the distal Ag-rich Peruvian deposits are hosted  
17 737 by carbonates (Fontboté and BendeZú, 2009), whereas the Shuangjianzishan deposit is hosted by slates  
18 738 (Fig. 2). The Cordilleran veins commonly formed in the shallow parts of porphyry Cu systems, in which  
19 739 both epithermal and porphyry-type mineralization are important (Baumgartner et al., 2008; BendeZú  
20 740 and Fontboté, 2009), whereas, although a close genetic relationship between the Shuangjianzishan Ag-  
21 741 Pb-Zn veins and a porphyry system has been established, the porphyry-type mineralization is very  
22 742 limited and other similar vein-type Ag-Pb-Zn deposits in the GHR are not associated with known  
23 743 porphyry-type mineralization. Finally, the GHR polymetallic vein deposits are related to post-subduction  
24 744 back-arc porphyry Mo systems, whereas the Cordilleran veins are commonly associated with  
25 745 subduction-related porphyry Cu systems (Fontboté and BendeZú, 2009; Catchpole et al., 2015). In  
26 746 conclusion, the model proposed for the giant Shuangjianzishan deposit emphasizes a genetic  
27 747 relationship between minor proximal Mo mineralization and considerable distal epithermal Ag-Pb-Zn  
28 748 mineralization. We expect that recognition of this relationship will provide an important guide for  
29 749 regional Ag-Pb-Zn exploration in NE China and elsewhere.

30 750

1  
2  
3  
4  
5  
6  
7  
8  
9  
10  
11  
12  
13  
14  
15  
16  
17  
18  
19  
20  
21  
22  
23  
24  
25  
26  
27  
28  
29  
30  
31  
32  
33  
34  
35  
36  
37  
38  
39  
40  
41  
42  
43  
44  
45  
46  
47  
48  
49  
50  
51  
52  
53  
54  
55  
56  
57  
58  
59  
60  
61  
62  
63  
64  
65

751 **Acknowledgements**

752 This research was supported financially by the National Natural Science Foundation of China (Grant  
753 41672068), the Fundamental Research Funds for the Central Universities (Grants 2652015045,  
754 2652018129 and QZ05201904), the MOST Special Fund from the State Key Laboratory of Geological  
755 Processes and Mineral Resources, China University of Geosciences (Grant MSFGPMR201804) and the  
756 Chinese “111” project (Grant B07011). We thank Li Su, Hongyu Zhang and Peng Xiang (CUGB) for  
757 performing the U-Pb analyses, Dongjie Tang (CUGB) for assistance with the SEM, and Zhenyu Chen and  
758 Xiaodan Chen (CAGS) for help with the microprobe analyses. Hegen Ouyang provided valuable insights  
759 into the ore deposit geology, and Xiaowen Huang helped with the interpretation of the Re-Os data.  
760 Meng Dai and Wenbin Jia assisted with the field work and sample collection. Preparation and writing of  
761 this manuscript was completed during DZ’s visit to McGill University. Travel to and living expenses in  
762 Canada were supported financially by an international visiting program grant from the Fundamental  
763 Research Funds for the Central Universities, China. DS acknowledges the Total Endowment Fund and  
764 the CUG (Wuhan) scholarship. We thank Economic Geology reviewers Bertrand Rottier and Ryan Taylor,  
765 Associate Editor David John and Editor-in-Chief Larry Meinert for their insightful reviews, which helped  
766 improve this paper.

767  
768 **References**

769 Alderton, D.H.M., and Brameld, F.C., 2006, Telluride mineralization at the Svetloye gold prospect,  
770 Khabarovsk Krai, eastern Russia. In: Cook NG, Özgenc I, Oyman T (eds) Au-Ag-Te-Se deposits, IGCP 486  
771 field workshop, Izmir 24-29 September 2006, Proceedings, p. 1-5.  
772 Balabin, A.I., and Sack, R.O., 2000, Thermodynamics of (Zn, Fe)S sphalerite: a CVM approach with large  
773 basis clusters: Mineralogical Magazine, v. 64, p. 923-943.  
774 Baumgartner, R., Fontboté, L., and Vennemann, T., 2008, Mineral zoning and geochemistry of  
775 epithermal polymetallic Zn-Pb-Ag-Cu-Bi mineralization at Cerro de Pasco, Peru: Economic Geology, v.  
776 103, p. 493-537.  
777 Baumgartner, R., Fontboté, L., Spikings, R., Ovtcharova, M., Schaltegger, U., Schneider, J., Page, L., and  
778 Gutjahr, M., 2009, Bracketing the age of magmatic-hydrothermal activity at the Cerro de Pasco  
779 epithermal polymetallic deposit, central Peru: A U-Pb and <sup>40</sup>Ar/<sup>39</sup>Ar study: Economic Geology, v. 104, p.  
780 479-504.

1 781 Beaudoin, G., and Sangster, D.F., 1992, A descriptive model for silver-lead-zinc veins in clastic  
2 782 metasedimentary terranes: *Economic Geology*, v. 87, p. 1005-1021.  
3  
4 783 Bendezú, R., and Fontboté, L., 2002, Late timing for high sulfidation Cordilleran base metal lode and  
5 784 replacement deposits in porphyry-related districts: the case of Colquijirca, central Peru: *SGA News*, v.  
6 785 13, p. 1-9.  
7  
8 786 Bendezú, R., and Fontboté, L., 2009, Cordilleran epithermal Cu-Zn-Pb-(Au-Ag) mineralization in the  
9 787 Colquijirca district, central Peru: Deposit-scale mineralogical patterns: *Economic Geology*, v. 104, p. 905-  
10 788 944.  
11  
12 789 Black, L.P., Kamo, S.L., Allen, C.M., Aleinikoff, J.N., Davis, D.W., Korsch, R.J., and Foudoulis, C., 2003,  
13 790 TEMORA 1: a new zircon standard for Phanerozoic U-Pb geochronology: *Chemical Geology*, v. 200, p.  
14 791 155-170.  
15  
16 792 Bonsall, T.A., Spry, P.G., Voudouris, P.C., Tombros, S., Seymour, K.S., and Melfos, V., 2011, The  
17 793 geochemistry of carbonate-replacement Pb-Zn-Ag mineralization in the Lavrion district, Attica, Greece:  
18 794 Fluid inclusion, stable isotope, and rare earth element studies: *Economic Geology*, v. 106, p. 619-651.  
19  
20 795 Cai, J.H., Yan, G.H., Xiao, C.D., Wang, G.Y., Mu, B.L., and Zhang, R.H., 2004, Nd, Sr, Pb isotopic  
21 796 characteristics of the Mesozoic intrusive rocks in the Taihang Da Hinggan Mountains Tectonomagmatic  
22 797 Belt and their source region: *Acta Petrologica Sinica*, v. 20, p. 1225-1242 (in Chinese with English  
23 798 abstract).  
24  
25 799 Catchpole, H., Kouzmanov, K., Putlitz, B., Seo, J.H., and Fontboté, L., 2015, Zoned base metal  
26 800 mineralization in a porphyry system: Origin and evolution of mineralizing fluids in the Morococha district,  
27 801 Peru: *Economic Geology*, v. 110, p. 39-71.  
28  
29 802 Chang, Y., and Lai, Y., 2010, Study of characteristics of ore-forming fluid and chronology in the Yindu Ag-  
30 803 Pb-Zn polymetallic ore deposit, Inner Mongolia: *Acta Scientiarum Naturalium Universitatis Pekinensis*,  
31 804 v. 46, p. 581-593 (in Chinese with English abstract).  
32  
33 805 Chen, L., Chen, K., Bao, Z., Liang, P., Sun, T., and Yuan, H., 2017, Preparation of standards for in situ sulfur  
34 806 isotope measurement in sulfides using femtosecond laser ablation MC-ICP-MS: *Journal of Analytical*  
35 807 *Atomic Spectrometry*, v. 32, p. 107-116.  
36  
37 808 Chen, Y.J., Zhang, C., Wang, P., Pirajno, F., and Li, N., 2017, The Mo deposits of Northeast China: a  
38 809 powerful indicator of tectonic settings and associated evolutionary trends: *Ore Geology Reviews*, v. 81,  
39 810 p. 602-640.  
40  
41  
42  
43  
44  
45  
46  
47  
48  
49  
50  
51  
52  
53  
54  
55  
56  
57  
58  
59  
60  
61  
62  
63  
64  
65

- 1 811 Chiaradia, M., 2014, Copper enrichment in arc magmas controlled by overriding plate thickness: Nature  
2 Geoscience, v. 7, p. 43.  
3  
4 813 Chiaradia, M., Ulianov, A., Kouzmanov, K., and Beate, B., 2012, Why large porphyry Cu deposits like high  
5 Sr/Y magmas?: Scientific reports, v. 2, p. 685.  
6  
7 814  
8  
9 815 Chu, X.L., Huo, W.G., and Zhang, X., 2001, Sulfur, carbon and lead isotope studies of the Dajing  
10 polymetallic deposit in Linxi county, Inner Mongolia, China – Implication for metallogenic elements  
11 from hypomagmatic source: Resource Geology, v. 51, p. 333-344.  
12  
13 817  
14  
15 818 Craddock, P.R., Rouxel, O.J., Ball, L.A., and Bach, W., 2008, Sulfur isotope measurement of sulfate and  
16 sulfide by high-resolution MC-ICP-MS: Chemical Geology, v. 253, p. 102-113.  
17  
18 819  
19 820 Cui, M., 2015, The geochemical characteristics and diagenesis of ore-forming diorite-porphyrite from  
20 Shuangjianzishan Ag polymetallic deposit in Inner Mongolia: Master thesis, China University of  
21 Geosciences Beijing, Beijing, China, 55 p. (in Chinese with English abstract).  
22  
23 822  
24  
25 823 Defant, M.J., and Drummond, M.S., 1993, Mount St. Helens: potential example of the partial melting of  
26 the subducted lithosphere in a volcanic arc: Geology, v. 21, p. 547-550.  
27  
28 824  
29 825 Duan, X.X., Zeng, Q.D., Yang, Y.H., Liu, J.M., Chu, S.X., Sun, Y., and Zhang, Z.L., 2015, Triassic magmatism  
30 and Mo mineralization in Northeast China: geochronological and isotopic constraints from the Laojiagou  
31 porphyry Mo deposit: International Geology Review, v. 57, p. 55-75.  
32  
33 827  
34  
35 828 Einaudi, M.T., 1981, Skarns associated with porphyry plutons: Description of deposits, southwestern  
36 North America. II. General features and origin. Advances in Geology of the Porphyry Copper Deposits of  
37 Southwestern North America. University of Arizona Press, Tucson, p. 139-183.  
38  
39 830  
40  
41 831 Einaudi, M.T., Hedenquist, J.W., and Inan, E.E., 2003, Sulfidation state of fluids in active and extinct  
42 hydrothermal systems: transitions from porphyry to epithermal environments: Special Publication-  
43 Society of Economic Geologists, v. 10, p. 285-314  
44  
45 833  
46  
47 834 Fontboté, L., and Bendezú, R., 2009, Cordilleran or Butte-type veins and replacement bodies as a deposit  
48 class in porphyry systems. In: Williams et al., P.J. (ed) Proceedings of the 10th Biennial Society of Geology  
49 Applied to Ore Deposits Meeting, Townsville, Australia, p. 521-523.  
50  
51 835  
52  
53 837 Gao, J., Klemd, R., Zhu, M., Wang, X., Li, J., Wan, B., Xiao, W., Zeng, Q., Shen, P., Sun, J., and Qin, K., 2018,  
54 Large-scale porphyry-type mineralization in the Central Asian metallogenic domain: A review: Journal  
55 of Asian Earth Sciences, v. 165, p. 7-36.  
56  
57 839  
58  
59 840 Gu, Y.C., Chen, R.Y., Jia, B., and Ju, N., 2017, Zircon U-Pb dating and geochemistry of the granite porphyry

1 841 from the Shuangjianzishan silver polymetallic deposit in Inner Mongolia and tectonic implications:  
2 842 Geology and Exploration, v. 53, p. 495-507 (in Chinese with English abstract).  
3  
4 843 Guilbert, J.M., and Park, C.F., 1986, The geology of ore deposits, 4th ed.: New York, WH Freeman, 985  
5  
6 844 p.  
7  
8 845 Guo, F., Fan, W., Gao, X., Li, C., Miao, L., Zhao, L., and Li, H., 2010, Sr–Nd–Pb isotope mapping of  
9  
10 846 Mesozoic igneous rocks in NE China: constraints on tectonic framework and Phanerozoic crustal  
11  
12 847 growth: Lithos, v. 120, p. 563-578.  
13  
14 848 HBGMR (Heilongjiang Bureau of Geology and Mineral Resources), 1993, Regional Geology of  
15  
16 849 Heilongjiang Province. Geological Publishing House, Beijing, pp. 347–418 (in Chinese with English  
17  
18 850 abstract).  
19  
20  
21 851 Heinrich, C.A., 2005, The physical and chemical evolution of low-salinity magmatic fluids at the porphyry  
22  
23 852 to epithermal transition: a thermodynamic study: Mineralium Deposita, v. 39, p. 864-889.  
24  
25 853 Irvine, T.N.J., and Baragar, W.R.A.F., 1971, A guide to the chemical classification of the common volcanic  
26  
27 854 rocks: Canadian Journal of Earth Sciences, v. 8, p. 523-548.  
28  
29 855 Ishiyama, D., Sato, R., Toshio, M., Yohei, I., and Wang, J.B., 2008, Characteristic features of tin-iron-  
30  
31 856 copper mineralization in the Anle-Huanggangliangmining area, InnerMongolia, China: Resource  
32  
33 857 Geology, v. 51, p. 377-392.  
34  
35 858 Jahn, B.M., 2004, The Central Asian Orogenic Belt and growth of the continental crust in the Phanerozoic.  
36  
37 859 In: Malpas, J., Fletcher, C.J.N., Ali, J.R., Aitchison, J.C. (Eds.), Aspects of the tectonic evolution of China:  
38  
39 860 Geological Society, London, Special Publications, v. 226, p. 73-100.  
40  
41 861 Jahn, B.M., Wu, F., and Chen, B., 2000, Granitoids of the Central Asian Orogenic Belt and continental  
42  
43 862 growth in the Phanerozoic: Geological Society of America Special Papers, v. 350, p. 181-193.  
44  
45 863 Jensen, E.P., and Barton, M.D., 2000, Gold deposits related to alkaline magmatism: Reviews in Economic  
46  
47 864 Geology, v. 13, p. 279-314.  
48  
49 865 Jiang, B., Wu, G., Chen, Y., Zhang, T., Liu, W., Zhang, T., and Li, X., 2018, Constraints on the genesis of the  
50  
51 866 Shuangjianzishan silver-polymetallic deposit, Balinzuo Qi, Inner Mongolia: evidence from trace and rare  
52  
53 867 earth elements: Acta Geologica Sinica, v. 92, p. 769-786 (in Chinese with English abstract).  
54  
55 868 Jiang, B.B., Zhu, X.Y., Huang, X.K., Xu, Q., and Zhang, Z.Q., 2017, Isotopic characteristics of sulfur and  
56  
57 869 lead metallogenic mechanism of Shuangjianzishan silver polymetallic deposit in Inner Mongolia:  
58  
59 870 Mineral Exploration, v. 8, p. 1010-1019 (in Chinese with English abstract).  
60  
61  
62  
63  
64  
65

1 871 Jiang, S.H., Chen, C.L., Bagas, L., Liu, Y., Han, N., Kang, H., and Wang, Z.H., 2017, Two mineralization  
2 872 events in the Baiyinnuoer Zn-Pb deposit in Inner Mongolia, China: Evidence from field observations, S-  
3  
4 873 Pb isotopic compositions and U-Pb zircon ages: *Journal of Asian Earth Sciences*, v. 144, p. 339-367.  
5  
6 874 Jiang, S.H., Liang, Q.L., Liu, Y.F., and Liu, Y., 2012, Zircon U–Pb ages of the magmatic rocks occurring in  
7  
8 875 and around the Dajing Cu–Ag–Sn polymetallic deposit of Inner Mongolia and constrains to the ore-  
9  
10 876 forming age: *Acta Petrologica Sinica*, v. 28, p. 495–513 (in Chinese with English abstract).  
11  
12 877 Jiang, S.H., Nie, F.J., Liu, Y.F., and Yun, F., 2010, Sulfur and lead isotopic compositions of Bairendaba and  
13  
14 878 Weilasituo silver-polymetallic deposits, Inner Mongolia: *Mineral Deposits*, v. 28, p. 101-112 (in Chinese  
15  
16 879 with English abstract).  
17  
18 880 Whalen, J.B., Currie, K.L., and Chappell, B.W., 1987, A-type granites: geochemical characteristics,  
19  
20 881 discrimination and petrogenesis: *Contributions to Mineralogy and Petrology*, v. 95, p. 407-419.  
21  
22 882 King, J., Williams-Jones, A.E., van Hinsberg, V., and Williams-Jones, G., 2014, High-sulfidation epithermal  
23  
24 883 pyrite-hosted Au (Ag-Cu) ore formation by condensed magmatic vapors on Sangihe Island,  
25  
26 884 Indonesia: *Economic Geology*, v. 109, p. 1705-1733.  
27  
28 885 Kissin, S.A., and Mango, H., 2014, *Silver Vein Deposits. Treatise on Geochemistry, Second Edition.*  
29  
30 886 Elsevier, Oxford, p. 425-432.  
31  
32 887 Kuang, Y.S., Zheng, G.R., Lu, M.J., Liu, Y.L., Zhang, S.J., Li, R.Y., and Cheng, W.J., 2014, Basic characteristics  
33  
34 888 of Shuangjianzishan silver polymetallic dposit in Chifeng City, Inner Mongolia: *Mineral Deposits*, v. 33,  
35  
36 889 p. 847-856 (in Chinese with English abstract).  
37  
38 890 Li, J.Y., 2006, Permian geodynamic setting of Northeast China and adjacent regions: closure of the  
39  
40 891 Paleo-Asian Ocean and subduction of the Paleo-Pacific Plate: *Journal of Asian Earth Sciences*, v. 26, p.  
41  
42 892 207-224.  
43  
44 893 Li, Y., Selby, D., Condon, D., and Tapster, S., 2017, Cyclic magmatic-hydrothermal evolution in porphyry  
45  
46 894 systems: high-precision U-Pb and Re-Os geochronology constraints on the Tibetan Qulong porphyry Cu-  
47  
48 895 Mo deposit: *Economic Geology*, v. 112, p. 1419-1440.  
49  
50 896 Liu, C., Bagas, L., and Wang, F., 2016, Isotopic analysis of the super-large Shuangjianzishan Pb–Zn–Ag  
51  
52 897 deposit in Inner Mongolia, China: Constraints on magmatism, metallogenesis, and tectonic setting: *Ore*  
53  
54 898 *Geology Reviews*, v. 75, p. 252-267.  
55  
56 899 Liu, K., Zhang, J., Wilde, S. A., Zhou, J., Wang, M., Ge, M., Wang, J., and Ling, Y., 2017, Initial subduction  
57  
58 900 of the Paleo-Pacific Oceanic plate in NE China: Constraints from whole-rock geochemistry and zircon U-

1 901 Pb and Lu-Hf isotopes of the Khanka Lake granitoids: *Lithos*, v. 274-275, p. 254-270.  
2  
3 902 Liu, Y., Jiang, S., and Bagas, L., 2016, The genesis of metal zonation in the Weilasituo and Bairendaba  
4 903 Ag-Zn-Pb-Cu-(Sn-W) deposits in the shallow part of a porphyry Sn-W-Rb system, Inner Mongolia,  
5  
6 904 China: *Ore Geology Reviews*, v. 75, p. 150-173.  
7  
8 905 Ludwig, K.R., 2003, *User's Manual for Isoplot 3.0: a Geochronological Toolkit for Microsoft Excel*:  
9  
10 906 Berkeley Geochronology Centre, Special Publication.  
11  
12  
13 907 Maniar, P.D., and Piccoli, P.M., 1989, Tectonic discrimination of granitoids: *Geological Society of America*  
14  
15 908 *Bulletin*, v. 101, p. 635-643.  
16  
17 909 Mao, J., Pirajno, F., Lehmann, B., Luo, M., and Berzina, A., 2014, Distribution of porphyry deposits in the  
18  
19 910 Eurasian continent and their corresponding tectonic settings: *Journal of Asian Earth Sciences*, v. 79, p.  
20  
21 911 576-584.  
22  
23 912 Mao, J.W., Xie, G.Q., Zhang, Z.H., Li, X.F., Wang, Y.T., Zhang, C.Q., and Li, Y.F., 2005, Mesozoic large-scale  
24  
25 913 metallogenic pluses in North China and corresponding geodynamic settings: *Acta Petrologica Sinica*, v.  
26  
27 914 21, p. 169-188 (in Chinese with English abstract).  
28  
29 915 McDonough, W.F., and Sun, S.S., 1995, The composition of the Earth: *Chemical Geology*, v. 120, p. 223-  
30  
31 916 253.  
32  
33 917 Meng, Q.R., 2003, What drove late Mesozoic extension of the northern China-Mongolia tract?:  
34  
35 918 *Tectonophysics*, v. 369, p. 155-174.  
36  
37 919 Middlemost, E.A., 1994, Naming materials in the magma/igneous rock system: *Earth-Science Reviews*, v.  
38  
39 920 37, p. 215-224.  
40  
41 921 Ohmoto H., 1972, Systematics of sulfur and carbon isotopes in hydrothermal ore deposits: *Economic*  
42  
43 922 *Geology*, v. 67, p. 551-578.  
44  
45 923 Ouyang, H., Li, R., and Zhou, Z., 2016, The Jurassic mineralization of the Shuangjianzishan Ag-  
46  
47 924 polymetallic deposit and its significance in prospecting: evidence from geochronology: *Acta Geologica*  
48  
49 925 *Sinica*, v. 90, p. 1835-1845 (in Chinese with English abstract).  
50  
51 926 Ouyang, H., Mao, J., Santosh, M., Wu, Y., Hou, L., and Wang, X., 2014, The Early Cretaceous Weilasituo  
52  
53 927 Zn-Cu-Ag vein deposit in the southern Great Xing'an Range, northeast China: Fluid inclusions, H, O, S,  
54  
55 928 Pb isotope geochemistry and genetic implications: *Ore Geology Reviews*, v. 56, p. 503-515.  
56  
57 929 Ouyang, H., Mao, J., Zhou, Z., and Su, H., 2015, Late Mesozoic metallogeny and intracontinental  
58  
59 930 magmatism, southern Great Xing'an Range, northeastern China: *Gondwana Research*, v. 27, p. 1153-  
60  
61 931 1172.

- 1 932 Pašava, J., Svojtka, M., Veselovský, F., Ďurišová, J., Ackerman, L., Pour, O., Drábek, M., Halodová, P., and  
2  
3 933 Haluzová, E., 2016, Laser ablation ICPMS study of trace element chemistry in molybdenite coupled with  
4  
5 934 scanning electron microscopy (SEM)—an important tool for identification of different types of  
6  
7 935 mineralization: *Ore Geology Reviews*, v. 72, p. 874-895.  
8  
9 936 Pearce, J.A., Harris, N.B., and Tindle, A.G., 1984, Trace element discrimination diagrams for the tectonic  
10  
11 937 interpretation of granitic rocks: *Journal of Petrology*, v. 25, p. 956-983.  
12  
13 938 Qi, J.P., Chen, Y.J., and Pirajno, F., 2005, Geological characteristics and tectonic setting of the epithermal  
14  
15 939 deposits in the northeast China: *Journal of Mineralogy and Petrology*, v. 25, p. 47-59 (in Chinese with  
16  
17 940 English abstract).  
18  
19 941 Richards, J.P., 2011, High Sr/Y arc magmas and porphyry Cu±Mo±Au deposits: just add water: *Economic*  
20  
21 942 *Geology*, v. 106, p. 1075-1081.  
22  
23 943 Rickwood, P.C., 1989, Boundary lines within petrologic diagrams which use oxides of major and minor  
24  
25 944 elements: *Lithos*, v. 22, p. 247-263.  
26  
27 945 Rottier, B., Kouzmanov, K., Casanova, V., Bouvier, A.S., Baumgartner, L.P., Wälle, M., and Fontboté, L.,  
28  
29 946 2018a, Mineralized breccia clasts: a window into hidden porphyry-type mineralization underlying the  
30  
31 947 epithermal polymetallic deposit of Cerro de Pasco (Peru): *Mineralium Deposita*, v. 53, p. 919-946.  
32  
33 948 Rottier, B., Kouzmanov, K., Casanova, V., Wälle, M., and Fontboté, L., 2018b, Cyclic dilution of magmatic  
34  
35 949 metal-rich hypersaline fluids by magmatic low-salinity fluid: a major process generating the giant  
36  
37 950 epithermal polymetallic deposit of Cerro de Pasco, Peru: *Economic Geology*, v. 113, p. 825-856.  
38  
39 951 Rottier, B., Kouzmanov, K., Wälle, M., Bendezú, R., and Fontboté, L., 2016, Sulfide replacement  
40  
41 952 processes revealed by textural and LA-ICP-MS trace element analyses: example from the early  
42  
43 953 mineralization stages at Cerro de Pasco, Peru: *Economic Geology*, v. 111, p. 1347-1367.  
44  
45 954 Rusk, B.G., Reed, M.H., and Dilles, J.H., 2008, Fluid inclusion evidence for magmatic-hydrothermal fluid  
46  
47 955 evolution in the porphyry copper-molybdenum deposit at Butte, Montana: *Economic Geology*, v. 103,  
48  
49 956 p. 307-334.  
50  
51 957 Sack, R.O., 2005, Internally consistent database for sulfides and sulfosalts in the system Ag<sub>2</sub>S-Cu<sub>2</sub>S-ZnS-  
52  
53 958 FeS-Sb<sub>2</sub>S<sub>3</sub>-As<sub>2</sub>S<sub>3</sub>: Update: *Geochim Cosmochim Acta*, v. 69, p. 1157-1164.  
54  
55 959 Seal, R.R., 2006, Sulfur isotope geochemistry of sulfide minerals: *Reviews in Mineralogy and*  
56  
57 960 *Geochemistry*, v. 61, p. 633-677.  
58  
59 961 Seedorff, E., Dilles, J.H., Proffett, J.M., Einaudi, M.T., Zurcher, L., Stavast, W.J.A., Johnson, D.A., and

1 962 Barton, M.D., 2005, Porphyry deposits: Characteristics and origin of hypogene features: Economic  
2 Geology 100<sup>th</sup> Anniversary Volume, p. 251-298.  
3  
4 964 Selby, D., Creaser, R.A., Stein, H.J., Markey, R.J., and Hannah, J.L., 2007, Assessment of the <sup>187</sup>Re decay  
5 constant by cross calibration of Re–Os molybdenite and U–Pb zircon chronometers in magmatic ore  
6  
7 965 systems: *Geochimica et Cosmochimica Acta*, v. 71, p. 1999-2013.  
8  
9 966 Shao, J.A., Mu, B.L., Zhu, H.Z., and Zhang, L.Q., 2010, Material source and tectonic settings of the  
10 Mesozoic mineralization or the Da Hinggan Mts: *Acta Petrologica Sinica*, v. 26, p. 649-656 (in Chinese  
11 with English abstract).  
12  
13 968 Shen, J.F., and Fu, X.Z., 1999, The metallogenic environment and geology of copper polymetallic  
14 deposits in the Middle segment of Great Xing'an Range: Geological Publishing House, Beijing (in  
15 Chinese).  
16  
17 970 Shimizu, M., Shimizu, M., Furuhashi, T., Harada, A., and Cook, N., 2008, Indium mineralization in  
18 epithermal Au-Ag-Cu-Mn-Te-(Se-Bi-Sn-Mo-In) vein-type deposits of the Kawazu (Rendaiji) mine,  
19 Shizuoka Prefecture, Japan: Intern Geol Congr Oslo, MRD-09 Au-Ag-telluride-selenide deposits, Abstract.  
20  
21 972 Shu, Q., Chang, Z., Lai, Y., Zhou, Y., Sun, Y., and Yan, C., 2016, Regional metallogeny of Mo-bearing  
22 deposits in northeastern China, with new Re-Os dates of porphyry Mo deposits in the northern  
23 Xilamulun district: *Economic Geology*, v. 111, p. 1783-1798.  
24  
25 974 Shvarov, Y., 2011, Unitherm Software, version 4.4.  
26  
27 975 Sillitoe, R.H., 2010, Porphyry copper systems: *Economic geology*, v. 105, p. 3-41.  
28  
29 976 Smoliar, M.I., Walker, R.J., and Morgan, J.W., 1996, Re-Os ages of group IIA, IIIA, IVA, and IVB iron  
30 meteorites: *Science*, v. 271, p. 1099-1102.  
31  
32 978 So, C.S., Dunchenko, V.Y., Yun, S.T., Park, M.E., Choi, S.G., and Shelton, K.L., 1995, Te- and Se-bearing  
33 epithermal Au-Ag mineralization, Prasolovskoye, Kunashir Island, Kuril Island arc: *Economic Geology*, v.  
34 90, p. 105-117.  
35  
36 980 Stein, H.J., Morgan, J.W., and Scherstén, A., 2000, Re-Os dating of low-level highly radiogenic (LLHR)  
37 sulfides: The Harnas gold deposit, southwest Sweden, records continental-scale tectonic  
38 events: *Economic Geology*, v. 95, p. 1657-1671.  
39  
40 982 Stern, R.A., and Amelin, Y., 2003, Assessment of errors in SIMS zircon U–Pb geochronology using a  
41 natural zircon standard and NIST SRM 610 glass: *Chemical Geology*, v. 197, p. 111-142.  
42  
43 983 Sun, S.S., and McDonough, W.S., 1989, Chemical and isotopic systematics of oceanic basalts:  
44  
45  
46  
47  
48  
49  
50  
51  
52  
53  
54  
55  
56  
57  
58  
59  
60  
61  
62  
63  
64  
65

1 992 implications for mantle composition and processes: Geological Society, London, Special Publications, v.  
2 993 42, p. 313-345.  
3  
4 994 Sun, W., Zhang, H., Ling, M.X., Ding, X., Chung, S.L., Zhou, J., Yang, X.Y., and Fan, W., 2011, The genetic  
5 995 association of adakites and Cu-Au ore deposits: International Geology Review, v. 53, p. 691-703.  
6  
7 996 Voudouris, P., 2011, Conditions of formation of the Mavrokoryfi high-sulfidation epithermal Cu-Ag-Au-  
8 997 Te mineralization (Petrota Graben, NE Greece): Mineralogy and Petrology, v. 101, p. 97-113.  
9  
10 998 Wan, B., Hegner, E., Zhang, L., Rocholl, A., Chen, Z., Wu, H., and Chen, F., 2009, Rb-Sr geochronology of  
11 999 chalcopyrite from the Chehugou porphyry Mo-Cu deposit (Northeast China) and geochemical  
12 1000 constraints on the origin of hosting granites: Economic Geology, v. 104, p. 351-363.  
13  
14 1001 Wang, C., 2015, Lead-zinc polymetallic metallogenic series and prospecting direction of  
15 1002 Huanggangliang-ganzhuermiao metallogenic belt, Inner Mongolia: Ph.D. thesis, Changchun, China, Jilin  
16 1003 University, 165 p. (in Chinese with English abstract).  
17  
18 1004 Wang, F., 2017, Magmatism and Ag-polymetallic mineralization in Shuangjianzishan deposit and its  
19 1005 periphery, Inner Mongolia: Ph.D. thesis, Wuhan, China, China University of Geosciences, 176 p. (in  
20 1006 Chinese with English abstract).  
21  
22 1007 Wang, F., Bagas, L., Jiang, S., and Liu, Y., 2017, Geological, geochemical, and geochronological  
23 1008 characteristics of Weilasituo Sn-polymetal deposit, Inner Mongolia, China: Ore Geology Reviews, v. 80,  
24 1009 p. 1206-1229.  
25  
26 1010 Wang, F., Sun, H., Pei, R., Liu, Y., Liu, C., and Jiang, S., 2016, The geologic features and genesis of  
27 1011 Shuangjianzishan silver-polymetallic deposit, Balinzuo Qi, Inner Mongolia: Geological Review, v. 62, p.  
28 1012 1241-1256 (in Chinese with English abstract).  
29  
30 1013 Wang, F., Zhou, X.H., Zhang, L.C., Ying, J.F., Zhang, Y.T., and Wu, F.Y., 2006, Timing of volcanism succession  
31 1014 of the Great Xing'an Range, northeastern Asia, and its tectonic significance: Earth Planetary Science  
32 1015 Letters, v. 251, p. 179-198.  
33  
34 1016 Wang, J., 2009, Chronology and geochemistry of granitoid for the Weilasituo copper polymetal deposit  
35 1017 in Inner Mongolia: Master thesis, China University of Geosciences Beijing, Beijing, China, 68 p. (in  
36 1018 Chinese with English abstract).  
37  
38 1019 Wang, J.B., Wang, Y.W., Wang, L.J., and Uemoto, T., 2001, Tin-polymetallic mineralization in the  
39 1020 southern part of the Da Hinggan Mountains, China: Resource Geology, v. 51, p. 283-291.  
40 1021 Wang, T., Guo, L., Zheng, Y.D., Donskaya, T., Gladkochub, D., Zeng, L.S., Li, J.B., Wang, Y.B., and

1 1022 Mazukabzov, A., 2012, Timing and processes of late Mesozoic mid-lower-crustal extension in continental  
2 1023 NE Asia and implications for the tectonic setting of the destruction of the North China Craton: mainly  
3  
4 1024 constrained by zircon U–Pb ages from metamorphic core complexes: *Lithos*, v. 154, p. 315-345.  
5  
6 1025 Wang, X.D., 2017, Magmatism and mineralization of Ag-Pb-Zn polymetallic deposits in the Lindong  
7  
8 1026 district, Inner Mongolia: Ph.D. thesis, Wuhan, China, China University of Geosciences, 175 p. (in Chinese  
9  
10 1027 with English abstract).  
11  
12 1028 Wei, C.S., Zhao, Z.F., and Spicuzza, M.J., 2008, Zircon oxygen isotopic constraint on the sources of late  
13  
14 1029 Mesozoic A-type granites in eastern China: *Chemical Geology*, v. 250, p. 1-15.  
15  
16 1030 Wiedenbeck, M., Alle, P., Corfu, F., Griffin, W.L., Meier, M., Oberli, F., Von Quadt, A., Roddick, J.C., and  
17  
18 1031 Spiegel, W., 1995, Three natural zircon standards for U-Th-Pb, Lu-Hf, trace element and REE analyses:  
19  
20 1032 *Geostandards Newsletter*, v. 19, p. 1-23.  
21  
22 1033 Wilde, S.A., 2015, Final amalgamation of the Central Asian Orogenic Belt in NE China: Paleo-Asian Ocean  
23  
24 1034 closure versus Paleo-Pacific plate subduction—A review of the evidence: *Tectonophysics*, v. 662, p. 345-  
25  
26 1035 362.  
27  
28 1036 Wilkinson, J.J., 2013, Triggers for the formation of porphyry ore deposits in magmatic arcs: *Nature*  
29  
30 1037 *Geoscience*, v. 6, p. 917.  
31  
32 1038 Williams-Jones, A.E., and Heinrich, C.A., 2005, 100th Anniversary special paper: Vapor transport of  
33  
34 1039 metals and the formation of magmatic-hydrothermal ore deposits: *Economic Geology*, v. 100, p. 1287-  
35  
36 1040 1312.  
37  
38 1041 Williams-Jones, A.E., and Migdisov, A.A., 2014, Experimental constraints on the transport and  
39  
40 1042 deposition of metals in ore-forming hydrothermal systems: *Society of Economic Geologists*, v. 18, p. 77-  
41  
42 1043 96.  
43  
44 1044 Wood, S.A., 1998, Calculation of activity-activity and  $\log fO_2$ -pH diagrams: *Reviews in Economic*  
45  
46 1045 *Geology*, v. 10, p. 81-96.  
47  
48 1046 Wu, F.Y., Lin, J.Q., Wilde, S.A., Zhang, X.O., and Yang, J.H., 2005, Nature and significance of the Early  
49  
50 1047 Cretaceous giant igneous event in eastern China: *Earth and Planetary Science Letters*, v. 233, p. 103-119.  
51  
52 1048 Wu, F.Y., Sun, D.Y., Ge, W.C., Zhang, Y.B., Grant, M.L., Wilde, S.A., and Jahn, B.M., 2011, Geochronology  
53  
54 1049 of the Phanerozoic granitoids in northeastern China: *Journal of Asian Earth Sciences*, v. 41, p. 1-30.  
55  
56 1050 Wu, F.Y., Sun, D.Y., Li, H.M., Jahn, B.M., and Wilde, S.A., 2002, A-type granites in northeastern China: age  
57  
58 1051 and geochemical constraints on their petrogenesis: *Chemical Geology*, v. 187, p. 143-173.  
59  
60  
61  
62  
63  
64  
65

1 1052 Wu, G., 2014, Research of silver mineralization in central-southern segment of the Great Xing'an Range  
2 1053 - A case study of the Shuangjianzishan silver deposit, Inner Mongolia: Ph.D. thesis, University of Chinese  
3 1054 Academy of Sciences, Beijing, China, 136 p. (in Chinese with English abstract).  
4  
5 1055 Wu, G., Liu, J., Zeng, Q., Liu, M., Sun, H., Yin, Z., and Yin, X., 2014, Occurrences of silver in the  
6 1056 Shuangjianzishan Pb-Zn-Ag deposit and its implications for mineral processing: *Earth Science Frontiers*,  
7 1057 v. 21, p. 105-115 (in Chinese with English abstract).  
8  
9 1058 Wu, G., Liu, J., Zeng, Q., Sun, H., and Liu, M., 2013, The metallogenic age of Shuangjianzishan Ag-Pb-Zn  
10 1059 deposit of Greate Hinggan Range, Inner Mongolia: *Acta Mineralogica Sinica*, v. 33, p. 619 (in Chinese).  
11  
12 1060 Wu, X.L., Mao, J.W., Zhou, Z.H., and Ouyang, H.G., 2012, H-O-S-Pb isotopic components of the  
13 1061 Budunhua Cu deposit in the middle-south part of the Da Hinggan Mountains and their implications for  
14 1062 the ore-forming process: *Geology in China*, v. 39, p. 1812-1829 (in Chinese with English abstract).  
15  
16 1063 Xiao, W.J., Zhang, L.C., Qin, K.Z., Sun, S., and Li, J.L., 2004, Paleozoic accretionary and collisional tectonics  
17 1064 of the eastern Tianshan China: Implication for the continental growth of central Asia: *American Journal*  
18 1065 *of Science*, v. 304, p. 370-395.  
19  
20 1066 Yao, M.J., Liu, J.J., Zhai, D.G., and Wang, J.P., 2012, Sulfur and lead isotopic compositions of the  
21 1067 polymetallic deposits in the southern Great Xing'an Range: some implications for metal sources: *Journal*  
22 1068 *of Jilin University (Earth Science Edition)*, v. 42, p. 362-373 (in Chinese with English abstract).  
23  
24 1069 Yuan, H., Yin, C., Liu, X., Chen, K., Bao, Z., Zong, C., Dai, M., Lai, S., Wang, R., and Jiang, S., 2015, High  
25 1070 precision in-situ Pb isotopic analysis of sulfide minerals by femtosecond laser ablation multi-collector  
26 1071 inductively coupled plasma mass spectrometry: *Science China Earth Sciences*, v. 58, p. 1713-1721.  
27  
28 1072 Zeng, Q., Liu, J., Chu, S., Guo, Y., Gao, S., Guo, L., and Zhai, Y., 2016, Poly-metal mineralization and  
29 1073 exploration potential in southern segment of the Da Hinggan Mountains: *Journal of Jilin University*  
30 1074 *(Earth Science Edition)*, v. 46, p. 1100-1123 (in Chinese with English abstract).  
31  
32 1075 Zeng, Q., Qin, K., Liu, J., Li, G., Zhai, M., Chu, S., and Guo, Y., 2015, Porphyry molybdenum deposits in  
33 1076 the Tianshan-Xingmeng orogenic belt, northern China: *International Journal of Earth Sciences*, v. 104,  
34 1077 p. 991-1023.  
35  
36 1078 Zeng, Q.D., Liu, J.M., Zhang, Z.L., Chen, W.J., and Zhang, W.Q., 2011, Geology geochronology of the  
37 1079 Xilamulun molybdenum metallogenic belt in eastern Inner Mongolia, China: *International Journal of*  
38 1080 *Earth Sciences*, v. 100, p. 1791-1809.

1 1081 Zeng, Q.D., Liu, J.M., Zhang, Z.L., Jia, C.S., Yu, C.M., Ye, J., and Liu, H.T., 2009, Geology and lead-isotope  
2 1082 study of the Baiyinnuoer Zn-Pb-Ag deposit, south segment of the Da Hinggan Mountains, Northeastern  
3  
4 1083 China: *Resource Geology*, v. 59, p. 170-180.  
5  
6 1084 Zhai, D., Bindi, L., Voudouris, P.C., Liu, J., Tombros, S.F., and Li, K., 2019c, Discovery of Se-rich canfieldite,  
7 1085  $\text{Ag}_3\text{Sn}(\text{S}, \text{Se})_6$ , from the Shuangjianzishan Ag-Pb-Zn deposit, NE China: A multimethodic chemical and  
8 1086 structural study: *Mineralogical Magazine*, v. 83, p. 419-426.  
9  
10 1087 Zhai, D., Williams-Jones, A.E., Liu, J., Selby, D., Li, C., Huang, X.W., Qi, L., and Guo, D., 2019b, Evaluating  
11 1088 the use of the molybdenite Re-Os chronometer in dating gold mineralization: Evidence from the Haigou  
12 1089 deposit, NE China: *Economic Geology* (in press).  
13  
14 1090 Zhai, D., Liu, J., Cook, N.J., Wang, X., Yang, Y., Zhang, A., and Jiao, Y., 2019a, Mineralogical, textural, sulfur  
15 1091 and lead isotope constraints on the origin of Ag-Pb-Zn mineralization at Bianjiadayuan, Inner Mongolia,  
16 1092 NE China: *Mineralium Deposita*, v. 54, p. 47-66.  
17  
18 1093 Zhai, D., Williams-Jones, A.E., Liu, J., Tombros, S.F., Cook, N.J., 2018a, Mineralogical, fluid inclusion and  
19 1094 multiple isotope (H-O-S-Pb) constraints on the genesis of the Sandaowanzi epithermal Au-Ag-Te deposit,  
20 1095 NE China: *Economic Geology*, v. 113, p. 1359-1382.  
21  
22 1096 Zhai, D., Liu, J., Li, J., Zhang, M., Li, B., Fu, X., Jiang, H., Ma, L., and Qi, L., 2016, Geochronological study  
23 1097 of Weilasituo porphyry type Sn deposit in Inner Mongolia and its geological significance: *Mineral*  
24 1098 *Deposits*, v. 35, p. 1011-1022 (in Chinese with English abstract).  
25  
26 1099 Zhai, D., Liu, J., Ripley, E.M., and Wang, J., 2015, Geochronological and He-Ar-S isotopic constraints on  
27 1100 the origin of the Sandaowanzi gold-telluride deposit, northeastern China: *Lithos*, v. 212, p. 338-352.  
28  
29 1101 Zhai, D., Liu, J., Tombros, S., and Williams-Jones, A.E., 2018b, The genesis of the Hashitu porphyry  
30 1102 molybdenum deposit, Inner Mongolia, NE China: constraints from mineralogical, fluid inclusion, and  
31 1103 multiple isotope (H, O, S, Mo, Pb) studies: *Mineralium Deposita*, v. 53, p. 377-397.  
32  
33 1104 Zhai, D., Liu, J., Wang, J., Yang, Y., Zhang, H., Wang, X., Zhang, Q., Wang, G., and Liu, Z., 2014a, Zircon U-  
34 1105 Pb and molybdenite Re-Os geochronology, and whole-rock geochemistry of the Hashitu molybdenum  
35 1106 deposit and host granitoids, Inner Mongolia, NE China: *Journal of Asian Earth Sciences*, v. 79, p. 144-  
36 1107 160.  
37  
38 1108 Zhai, D., Liu, J., Zhang, A., and Sun, Y., 2017, U-Pb, Re-Os and  $^{40}\text{Ar}/^{39}\text{Ar}$  geochronology of porphyry Sn  $\pm$   
39 1109 Cu  $\pm$  Mo and polymetallic (Ag-Pb-Zn-Cu) vein mineralization at Bianjiadayuan, Inner Mongolia, NE China:  
40 1110 Implications for discrete mineralization events: *Economic Geology*, v. 112, p. 2041-2059.  
41  
42 1111 Zhai, D., Liu, J., Zhang, H., Tombros, S., and Zhang, A., 2018c, A magmatic-hydrothermal origin for Ag-  
43 1112 Pb-Zn vein formation at the Bianjiadayuan deposit, Inner Mongolia, NE China: Evidences from fluid  
44 1113 inclusion, stable (C-H-O) and noble gas isotope studies: *Ore Geology Reviews*, v. 101, p. 1-16.  
45  
46 1114 Zhai, D., Liu, J., Zhang, H., Yao, M., Wang, J., and Yang, Y., 2014b, S-Pb isotopic geochemistry, U-Pb and

1 1115 Re-Os geochronology of the Huanggangliang Fe-Sn deposit, Inner Mongolia, NE China: Ore Geology  
2 1116 Reviews, v. 59, p. 109-122.

3 1117 Zhang, F.Q., Chen, H.L., Yu, X., Dong, C.W., Yang, S.F., Pang, Y.M., and Batt, G.E., 2011, Early Cretaceous  
4 1118 volcanism in the northern Songliao Basin, NE China, and its geodynamic implication: Gondwana  
5 1119 Research, v. 19, p. 163-176.

6 1120 Zhang, J.H., Gao, S., Ge, W.C., Wu, F.Y., Yang, J.H., Wilde, S.A., and Li, M., 2010, Geochronology of the  
7 1121 Mesozoic volcanic rocks in the Great Xing'an Range, northeastern China: implications for subduction-  
8 1122 induced delamination: Chemical Geology, v. 276, p. 144-165.

9 1123 Zhang, L.C., Zhou, X.H., Ying, J.F., Wang, F., Guo, F., Wan, B., and Chen, Z.G., 2008, Geochemistry and  
10 1124 Sr-Nd-Pb-Hf isotopes of Early Cretaceous basalts from the Great Xinggan Range, NE China: Implications  
11 1125 for their origin and mantle source characteristics: Chemical Geology, v. 256, p. 12-23.

12 1126 Zhang, L.G., Liu, J.X., and Wang, K.F., 1995, Block geology of eastern Asia lithosphere: Isotope  
13 1127 geochemistry and dynamics of upper mantle, basement and granite. Beijing: Science Press, 252 p. (in  
14 1128 Chinese with English abstract).

15 1129 Zhang, Z., 2018, Geological and geochemical characteristics and metallogenic mechanism of the  
16 1130 Shuangjianzishan Ag-polymetallic deposit, Inner Mongolia, Master thesis, Beijing, China, China  
17 1131 University of Geosciences Beijing, 64 p. (in Chinese with English abstract).

18 1132 Zhou, J.B., Wilde, S.A., Zhao, G.C., and Han, J., 2018, Nature and assembly of microcontinental blocks  
19 1133 within the Paleo-Asian Ocean: Earth-Science Reviews, v. 186, p. 76-93.

20 1134 Zhou, Z.H., Ouyang, H.G., Wu, X.L., Liu, J., and Che, H.W., 2014, Geochronology and geochemistry study  
21 1135 of the biotite granite from the Daolundaba Cu-W polymetallic deposit in the Inner Mogolia and its  
22 1136 geological significance: Acta Petrologica Sinica, v. 30, p. 79-94 (in Chinese with English abstract).

23 1137 Zhu, X.Y., Zhang, Z.H., Fu, X., Li, B.Y., Wang, Y.L., Jiao, S.T., and Sun, Y.L., 2016, Geological and geochemical  
24 1138 characteristics of the Weilasito Sn-Zn deposit, Inner Mongolia: Geology in China, v. 43, p. 188-208 (in  
25 1139 Chinese with English abstract).

26 1140

27 1141 **Figure Captions**

28 1142 Figure 1 (A) A tectonic map of the Central Asian Orogenic Belt (based on Jahn et al., 2000); (B) A  
29 1143 geological map of the Great Hinggan Range (GHR) in NE China showing the distribution of the Mesozoic  
30 1144 granites and volcanic rocks (modified from Qi et al., 2005); (C) A geological map of the southern GHR

1 1145 showing the locations and ages of major ore deposits (modified from Zhai et al., 2017).  
2  
3 1146  
4 1147 Figure 2 (A) A geological map of the Shuangjianshishan ore district (based on Wu et al., 2014); (B) A  
5  
6 1148 vertical section through the ore deposit (modified from Wang, 2015).  
7  
8 1149  
9  
10 1150 Figure 3 Core logs of two drill holes showing the distribution of granite porphyry and Mo mineralization  
11  
12 1151 (A), and a diorite dike and Ag-Pb-Zn mineralization (B). Also shown are the locations of samples used in  
13  
14 1152 geochronological analyses. Abbreviations: Ab-albite; Mo-molybdenite; Cal-calcite; Qtz-quartz.  
15  
16 1153  
17  
18 1154 Figure 4 (A) Oxidized mineralized veins hosted in slate near the erosional surface; (B) Major and parallel  
19  
20 1155 Ag-Pb-Zn-quartz veins hosted by slate associated with an alteration assemblage of chlorite-sericite-  
21  
22 1156 quartz; (C) Early formed pyrite veinlets within slate enclosed as breccias in subsequent massive Ag-Pb-  
23  
24 1157 Zn quartz-calcite veins; (D) Early quartz-pyrite veins crosscut by Ag-Pb-Zn mineralized quartz-calcite  
25  
26 1158 veins, and a late stage quartz vein crosscutting the Ag-Pb-Zn mineralized veins; (E) Massive Ag-Pb-Zn  
27  
28 1159 ore with a very high Ag grade (>32,000 g/t) from a major mineralized vein; (F) Massive sulfide ore  
29  
30 1160 comprising galena, sphalerite and pyrite; (G) Slate as breccia fragments cemented by quartz, calcite and  
31  
32 1161 sulfides. Abbreviations: Cal-calcite; Chl-chlorite; Gn-galena; Py-pyrite; Q-Quaternary gravel; Qtz-quartz;  
33  
34 1162 Sec-sericite; Sp-sphalerite.  
35  
36 1163  
37  
38 1164 Figure 5 The paragenetic sequence for the Shuangjianshishan Ag-Pb-Zn mineralization.  
39  
40 1165  
41  
42 1166 Figure 6 Photomicrographs of ore textures involving silver-bearing minerals, and mineral assemblages  
43  
44 1167 from the Shuangjianshishan deposit. (A) Galena and sphalerite replaced by argentite and canfieldite  
45  
46 1168 coexisting with sericite and quartz (BSE); (B) Early pyrite surrounded by later chalcopyrite, which was  
47  
48 1169 replaced by argentite and canfieldite (reflected light); (C) Canfieldite intergrown with freibergite that  
49  
50 1170 replaced sphalerite and galena (reflected light); (D) Galena and chalcopyrite associated with freibergite  
51  
52 1171 and canfieldite (reflected light); (E) Argentite after galena, sphalerite and chalcopyrite (BSE); (F) Late  
53  
54 1172 argentite as veins cutting galena (reflected light); (G) Ellipsoidal inclusions of freibergite, pyrargyrite and  
55  
56 1173 pyrrhotite within galena (BSE); (H) Coexisting stephanite and freibergite that replaced galena and  
57  
58 1174 sphalerite (reflected light); (I) Polybasite associated with quartz and sericite after galena (BSE).  
59  
60  
61  
62  
63  
64  
65

1 1175 Abbreviations: Arg-argentite; Caf-canfieldite; Ccp-chalcopyrite; Frb-freibergite; Gn-galena; Po-  
2 1176 pyrrhotite; Pol-polybasite; Py-pyrite; Pyr-pyrargyrite; Qtz-quartz; Sec-sericite; Sp-sphalerite; Ste-  
3  
4 1177 stephanite.  
5  
6 1178  
7  
8 1179 Figure 7 Reflected light (A) and EPM element maps (B-I) of canfieldite and argentite. Abbreviations: Arg-  
9  
10 1180 argentite; Caf-canfieldite; Cas-cassiterite; Ccp-chalcopyrite; Sp-sphalerite.  
11  
12 1181  
13  
14 1182 Figure 8 Locations of in situ spot sulfur isotopic analyses of sulfide and sulfosalt minerals and  
15  
16 1183 corresponding  $\delta^{34}\text{S}$  values. (A): Galena and sphalerite; (B): A single galena crystal; (C): Freibergite and  
17  
18 1184 galena; (D): Pyrargyrite, canfieldite and galena. Abbreviations: Caf-canfieldite; Frb-freibergite; Gn-  
19  
20 1185 galena; Ccp-chalcopyrite; Pyr-pyrargyrite; Qtz-quartz; Sp-sphalerite.  
21  
22 1186  
23  
24 1187 Figure 9 (A) A histogram of  $\delta^{34}\text{S}$  values for various ore minerals from the different ore stages; (B)  $\delta^{34}\text{S}$   
25  
26 1188 values for ore minerals versus depth.  
27  
28 1189  
29  
30 1190 Figure 10 Binary plots of  $^{206}\text{Pb}/^{204}\text{Pb}$  vs.  $^{207}\text{Pb}/^{204}\text{Pb}$  (A) and  $^{206}\text{Pb}/^{204}\text{Pb}$  vs.  $^{208}\text{Pb}/^{204}\text{Pb}$  (B) for ore minerals  
31  
32 1191 from the Shuangjianzishan deposit.  
33  
34 1192  
35  
36 1193 Figure 11 Zircon U-Pb ages for igneous rocks from the Shuangjianzishan deposit. (A): Diorite dike; (B):  
37  
38 1194 Dacite; (C): Granite intrusion; (D): Coarse-grained granite porphyry; (E): Fine-grained granite porphyry.  
39  
40 1195  
41  
42 1196 Figure 12 Molar  $\text{Ag}/(\text{Ag}+\text{Cu})$  and  $\text{Zn}/(\text{Zn}+\text{Fe})$  plots for primary freibergite in the Shuangjianzishan  
43  
44 1197 deposit. The isotherms were calculated from Sack (2005). These isotherms terminate at low  $\text{Zn}/(\text{Zn}+\text{Fe})$   
45  
46 1198 and high  $\text{Ag}/(\text{Ag}+\text{Cu})$  ratios because of saturation with respect to pyrrhotite (Po) (Balabin and Sack,  
47  
48 1199 2000).  
49  
50 1200  
51  
52 1201 Figure 13 Lead isotope plots of the Shuangjianzishan ore minerals compared to local magmatic-  
53  
54 1202 hydrothermal deposits and various rock units. The Pb isotope data for local Mesozoic granite, andesite  
55  
56 1203 and basalt, Paleozoic granite, Permian slate, and sulfides from the nearby magmatic-hydrothermal  
57  
58 1204 deposits were taken from the literature (Zhang et al., 1995, 2008; Shen and Fu, 1999; Chu et al., 2001;  
59  
60  
61  
62  
63  
64  
65

1 1205 Cai et al., 2004; Wang, 2009; Zeng et al., 2009; Guo et al., 2010; Jiang et al., 2010; Shao et al., 2010; Yao  
2 1206 et al., 2012; Wu et al., 2012; Zhai et al., 2014b, 2018b, 2019a). The Pb isotope ratios for the  
3  
4 1207 Shuangjianzishan deposit are similar to those of the local Mesozoic granite and adjacent ore deposits.  
5  
6 1208 (A):  $^{206}\text{Pb}/^{204}\text{Pb}$  vs.  $^{207}\text{Pb}/^{204}\text{Pb}$  plots; (B):  $^{206}\text{Pb}/^{204}\text{Pb}$  vs.  $^{208}\text{Pb}/^{204}\text{Pb}$  plots.  
7  
8 1209  
9  
10 1210 Figure 14  $\text{Log}f\text{O}_2$ -pH diagrams showing stability relationships in the Fe-O-S system and alteration  
11 1211 assemblages for Ag-Pb-Zn mineralization in the Shuangjianzishan deposit at 250 °C (A) and 200 °C (B)  
12 1212 and 300 bars. The calculations assumed an aqueous fluid with a  $\Sigma a\text{S}$  value of 0.01 and a  $\delta^{34}\text{S}_{\Sigma\text{S}}$  value of  
13 1213 +0.5‰. The diagrams show the predominance boundaries of aqueous sulfur species (pink dashed),  
14 1214 mineral stability in the Fe-O-S system (black solid), alteration equilibra (grey solid), and calcite  
15 1215 dissolution (black dashed). The kaolinite–muscovite and K–feldspar–muscovite stability fields are for a  
16 1216 solution with a  $\text{K}^+$  activity of 0.001. The stability boundary for calcite is for  $\Sigma\text{C} = 1$  m (based on Ohmoto,  
17 1217 1972). The sulfur isotope contours are indicated by blue lines. The grey area represents the approximate  
18 1218 stability field for the ore minerals. Phase and predominance boundaries were constructed using the HCh  
19 1219 software package (Shvarov, 2011). Abbreviations: Hem-hematite; Kfs-K-feldspar; Kln-kaolinite; Mag-  
20 1220 magnetite; Mus-muscovite; Po-pyrrhotite; Py-pyrite .  
21  
22 1221  
23 1222 Figure 15 (A) A chronology of magmatic and mineralization events in the Shuangjianzishan ore district;  
24 1223 some of the data are from the literature (Wu, 2014; Cui, 2015; Liu, C., et al., 2016; Gu et al., 2017; Zhang,  
25 1224 2018). The uncertainty for all the data is  $2\sigma$ ; (B)-(D): Cartoons illustrating the sequence of magmatic and  
26 1225 mineralizing events from ~252 to 132 Ma in the Shuangjianzishan ore district.  
27  
28 1226  
29  
30 1227 **Appendix Data**  
31  
32 1228 Figure A1 A total alkali vs. silica diagram illustrating the classification of the magmatic rocks at  
33 1229 Shuangjianzishan (after Middlemost, 1994). The alkaline/subalkaline boundary is from Irvine and  
34 1230 Baragar (1971). Some of the petrochemical data are from Gu et al. (2017) and Zhang (2018).  
35  
36 1231  
37  
38 1232 Figure A2 Geochemical data for the magmatic rocks in the Shuangjianzishan ore district. (A)-(D): Harker  
39 1233 diagrams of  $\text{Al}_2\text{O}_3$ , CaO, MgO and  $\text{TiO}_2$  versus  $\text{SiO}_2$ ; (E) A  $\text{K}_2\text{O}$ - $\text{SiO}_2$  diagram (Rickwood, 1989); (F) A A/NK-  
40 1234 A/CNK diagram (Maniar and Piccoli, 1989).

1 1235  
2 1236 Figure A3 Trace element diagrams for the granite porphyry and dacite. (A) Rare earth element profiles  
3  
4 1237 normalized to the CI chondrite of McDonough and Sun (1995); (B) Spider diagram of trace elements  
5  
6 1238 normalized to the primitive mantle composition of Sun and McDonough (1989).  
7  
8 1239  
9  
10 1240 Figure A4 A histogram of temperatures determined using sulfur isotope geothermometry.  
11  
12 1241  
13  
14 1242 Figure A5 Comparisons of the Pb isotope ratios obtained using in situ and conventional (mineral  
15  
16 separates) analytical methods; the mineral separate data are from Wang, F. (2017). (A):  $^{206}\text{Pb}/^{204}\text{Pb}$   
17 1243 versus  $^{207}\text{Pb}/^{204}\text{Pb}$ ; (B):  $^{206}\text{Pb}/^{204}\text{Pb}$  versus  $^{208}\text{Pb}/^{204}\text{Pb}$ .  
18 1244  
19 1245  
20  
21 1246 Figure A6 Trace element tectonic discrimination diagrams. (A) Sr/Y versus Y (Defant and Drummond,  
22  
23 1993); (B) Y + Nb versus Rb (Pearce et al., 1984).  
24 1247  
25 1248  
26  
27 1249 Table A1 Electron microprobe-determined compositions of sulfides and sulfosalts from the  
28  
29 Shuangjianzishan Ag-Pb-Zn deposit (wt.%).  
30 1250  
31 1251  
32  
33 1252 Table A2 LA-ICP-MS zircon U-Pb isotopic data for various igneous rocks from the Shuangjianzishan  
34  
35 deposit.  
36 1253  
37 1254  
38  
39 1255 Table A3 Lead isotope ratios for sulfides from ore deposits and a variety of rock units in the southern  
40  
41 GRH region.  
42 1256  
43 1257  
44  
45  
46  
47  
48  
49  
50  
51  
52  
53  
54  
55  
56  
57  
58  
59  
60  
61  
62  
63  
64  
65

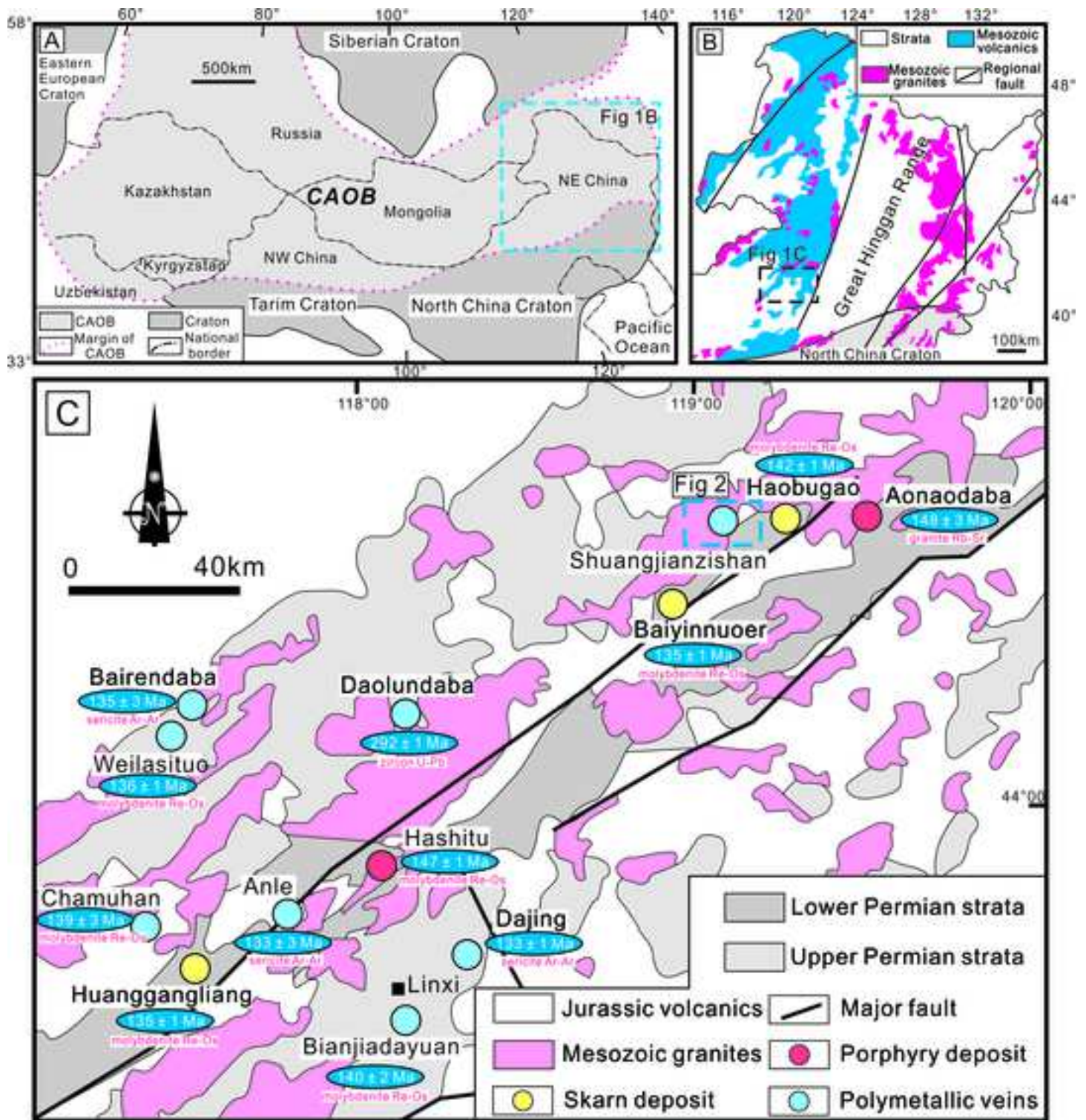
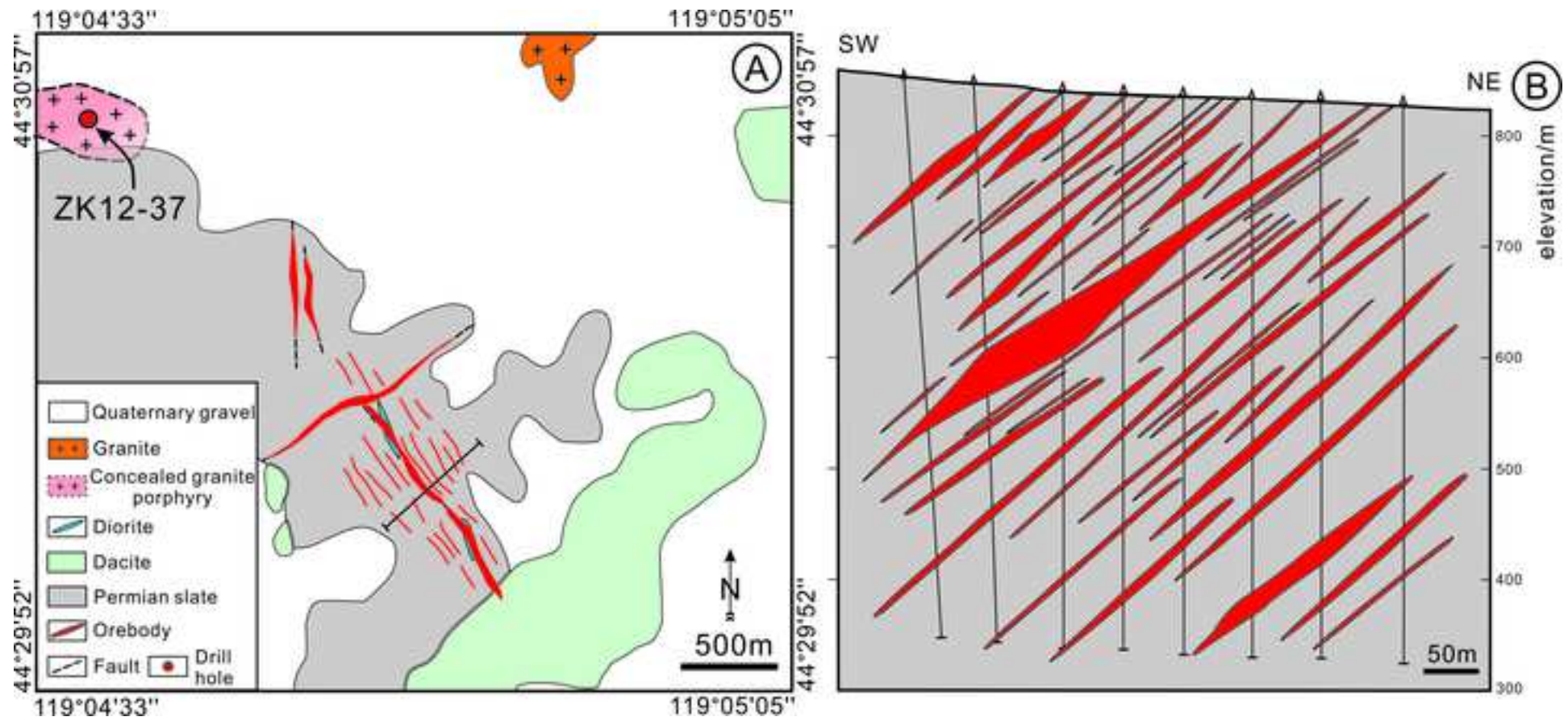
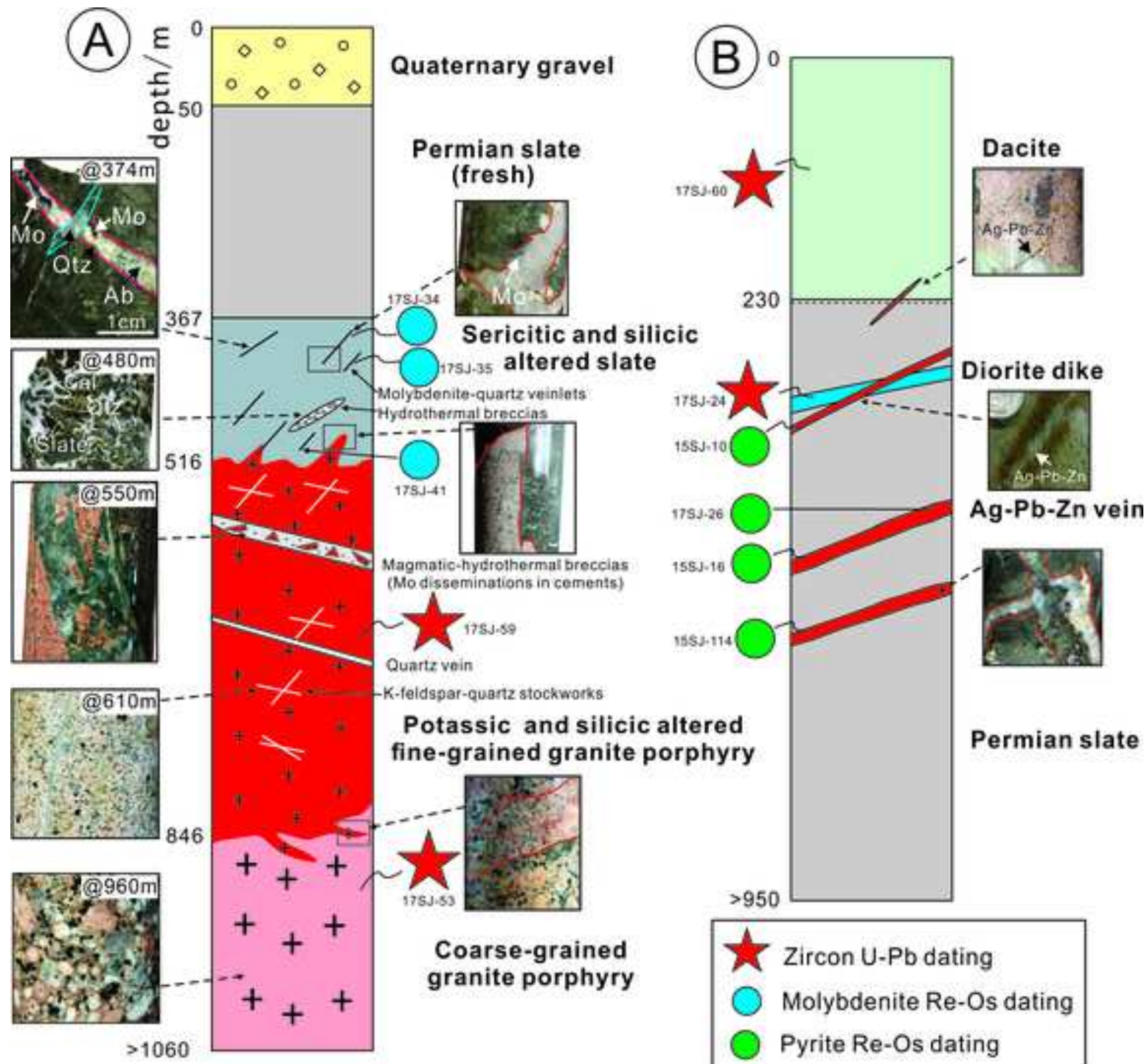
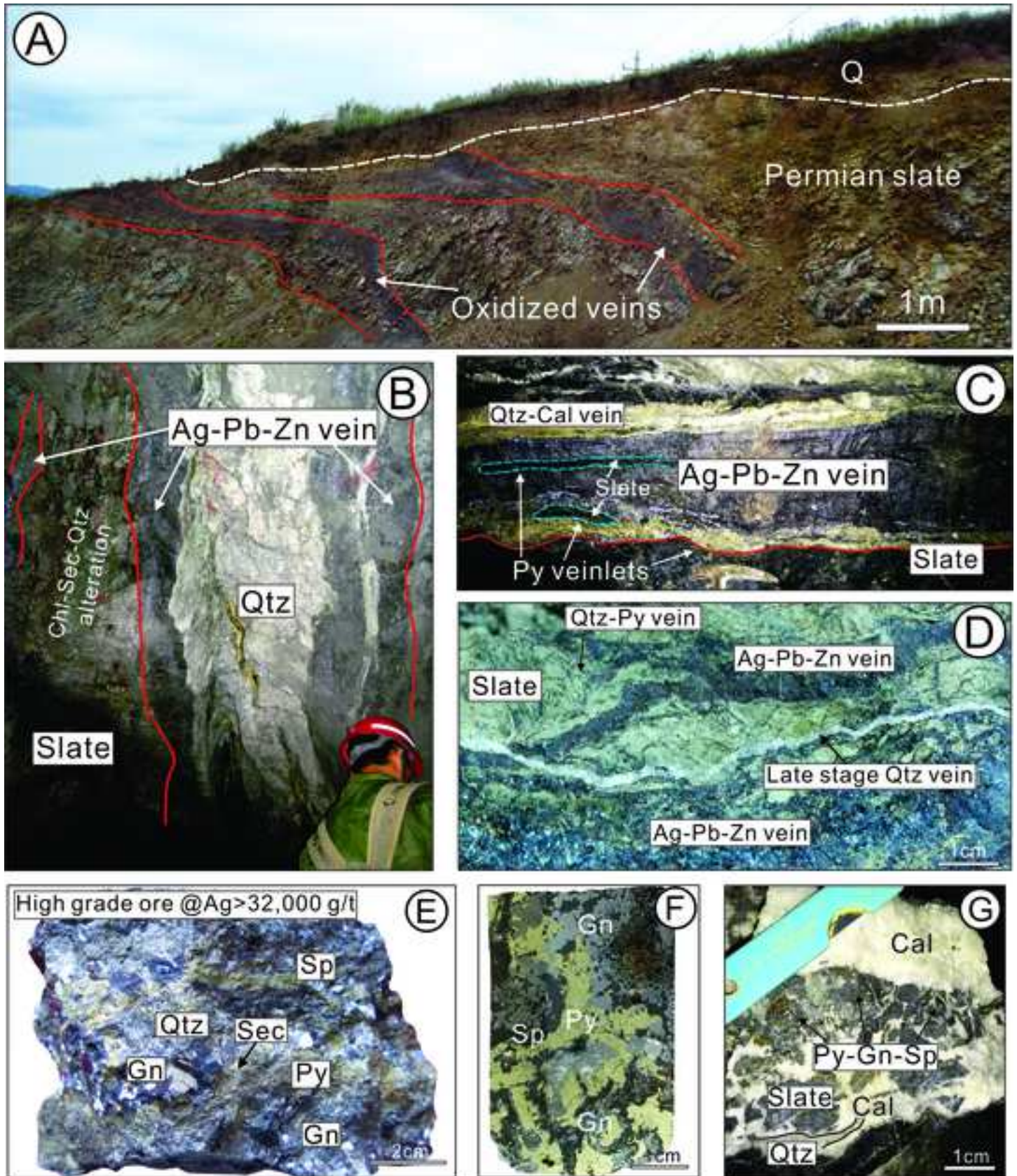


Figure 2

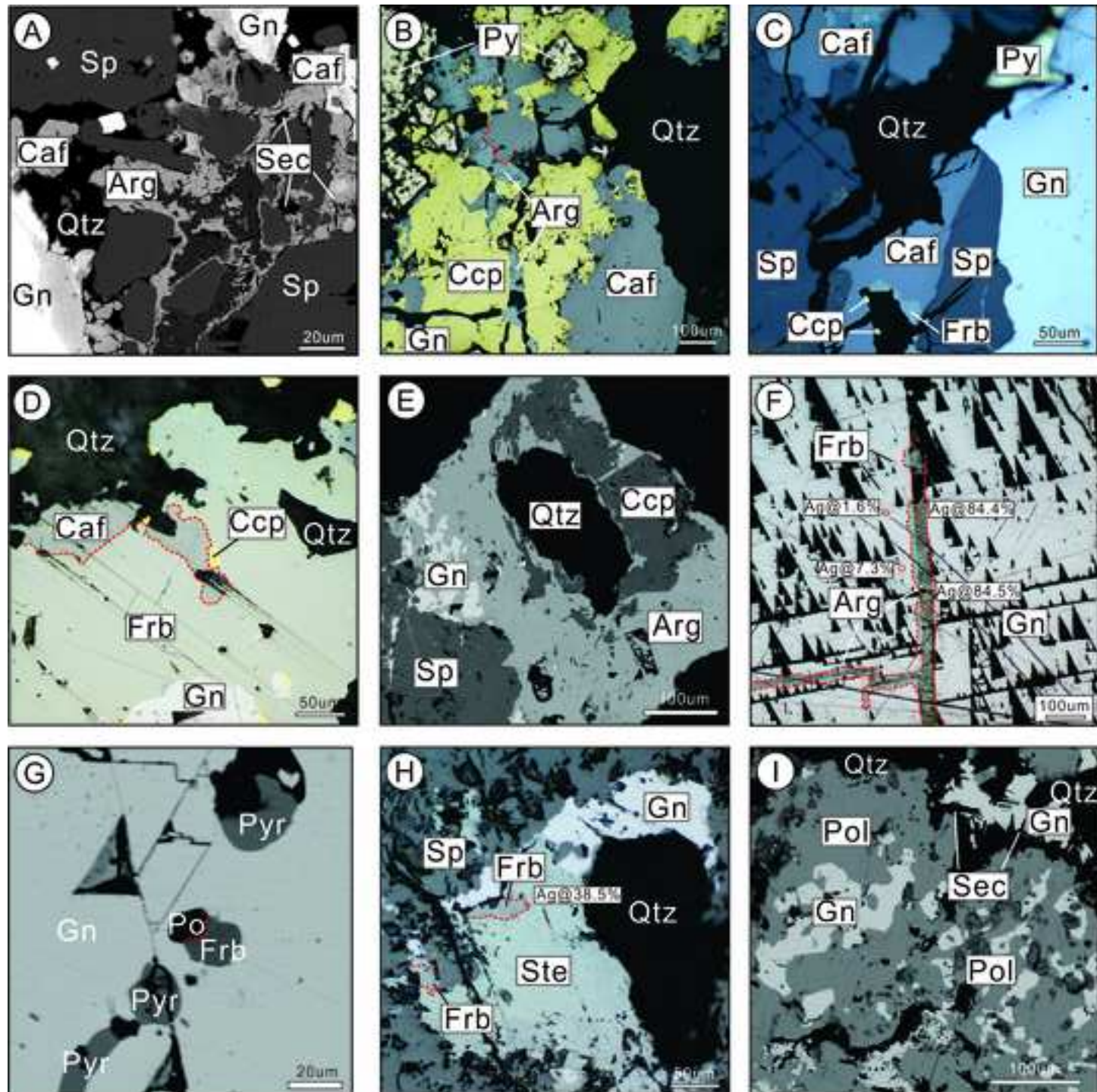
[Click here to access/download;Figure;Fig 2 ore deposit geol-revised.jpg](#)

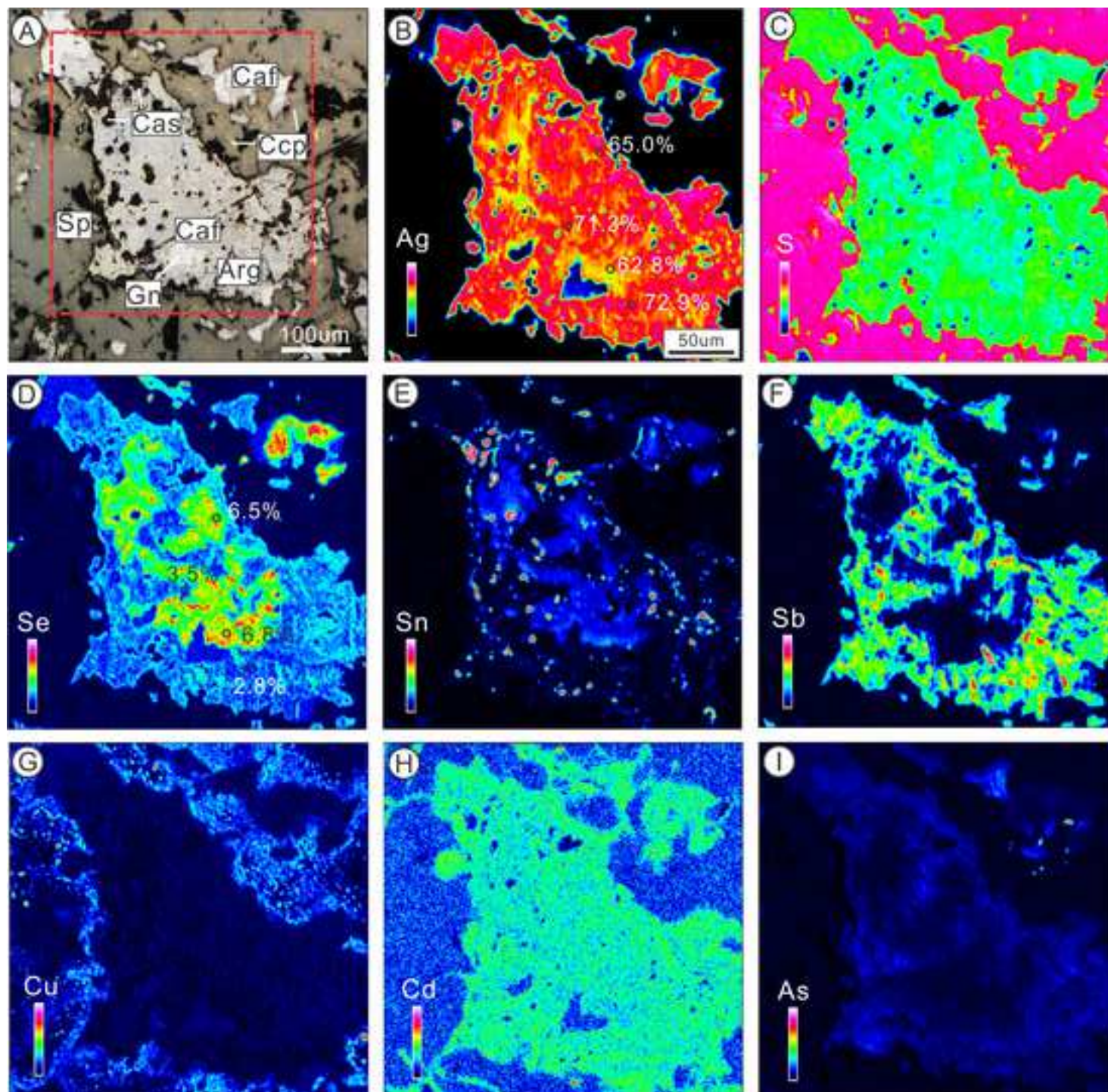


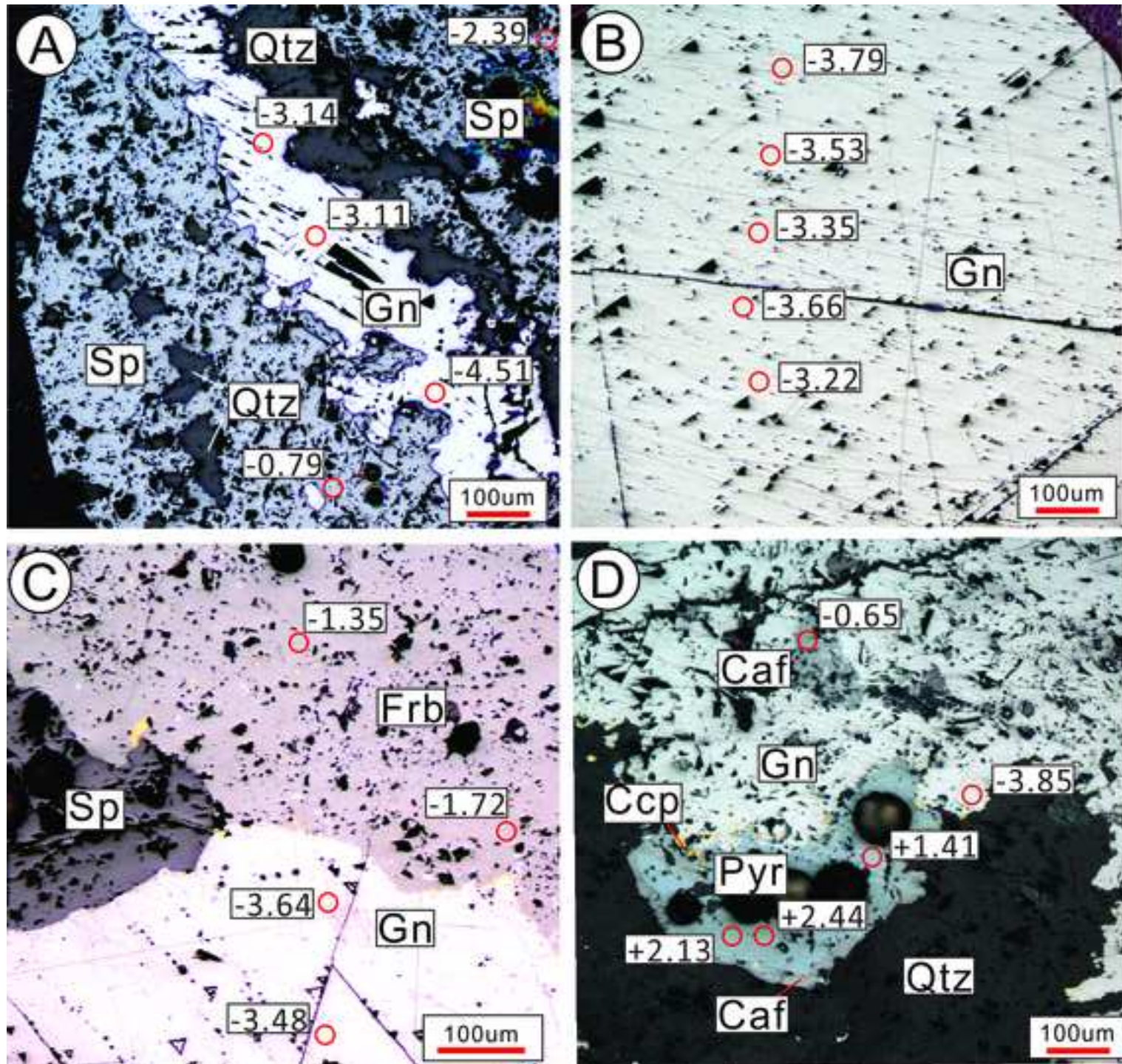


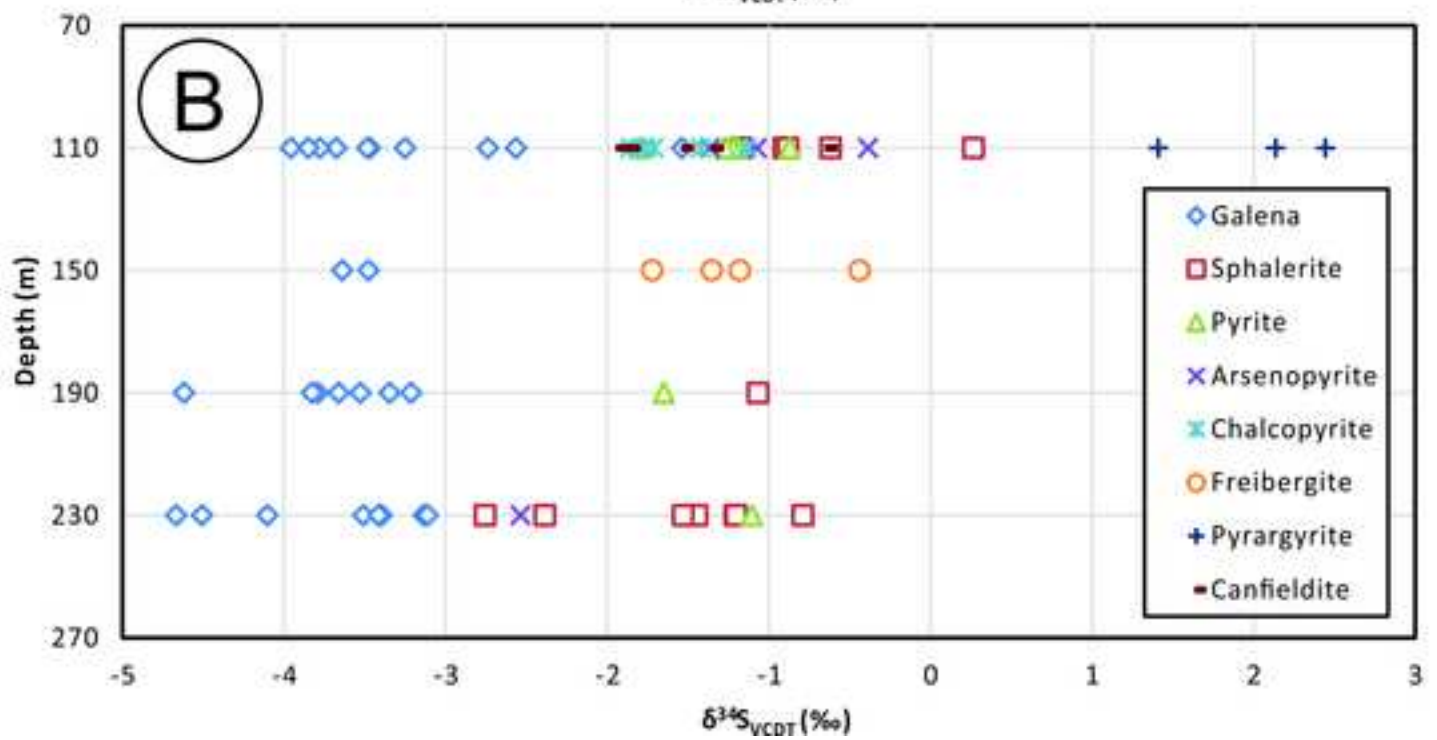
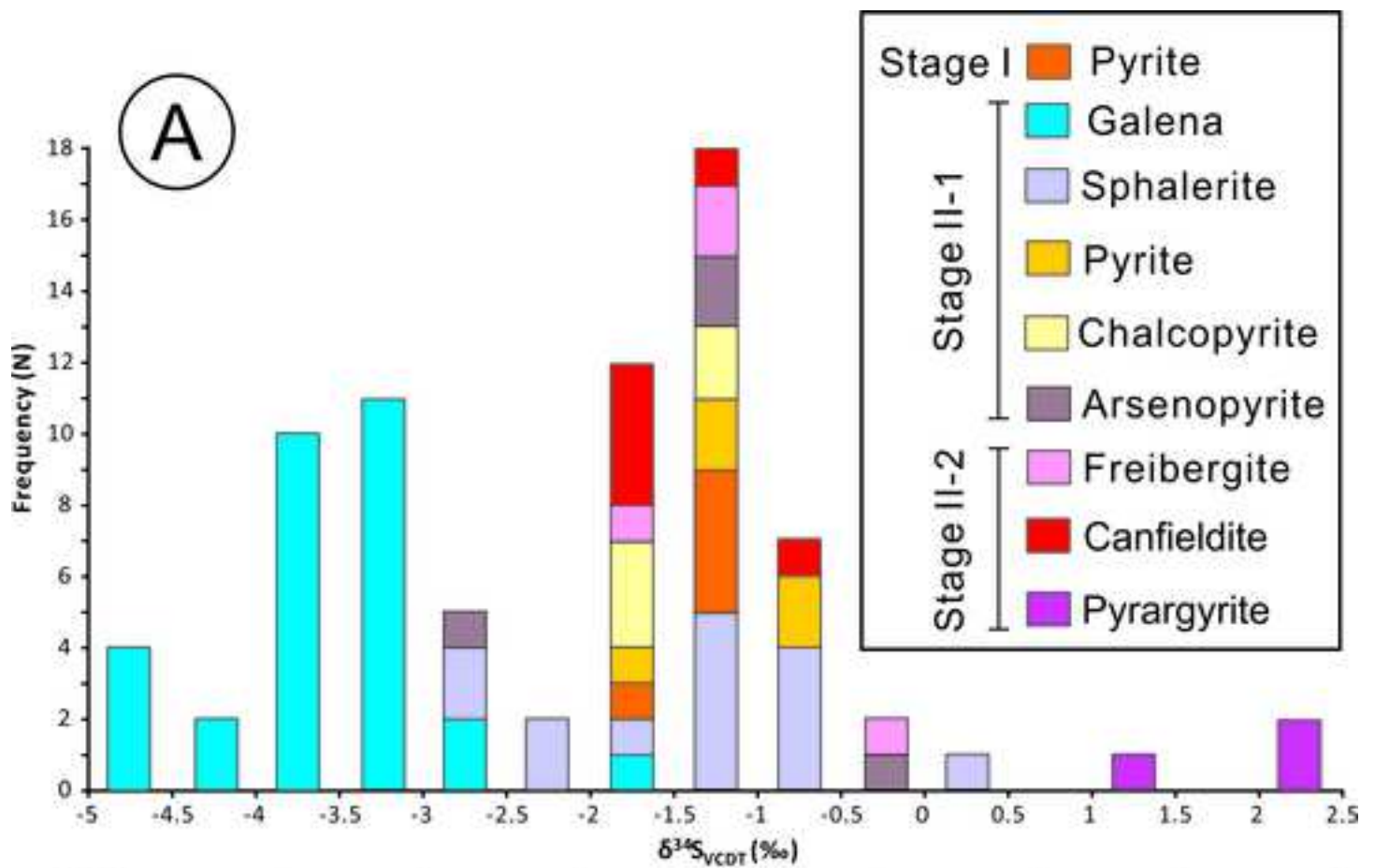


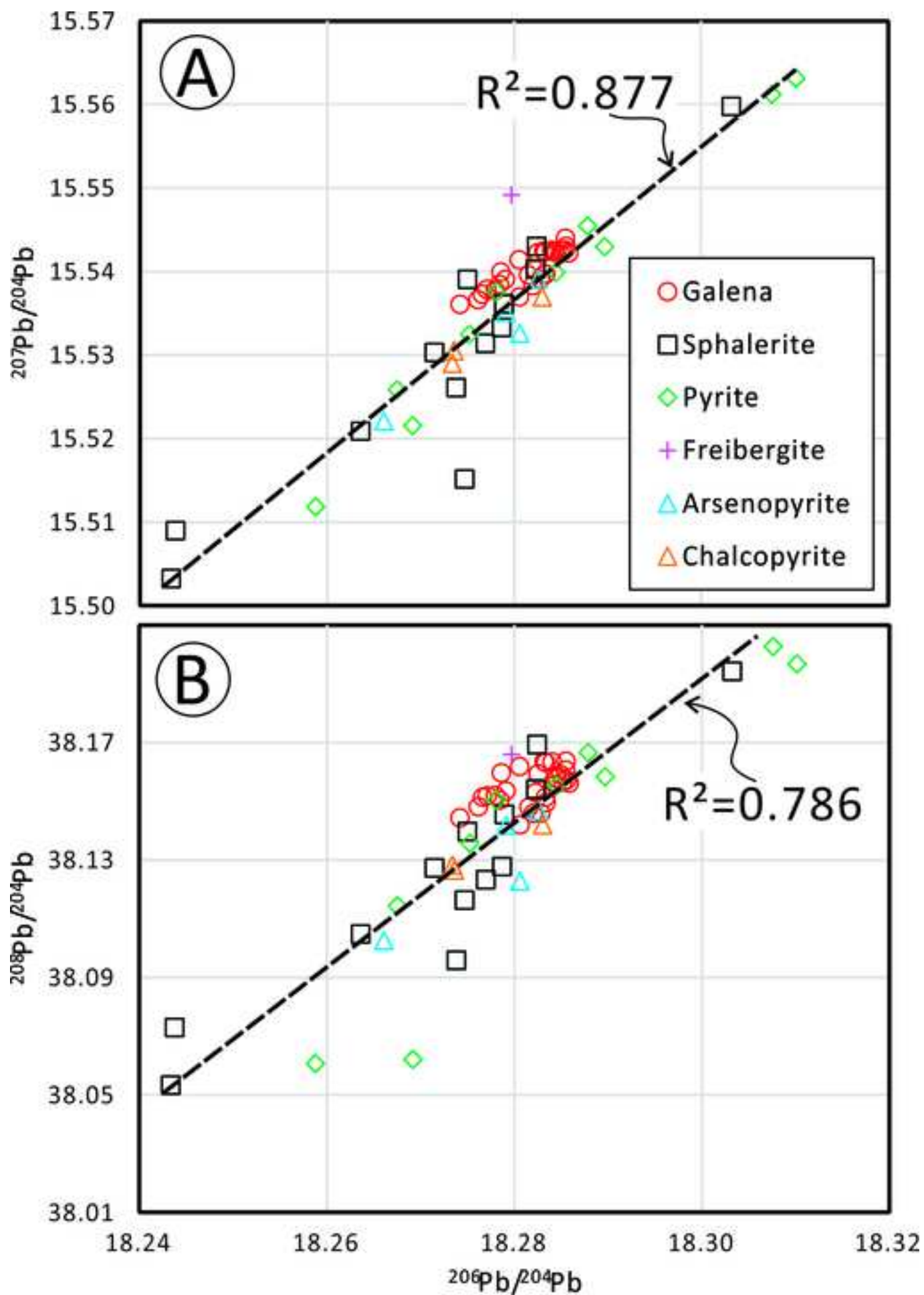


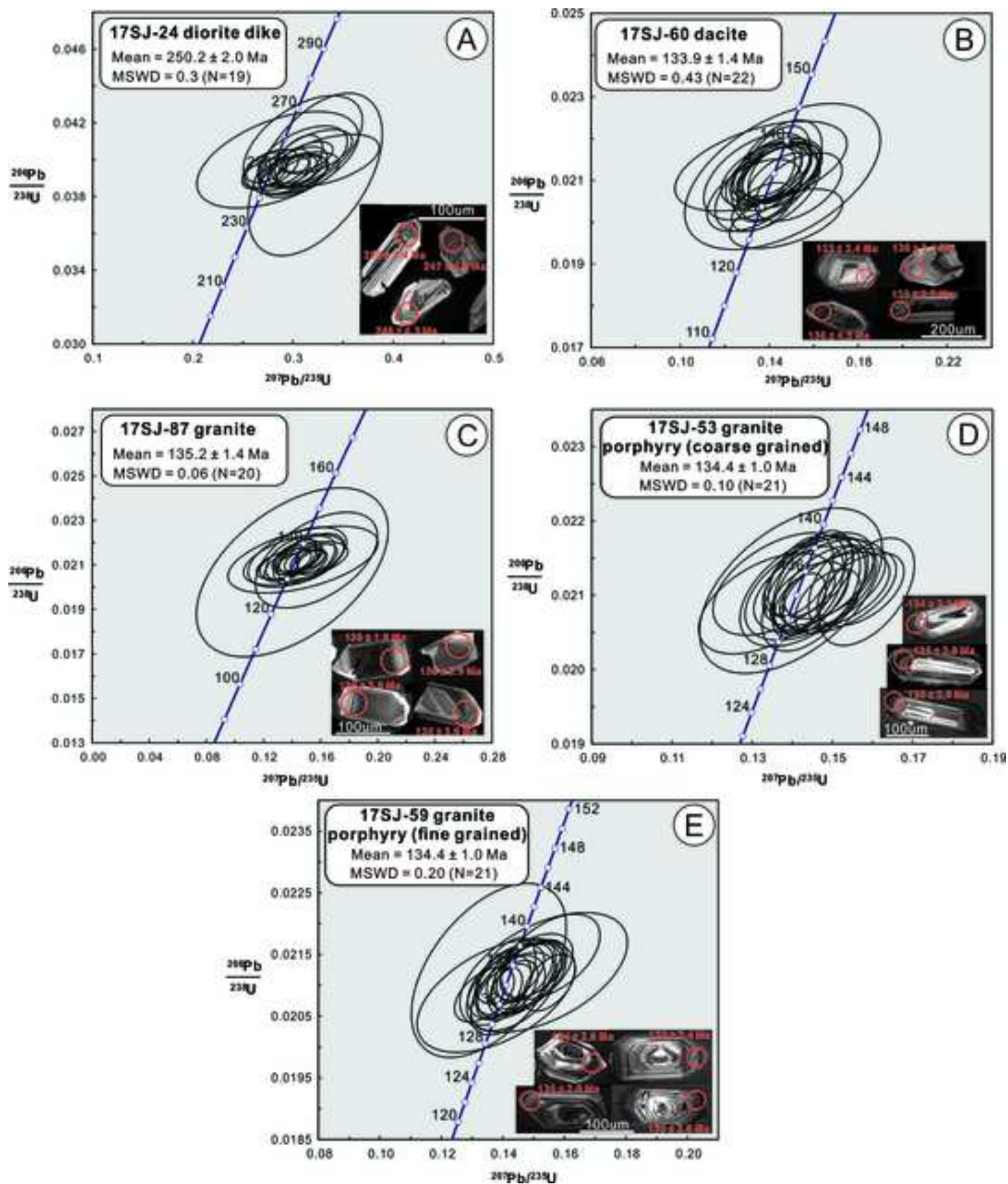


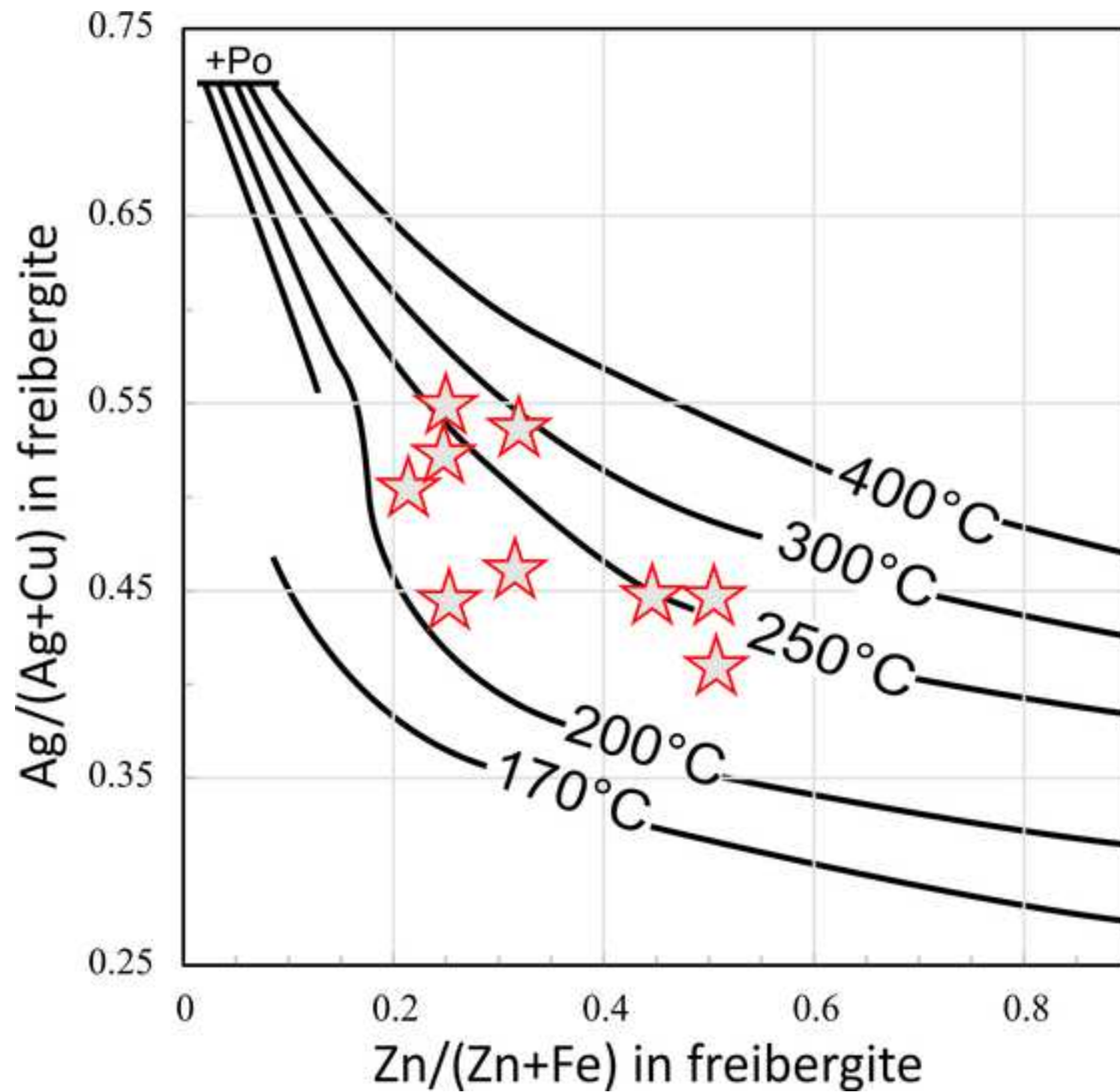


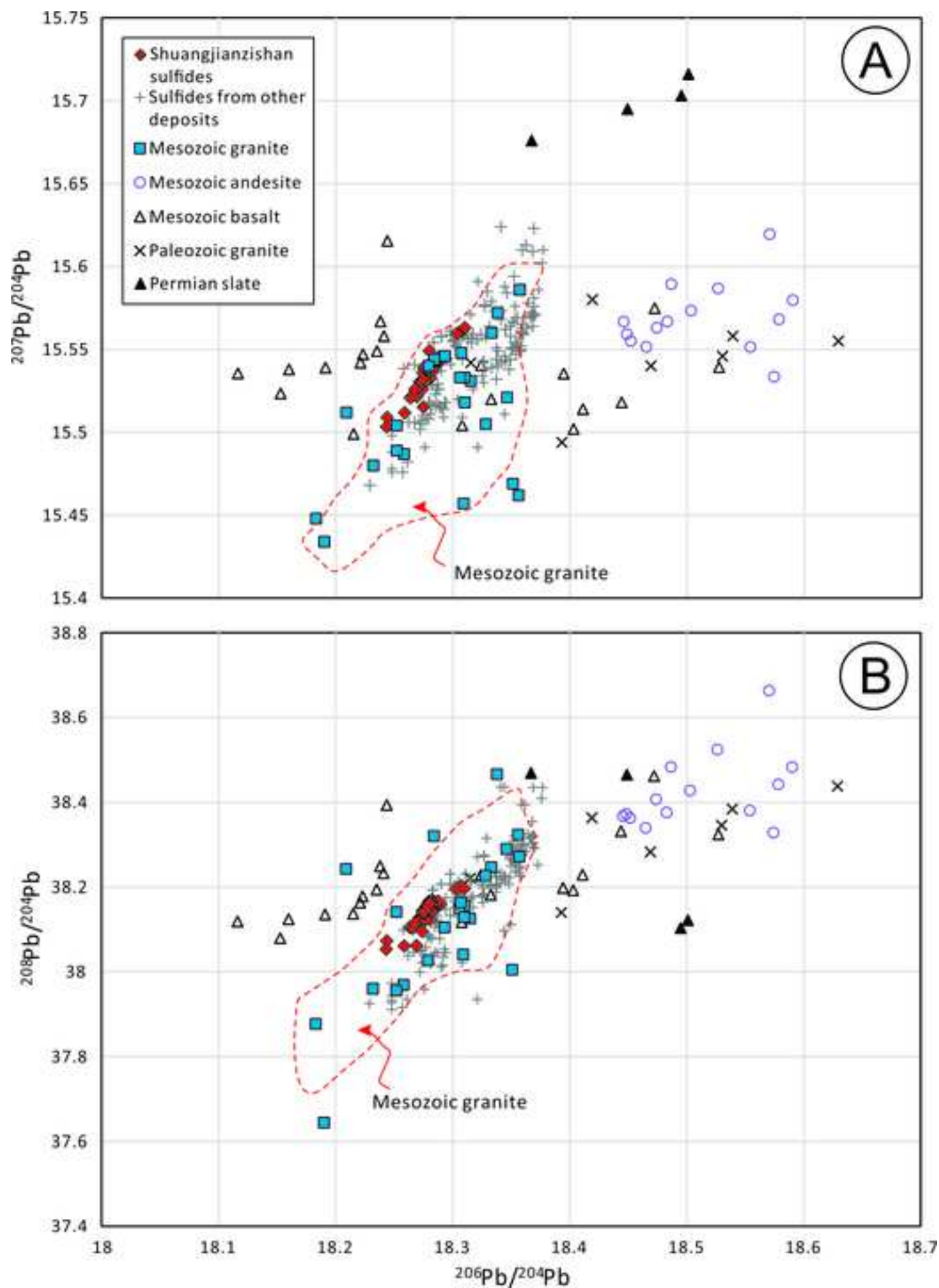


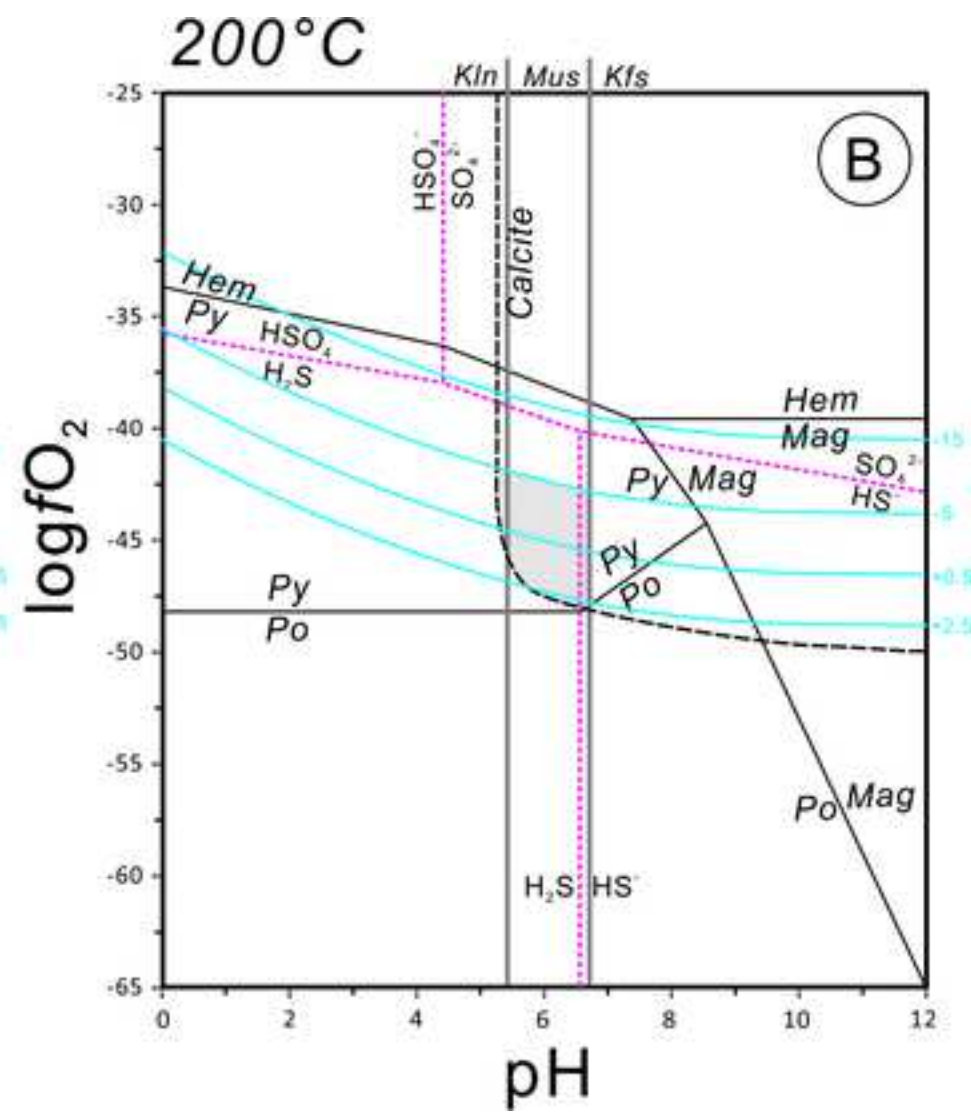
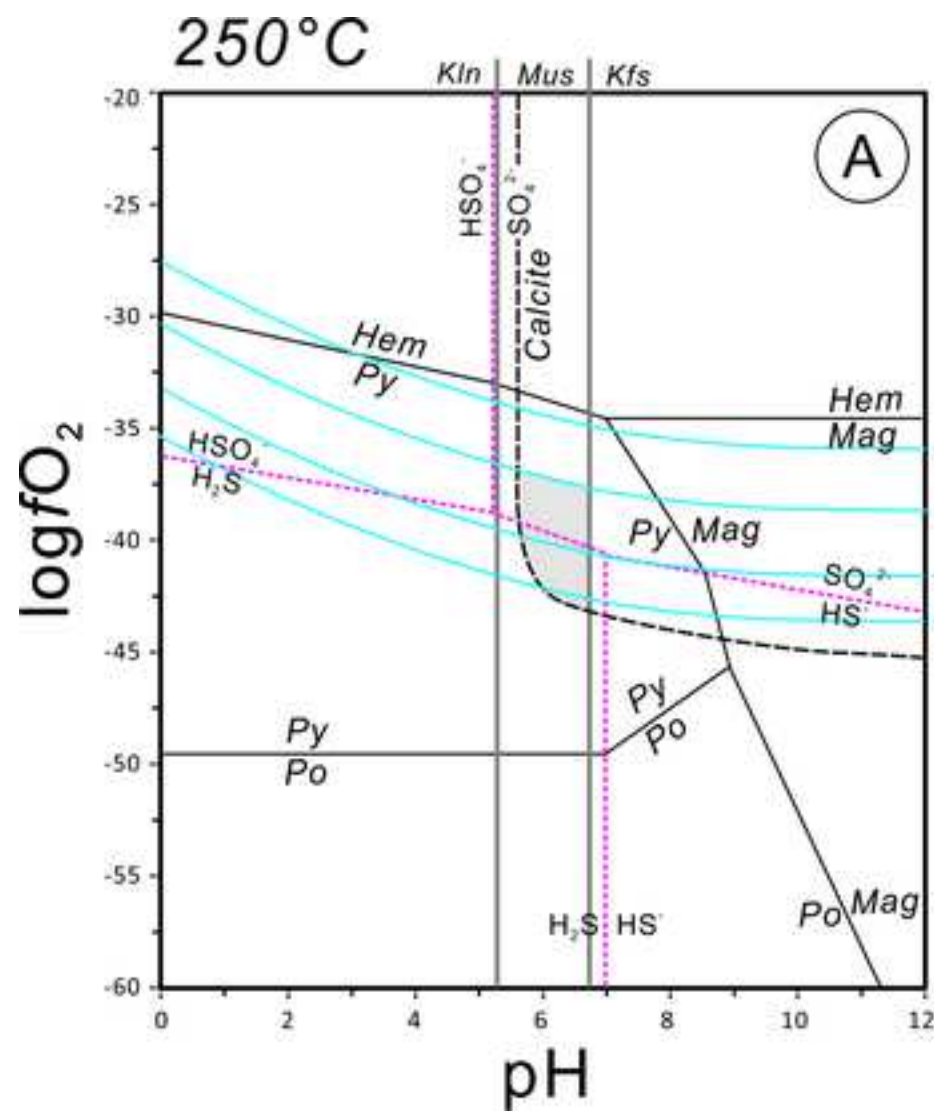


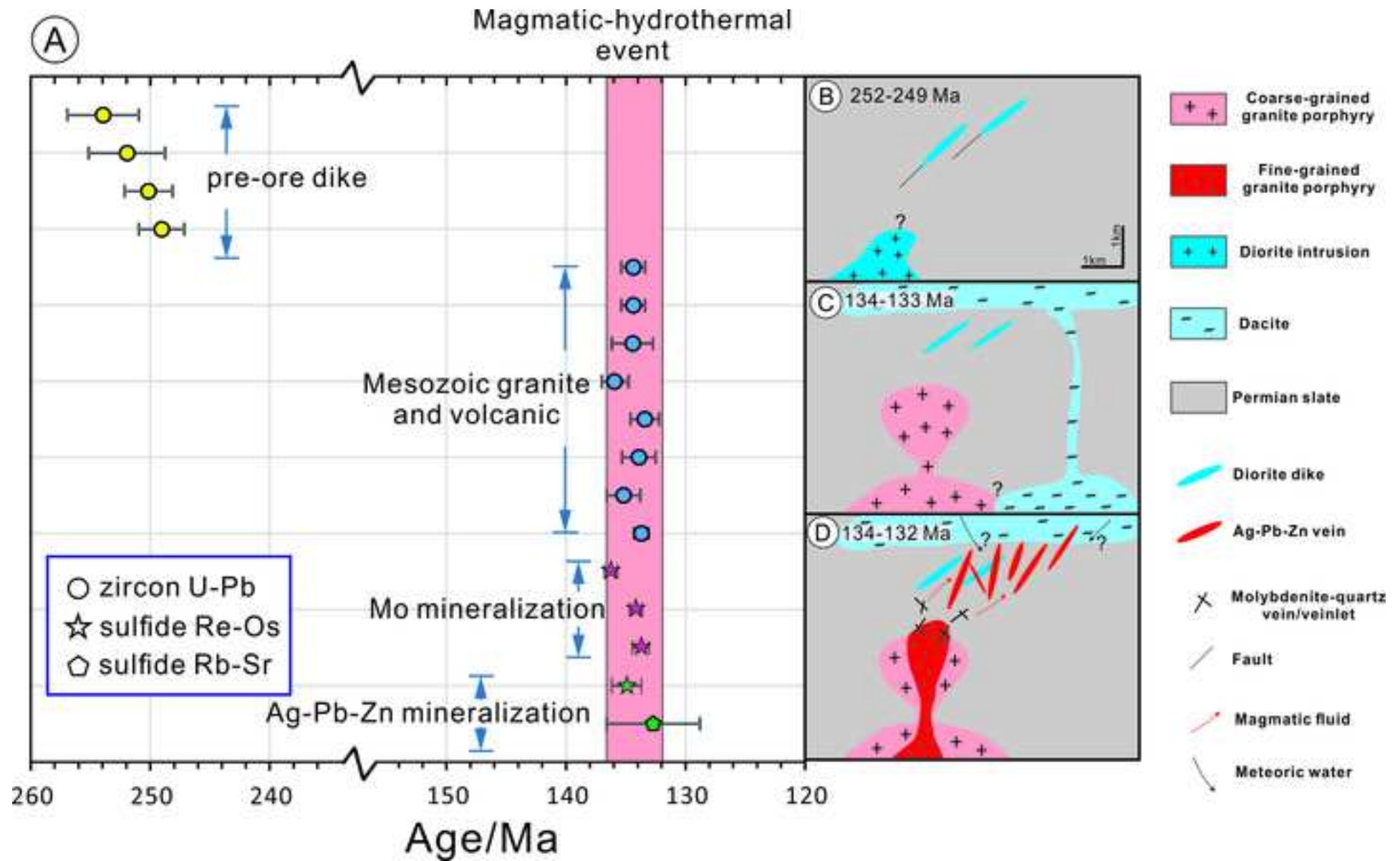












Sample	17SJ-47	17SJ-48	17SJ-59
rock type	granite porphyry (fine-grained)	granite porphyry (fine-grained)	granite porphyry (fine-grained)
wt.%			
SiO <sub>2</sub>	80.0	77.3	76.2
TiO <sub>2</sub>	0.1	0.1	0.1
Al <sub>2</sub> O <sub>3</sub>	11.2	12.1	12.9
TFe <sub>2</sub> O <sub>3</sub>	0.8	1.0	1.1
MnO	0	0	0
MgO	0.2	0.1	0.1
CaO	0.2	0.2	0.6
Na <sub>2</sub> O	2.2	3.5	3.7
K <sub>2</sub> O	4.6	4.7	4.5
P <sub>2</sub> O <sub>5</sub>	0	0	0
LOI	0.7	0.7	0.7
ppm			
Sc	1.1	1.1	0.9
Cu	16.3	19.4	23.3
Zn	30.3	31.0	30.3
Ga	17.6	18.6	19.9
Rb	250.8	247.5	252.0
Sr	58.0	54.6	56.1
Y	35.1	31.3	48.4
Zr	101.2	105.7	171.2
Nb	12.6	12.9	14.8
Sn	4.9	5.0	4.5
Cs	9.4	5.9	7.3
Ba	212.7	151.4	152.7
La	21.2	24.4	27.1
Ce	45.7	52.7	57.8
Pr	5.3	6.0	6.7
Nd	18.5	21.3	22.9
Sm	4.1	4.7	5.4
Eu	0.2	0.2	0.2
Gd	3.7	4.2	5.2
Tb	0.7	0.7	1.0
Dy	5.0	4.8	6.7
Ho	1.0	0.9	1.4
Er	3.5	3.0	4.7
Tm	0.6	0.5	0.8
Yb	4.2	3.4	5.5
Lu	0.6	0.5	0.8
Hf	4.3	4.4	6.5
Ta	2.2	2.1	2.4
Pb	36.3	26.2	26.8
Th	32.4	37.3	38.8
U	12.8	19.1	22.3

Table 1 Major and trace element concentrations for magmatic rocks in the Shuangjianzishan ore

17SJ-50	17SJ-51	17SJ-52
granite porphyry (fine-grained)	granite porphyry (coarse-grained)	granite porphyry (coarse-grained)
75.7	69.7	70.0
0.1	0.4	0.4
12.6	14.3	14.4
1.1	2.9	2.9
0	0.1	0.1
0.1	0.6	0.7
0.4	1.6	1.5
3.5	4.1	4.1
4.9	4.3	4.1
0.1	0.1	0.1
0.7	1.4	1.4
1.0	4.4	4.3
3.6	14.8	8.3
27.7	60.1	64.8
20.4	23.0	22.6
276.8	207.4	227.9
55.1	262.0	267.5
34.0	31.9	31.7
125.0	207.8	196.1
15.4	14.0	12.8
3.2	6.0	8.3
8.1	10.4	11.7
150.3	435.7	457.8
25.4	30.2	31.4
54.0	63.9	65.0
6.2	7.4	7.7
21.5	27.5	27.7
4.7	6.2	5.9
0.2	0.7	0.7
4.1	5.3	5.1
0.7	0.9	0.9
4.9	5.5	5.3
1.0	1.0	1.0
3.4	3.2	3.1
0.6	0.5	0.5
4.0	3.3	3.1
0.6	0.5	0.5
5.4	6.9	6.3
2.6	1.5	1.3
26.6	29.9	20.1
39.4	26.0	22.9
15.2	9.0	7.8

district

	17SJ-53	17SJ-87	17SJ-24	17SJ-63
	granite porphyry (coarse-grained)	granite intrusion (northern part)	granodiorite dike	diorite dike
	69.6	73.6	67.3	54.2
	0.4	0.2	0.6	0.9
	15.3	14.1	16.1	14.7
	2.9	1.2	4.3	7.6
	0.1	0.0	0.1	0.2
	0.7	0.1	1.4	4.7
	1.7	0.4	0.4	6.7
	4.6	3.3	2.3	3.0
	4.0	5.0	4.4	3.5
	0.1	0	0.1	0.6
	0.9	1.1	2.6	4.1
	4.0	3.7	5.6	25.6
	4.1	4.1	3.9	39.1
	55.9	34.6	1243.9	83.2
	23.3	22.7	21.5	16.6
	214.2	157.2	122.1	85.9
	291.1	21.4	116.3	442.9
	33.4	31.0	10.4	22.9
	227.1	381.2	225.0	124.0
	13.0	13.1	7.9	4.7
	11.8	6.0	8.3	2.2
	11.4	6.0	14.5	0.5
	480.5	145.8	671.6	671.1
	24.8	65.9	27.4	12.5
	53.5	134.6	54.6	27.6
	6.6	15.5	6.2	3.7
	24.3	55.4	22.6	15.8
	5.5	9.8	4.1	3.8
	0.6	0.2	1.0	1.2
	5.0	6.9	3.0	3.9
	0.8	1.0	0.3	0.6
	5.4	6.0	2.0	4.0
	1.0	1.1	0.4	0.8
	3.3	3.2	1.0	2.4
	0.5	0.4	0.1	0.3
	3.3	3.1	0.7	2.3
	0.5	0.4	0.1	0.4
	6.8	10.5	5.4	3.4
	1.5	1.0	0.6	0.3
	18.1	23.4	261.2	21.6
	18.0	22.1	10.6	3.5
	6.9	5.3	2.6	1.3

---

17SJ-60

---

dacite

---

65.0

0.6

15.9

4.2

0.1

1.1

1.9

4.6

3.6

0.1

2.2

6.8

5.2

70.0

17.3

74.7

802.9

17.7

196.1

8.1

1.5

2.5

1239.8

31.1

60.6

6.9

24.3

4.3

1.1

3.5

0.5

3.2

0.6

1.8

0.3

1.7

0.3

5.1

0.6

20.6

9.1

2.9

---

Table 2 In situ sulfur isotope results of ore minerals

Number	Samples	Depth (m)	Ore stage	Minerals	$\delta^{34}\text{S}_{\text{vcdt}}$ (‰)
1	15SJ-16-Q1-Gn-1	230	II-1	Gn	-3.41
2	15SJ-16-Q1-Py-2	230	II-1	Py	-1.11
3	15SJ-16-Q1-Sp-3	230	II-1	Sp	-1.45
4	15SJ-16-Q2-Gn-1	230	II-1	Gn	-4.67
5	15SJ-16-Q2-Sp-2	230	II-1	Sp	-1.53
6	15SJ-16-Q2-Apy-3	230	II-1	Apy	-2.54
7	15SJ-16-Q3-Gn-1	230	II-1	Gn	-3.40
8	15SJ-16-Q3-Gn-2	230	II-1	Gn	-3.51
9	15SJ-16-Q3-Sp-3	230	II-1	Sp	-1.20
10	15SJ-31-Q1-Gn-1	150	II-1	Gn	-3.64
11	15SJ-31-Q1-Gn-2	150	II-1	Gn	-3.48
12	15SJ-31-Q1-Frb-3	150	II-2	Frb	-1.72
13	15SJ-31-Q1-Frb-4	150	II-2	Frb	-1.35
14	15SJ-31-Q4-Frb-1	150	II-2	Frb	-1.18
15	15SJ-31-Q4-Frb-2	150	II-2	Frb	-0.44
16	15SJ-43-Q1-Gn-1	190	II-1	Gn	-3.79
17	15SJ-43-Q1-Gn-2	190	II-1	Gn	-3.53
18	15SJ-43-Q1-Gn-3	190	II-1	Gn	-3.35
19	15SJ-43-Q1-Gn-4	190	II-1	Gn	-3.66
20	15SJ-43-Q1-Gn-5	190	II-1	Gn	-3.22
21	15SJ-43-Q2-Gn-1	190	II-1	Gn	-4.62
22	15SJ-43-Q2-Gn-2	190	II-1	Gn	-3.83
23	15SJ-43-Q2-Py-3	190	I	Py	-1.65
24	15SJ-43-Q2-Sp-4	190	II-1	Sp	-1.07
25	15SJ-51-Q1-Gn-1	230	II-1	Gn	-3.14
26	15SJ-51-Q1-Gn-2	230	II-1	Gn	-3.11
27	15SJ-51-Q1-Gn-3	230	II-1	Gn	-4.51
28	15SJ-51-Q1-Sp-4	230	II-1	Sp	-0.79
29	15SJ-51-Q1-Sp-5	230	II-1	Sp	-2.39
30	15SJ-51-Q2-Gn-1	230	II-1	Gn	-3.42
31	15SJ-51-Q2-Gn-2	230	II-1	Gn	-4.10
32	15SJ-51-Q2-Sp-3	230	II-1	Sp	-1.21
33	15SJ-51-Q2-Sp-4	230	II-1	Sp	-2.76
34	15SJ-84-Q1-Gn-1	110	II-1	Gn	-3.68
35	15SJ-84-Q1-Py-2	110	II-1	Py	-0.87
36	15SJ-84-Q1-Sp-3	110	II-1	Sp	-0.62
37	15SJ-84-Q2-Gn-1	110	II-1	Gn	-3.78
38	15SJ-84-Q2-Gn-2	110	II-1	Gn	-3.96
39	15SJ-84-Q2-Py-3	110	II-1	Py	-1.27

Abbreviations: Apy-arsenopyrite; Caf-canfieldite; Ccp-chalcopyrite; Frb-freibergite; Gn-galena; Py-pyrite; Py

in the Shuangjianishan Ag-Pb-Zn deposit

Number	Samples	Depth (m)	Ore stage	Minerals	$\delta^{34}\text{S}_{\text{vcdt}}$ (‰)
40	15SJ-84-Q3-Apy-1	110	II-1	Apy	-1.36
41	15SJ-84-Q4-Apy-1	110	II-1	Apy	-1.08
42	15SJ-94-Q1-Pyr-1	110	II-2	Pyr	2.13
43	15SJ-94-Q1-Pyr-2	110	II-2	Pyr	2.44
44	15SJ-94-Q1-Pyr-3	110	II-2	Pyr	1.41
45	15SJ-94-Q1-Caf-4	110	II-2	Caf	-0.65
46	15SJ-94-Q1-Gn-5	110	II-1	Gn	-3.85
47	15SJ-94-Q2-Gn-1	110	II-1	Gn	-3.47
48	15SJ-94-Q2-Caf-2	110	II-2	Caf	-1.94
49	15SJ-94-Q2-Ccp-3	110	II-1	Ccp	-1.86
50	15SJ-94-Q3-Caf-1	110	II-2	Caf	-1.35
51	15SJ-94-Q4-Caf-1	110	II-2	Caf	-1.87
52	15SJ-94-Q4-Caf-2	110	II-2	Caf	-1.91
53	15SJ-94-Q5-Caf-1	110	II-2	Caf	-1.53
54	15SJ-94-Q5-Sp-2	110	II-1	Sp	0.27
55	15SJ-94-Q5-Py-3	110	II-1	Py	-1.80
56	15SJ-94-Q5-Gn-4	110	II-1	Gn	-3.25
57	15SJ-97-Q1-Py-1	110	I	Py	-1.27
58	15SJ-97-Q1-Py-2	110	I	Py	-1.19
59	15SJ-97-Q1-Ccp-3	110	II-1	Ccp	-1.42
60	15SJ-97-Q1-Ccp-4	110	II-1	Ccp	-1.71
61	15SJ-97-Q1-Sp-5	110	II-1	Sp	-1.17
62	15SJ-97-Q2-Ccp-1	110	II-1	Ccp	-1.13
63	15SJ-97-Q2-Gn-2	110	II-1	Gn	-1.54
64	15SJ-97-Q2-Py-3	110	I	Py	-1.22
65	15SJ-97-Q2-Sp-4	110	II-1	Sp	-0.88
66	15SJ-99-Q1-Apy-1	110	II-1	Apy	-0.39
67	15SJ-99-Q1-Sp-2	110	II-1	Sp	-0.91
68	15SJ-99-Q1-Gn-3	110	II-1	Gn	-3.49
69	15SJ-99-Q1-Ccp-4	110	II-1	Ccp	-1.78
70	15SJ-99-Q2-Gn-1	110	II-1	Gn	-2.74
71	15SJ-99-Q2-Gn-2	110	II-1	Gn	-2.57
72	15SJ-104-Q1-Py-1	190-210	II-1	Py	-0.92
73	15SJ-104-Q1-Sp-2	190-210	II-1	Sp	-2.47
74	15SJ-104-Q1-Gn-3	190-210	II-1	Gn	-4.57
75	15SJ-104-Q2-Sp-1	190-210	II-1	Sp	-2.95
76	15SJ-104-Q2-Gn-2	190-210	II-1	Gn	-4.18
77	15SJ-104-Q2-Py-3	190-210	I	Py	-1.36

r-pyrargyrite; Sp-sphalerite.

Table 3 In situ lead isotope results of ore minerals in the Shuangji

Number	Samples	Depth (m)	Ore stage	Minerals	$^{206}\text{Pb}/^{204}\text{Pb}$
1	15SJ-104-q1-py-1	190-210	I	Pyrite	18.308
2	15SJ-104-q1-sp-1	190-210	II-1	Sphalerite	18.264
3	15SJ-104-q1-apy-1	190-210	II-1	Arsenopyrite	18.279
4	15SJ-104-q2-gn-3	190-210	II-1	Galena	18.283
5	15SJ-104-q2-py-1	190-210	II-1	Pyrite	18.284
6	15SJ-104-q2-sp-1	190-210	II-1	Sphalerite	18.244
7	15SJ-16-q1-gn-1	230	II-1	Galena	18.282
8	15SJ-16-q1-py-1	230	II-1	Pyrite	18.269
9	15SJ-16-q1-sp-1	230	II-1	Sphalerite	18.303
10	15SJ-16-q2-gn-1	230	II-1	Galena	18.283
11	15SJ-16-q2-sp-1	230	II-1	Sphalerite	18.279
12	15SJ-16-q2-apy-1	230	II-1	Arsenopyrite	18.281
13	15SJ-16-q3-gn-1	230	II-1	Galena	18.283
14	15SJ-16-q3-gn-2	230	II-1	Galena	18.281
15	15SJ-16-q3-sp-1	230	II-1	Sphalerite	18.275
16	15SJ-31-q1-frb-1	150	II-2	Freibergite	18.280
17	15SJ-31-q4-gn-1	150	II-1	Galena	18.285
18	15SJ-31-q4-gn-2	150	II-1	Galena	18.284
19	15SJ-43-q1-gn-1	190	II-1	Galena	18.277
20	15SJ-43-q1-gn-2	190	II-1	Galena	18.277
21	15SJ-43-q1-gn-3	190	II-1	Galena	18.276
22	15SJ-43-q1-gn-4	190	II-1	Galena	18.285
23	15SJ-43-q1-gn-5	190	II-1	Galena	18.286
24	15SJ-43-q2-gn-1	190	II-1	Galena	18.274
25	15SJ-43-q2-gn-2	190	II-1	Galena	18.278
26	15SJ-43-q2-py-1	190	II-1	Pyrite	18.290
27	15SJ-43-q2-sp-1	190	II-1	Sphalerite	18.274
28	15SJ-51-q1-gn-1	230	II-1	Galena	18.286
29	15SJ-51-q1-gn-2	230	II-1	Galena	18.285
30	15SJ-51-q1-gn-3	230	II-1	Galena	18.282
31	15SJ-51-q1-sp-1	230	II-1	Sphalerite	18.282
32	15SJ-51-q1-sp-2	230	II-1	Sphalerite	18.271
33	15SJ-51-q2-gn-1	230	II-1	Galena	18.282
34	15SJ-51-q2-gn-2	230	II-1	Galena	18.283
35	15SJ-51-q2-sp-1	230	II-1	Sphalerite	18.282
36	15SJ-51-q2-sp-2	230	II-1	Sphalerite	18.243
37	15SJ-84-q1-gn-1	110	II-1	Galena	18.284
38	15SJ-84-q1-py-1	110	I	Pyrite	18.310
39	15SJ-84-q2-gn-1	110	II-1	Galena	18.286
40	15SJ-84-q2-gn-2	110	II-1	Galena	18.285
41	15SJ-84-q2-py-1	110	I	Pyrite	18.288
42	15SJ-84-q3-apy-1	110	II-1	Arsenopyrite	18.266
43	15SJ-84-q4-apy-1	110	II-1	Arsenopyrite	18.283
44	15SJ-94-q1-gn-1	110	II-1	Galena	18.283
45	15SJ-94-q2-gn-1	110	II-1	Galena	18.283
46	15SJ-97-q1-ccp-1	110	II-1	Chalcopyrite	18.273
47	15SJ-97-q1-ccp-2	110	II-1	Chalcopyrite	18.274
48	15SJ-97-q1-py-1	110	I	Pyrite	18.268
49	15SJ-97-q1-py-2	110	I	Pyrite	18.259

50	15SJ-97-q1-sp-1	110	II-1	Sphalerite	18.277
51	15SJ-97-q2-ccp-1	110	II-1	Chalcopyrite	18.283
52	15SJ-97-q2-gn-1	110	II-1	Galena	18.279
53	15SJ-97-q2-py-1	110	I	Pyrite	18.275
54	15SJ-97-q2-sp-1	110	II-1	Sphalerite	18.279
55	15SJ-99-q1-gn-1	110	II-1	Galena	18.279
56	15SJ-99-q1-py-1	110	I	Pyrite	18.278
57	15SJ-99-q1-sp-1	110	II-1	Sphalerite	18.275
58	15SJ-99-q2-gn-1	110	II-1	Galena	18.278
59	15SJ-99-q2-gn-1	110	II-1	Galena	18.281

---

## ianzishan Ag-Pb-Zn deposit

$1\sigma$	$^{207}\text{Pb}/^{204}\text{Pb}$	$1\sigma$	$^{208}\text{Pb}/^{204}\text{Pb}$	$1\sigma$
0.020	15.561	0.018	38.203	0.042
0.026	15.521	0.023	38.105	0.056
0.003	15.535	0.003	38.142	0.009
0.002	15.542	0.002	38.163	0.006
0.006	15.540	0.005	38.155	0.013
0.015	15.509	0.013	38.073	0.031
0.002	15.540	0.002	38.148	0.006
0.009	15.522	0.008	38.062	0.022
0.004	15.560	0.004	38.194	0.012
0.002	15.539	0.002	38.146	0.005
0.006	15.533	0.005	38.128	0.015
0.004	15.533	0.004	38.123	0.010
0.002	15.540	0.002	38.150	0.006
0.002	15.537	0.002	38.142	0.007
0.013	15.515	0.012	38.116	0.029
0.010	15.549	0.010	38.166	0.032
0.002	15.542	0.002	38.158	0.007
0.002	15.542	0.002	38.156	0.007
0.002	15.537	0.002	38.151	0.006
0.002	15.538	0.002	38.152	0.006
0.003	15.537	0.003	38.148	0.008
0.002	15.542	0.002	38.159	0.006
0.002	15.543	0.002	38.157	0.006
0.002	15.536	0.002	38.144	0.007
0.002	15.538	0.003	38.152	0.007
0.004	15.543	0.004	38.159	0.011
0.007	15.526	0.006	38.096	0.017
0.002	15.544	0.002	38.164	0.007
0.002	15.542	0.002	38.157	0.005
0.002	15.540	0.002	38.153	0.006
0.026	15.543	0.022	38.169	0.055
0.005	15.530	0.005	38.127	0.013
0.002	15.538	0.002	38.146	0.006
0.002	15.540	0.002	38.151	0.005
0.002	15.540	0.002	38.154	0.006
0.015	15.503	0.013	38.053	0.032
0.002	15.543	0.002	38.163	0.006
0.016	15.563	0.014	38.197	0.035
0.002	15.542	0.002	38.156	0.006
0.003	15.543	0.003	38.161	0.008
0.005	15.545	0.005	38.167	0.012
0.004	15.522	0.003	38.103	0.010
0.002	15.539	0.002	38.147	0.007
0.003	15.542	0.003	38.164	0.008
0.002	15.542	0.002	38.159	0.006
0.006	15.529	0.006	38.128	0.020
0.006	15.531	0.006	38.127	0.015
0.004	15.526	0.004	38.114	0.011
0.010	15.512	0.009	38.061	0.023

0.004	15.531	0.004	38.123	0.010
0.008	15.537	0.007	38.142	0.020
0.002	15.539	0.002	38.154	0.007
0.002	15.532	0.003	38.136	0.008
0.006	15.536	0.006	38.146	0.016
0.003	15.540	0.003	38.160	0.008
0.001	15.538	0.002	38.150	0.005
0.007	15.539	0.006	38.140	0.016
0.002	15.538	0.002	38.150	0.007
0.002	15.541	0.003	38.162	0.007

---

Table 4 Molybdenite Re-Os results of the Shuangjianzishan Ag-Pb

Sample	wt (g)	Re (ppm)	$\pm 2\sigma$	$^{187}\text{Re}$ (ppm)	$\pm 2\sigma$	$^{187}\text{Os}$ (ppb)	$\pm 2\sigma$
17SJ-34	0.021	2.640	0.012	1.659	0.008	3.773	0.015
17SJ-35	0.061	0.119	0.001	0.075	0.001	0.167	0.001
17SJ-41	0.059	1.994	0.008	1.253	0.005	2.805	0.009

<sup>a</sup>uncertainty including only mass spectrometry uncertainty

<sup>b</sup>uncertainty including all sources of analytical uncertainty

<sup>c</sup>uncertainty including all sources of analytical uncertainty plus decay constant

-Zn deposit

<b>Age (Ma)</b>	<b><math>\pm 2\sigma^a</math></b>	<b><math>\pm 2\sigma^b</math></b>	<b><math>\pm 2\sigma^c</math></b>
136.31	0.15	0.75	0.87
133.69	0.01	1.13	1.20
134.19	0.12	0.66	0.78

Table 5 Pyrite Re-Os

Samples	Re (ppb)	$\pm 2\sigma$	$^{187}\text{Re}$ (ppb)	$\pm 2\sigma$	Total Os (ppt)	$\pm 2\sigma$	$^{192}\text{Os}$ (ppt)	$\pm 2\sigma$	$^{187}\text{Os}^r$ (ppt)
15SJ-10	0.262	0.001	0.164	0.001	2.198	0.069	0.670	0.041	0.371
15SJ-16	0.520	0.003	0.327	0.002	1.446	0.782	0.164	0.085	0.736
17SJ-26	0.886	0.003	0.557	0.002	13.082	0.153	3.546	0.065	1.253
15SJ-114	1.077	0.004	0.677	0.002	1.483	1.252	0.061	0.040	1.317

Note: The initial  $^{187}\text{Os}/^{188}\text{Os}$  ( $\text{Os}_i$ ) values, with the exception of sample 15SJ-114, are assumed to have a large range fro

data of the Shuangjianzishan Ag-Pb-Zn deposit

$\pm 2\sigma$	$^{187}\text{Os} \text{ r } \%$	$^{187}\text{Re}/^{188}\text{Os}$	$\pm 2\sigma$	$^{187}\text{Os}/^{188}\text{Os}$	$\pm 2\sigma$	rho	% Re blank	% $^{187}\text{Os}$ blank
0.028	60.7	776.4	48.0	2.8	0.2	0.98	2.2	0.9
0.170	69.3	6309.3	3269.9	20.4	10.6	1.00	2.3	1.1
0.146	27.0	496.9	9.2	4.1	0.1	0.78	0.6	0.1
0.041	99.3	34959.9	23095.1	69.0	45.6	1.00	0.5	0.4

m ~1.1 to 6.2; uncertainty correlation factor (rho) is applied to assess the degree of correlation between  $^{187}\text{Re}$ ,

<b>% <sup>188</sup>Os blank</b>	<b>Os<sub>i</sub> (ppt)</b>	<b>Age (Ma)</b>
10.9	1.09	134.5
50.8	6.16	135.6
2.2	3.02	135.0
56.9	-	118.1

<sup>188</sup>Os and <sup>187</sup>Os/<sup>188</sup>Os ratios.



[Click here to access/download](#)

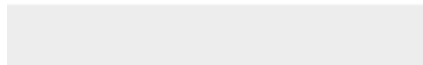
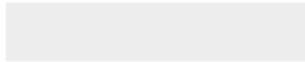
**Electronic Appendix (Excel etc.)**

Fig A1 Petrochemical summary of granites revised.jpg





Click here to access/download  
**Electronic Appendix (Excel etc.)**  
Fig A2 petrochemical plots.jpg

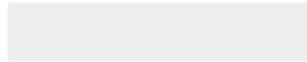




Click here to access/download

**Electronic Appendix (Excel etc.)**

Fig A3 REE and spider diagram-revised.jpg

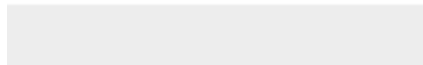




Click here to access/download

**Electronic Appendix (Excel etc.)**

Fig A4 Hisgram T of S isotope.jpg





Click here to access/download

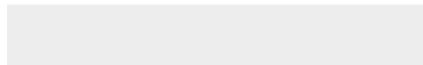
**Electronic Appendix (Excel etc.)**

Fig A5 in situ vs mineral sep Pb data-revised.jpg



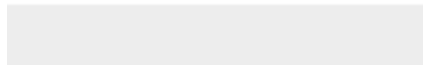


Click here to access/download  
**Electronic Appendix (Excel etc.)**  
Fig A6 trace element diagram.jpg





Click here to access/download  
**Electronic Appendix (Excel etc.)**  
Table A1 EPMA results-revised.xlsx

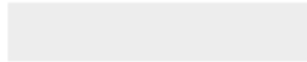




Click here to access/download

**Electronic Appendix (Excel etc.)**

Table A2 zircon U-Pb data.xlsx





Click here to access/download

**Electronic Appendix (Excel etc.)**

Table A3 Collected lead isotope data.xls

